UNIVERSITY OF MODENA AND REGGIO EMILIA

Department of engineering Enzo Ferrari

PhD "Enzo Ferrari" in Industrial and Environmental Engineering

XXXII Cycle

Elastohydrodynamic analysis in engine lubricated contacts: managing of fluid cavitation and asperity contact problems

Candidate:

Andrea Ferretti

Supervisor:

Prof. Matteo Giacopini

School Director/Coordinator:

Prof. Alberto Muscio

Academic Year: 2018/2019

To my grandparents…

Abstract

The continuous demand of even-higher efficiency in internal combustion engines has led to a growing interest in the study of their internal losses' mechanisms. In particular, a large amount of friction losses is registered at engine's bearings, whose correct definition deeply affects the achievement of the desired performances. The design of the layout of engine's lubricated contacts is one of the first design choices to be addressed and a modification of their quotas usually involves an almost complete engine's redesign.

The developing of simulation methodologies able to evaluate the adequacy of the design choices concerning the lubricated contacts is therefore fundamental, in order to considerably reduce the number of trial-and-errors steps usually required in the design process of an engine.

This activity deals with the problem of simulating lubricated contacts, mainly focusing on the developing of a proper approach to the analysis of the asperity contact problem. The hydrodynamic problem will be tackled adopting a mass-conserving algorithm, which uses a linear complementary formulation of the Reynolds equation to calculate the hydrodynamic pressure distribution within the lubricant film and to identify the cavitated region at given oil film height.

Great attention will be paid to the methodology used to deal with cases of mixed lubrication, in which a partial direct metal-to-metal contact occurs. Two different methodologies will be investigated, the first based on a complementary formulation of the asperity contact problem and the latter based on the theory introduced by Greenwood and Williamson and then deepened by Greenwood and Tripp. This theory introduces a direct relationship between the asperity contact pressure and the gap between the two mating surfaces, obtained by statistically evaluating the probability that two asperity peaks come into contact and approximating each peaks' contact according to the Hertzian theory.

The derived methodology is then applied to the elastohydrodynamic analysis of the conrod small-end/piston-pin coupling of an high performance Ducati motorcycle engine. In order to calibrate the asperity contact model based on the Greenwood and Tripp theory, some non-standard roughness parameters are necessary, useful to describe the entire profile from a statistical point of view. The meaning and value assumed by these parameters will be investigated by directly measuring the roughness profiles of the two mating surfaces and implementing a procedure able to calculate them, starting from their definition.

It will be shown how, by adopting different calibrations of the asperity contact model, it is possible to identify similar critical areas, in good agreement with empirical evidences of small end failures occurred during preliminary tests conducted at an early stage of the engine design process and under severe loading conditions. However, the absolute values of the various quantities involved are significantly different, making it difficult to identify admissible threshold values capable of defining the critical state of the components.

Acknowledgements

I would like to begin this work with some special thanks to those who made it possible, with their support and affection. The first thanks go to my family, my father Ivo, my mother Daniela, my sister Chiara and her boyfriend Nino, and all the other, who have always supported my decision to move far away from them, to follow my passions. Thanks to my grandmother, Teresa, who make me find her special meatballs every time I go to visit her, and to my grandfather Armando, former mechanic, who always listens with passion to the stories of my mechanical chores and teaches me how to improve my mechanical skills. Thanks to my girlfriend, Arianna, who is by my side even when it is more difficult.

Thanks to my friend Francesco, who introduced me to the university of Modena and Reggio Emilia, and is always ready to help me when I need him.

Thanks to the CDM team, Valerio, Saverio, Sara, Enrico, Luigi, Andrea, and other, that made my period at university one of the best of my life. To my supervisor, Giaco, from which I would like to learn how to manage the millions of commitments with his professionalism and attention, with that apparent tranquillity and calmness. He gave me the best opportunities of my life, showing a great trust in me that I hope to deserve.

I would also like to thank the guys I met in these years of work at Ducati Motor Holding S.P.A, Christian, Donato, Giuseppe, Leonardo, Michele, Francesco, who made me suddenly feel part of the team, and Stefano Fantoni, that support me both in the research and work activity.

A great acknowledge goes to Professor Elena Bassoli and her research group whose support to this activity was fundamental for the part of measurement of surfaces roughness profiles.

Contents

1. Introduction

1.1 Motivation and object

Aiming at reducing air pollution, in recent times a policy was developed that focuses on heavily reducing engines' emissions. A consistent reduction of pollution can be achieved applying a proper catalyst technology, but this doesn't affect the emission of CO_2 produced by combustion of internal combustion engines [1]. Considering this, most of the modern regulations mandate engine's fuel economy.

The reduction of engines' friction losses is a key component of energy conservation. Mechanical losses and friction in engine are mainly developed at contacting surfaces, such as ring-pack/liner, piston-skirt/liner, piston-pin/connecting-rod contacts, connecting rod and crankshaft bearings and so on. In [2], Wong and Tung propose an interesting overview of automotive engine friction reduction trends, focusing on the impact on fuel economy of each engine's component. A typical estimate of friction for a fired engine (diesel or SI), as a fraction of total fuel energy used is shown in Figure 1.1, in which mechanical friction is shown to take up roughly 4%−15% of the total fuel energy [3].

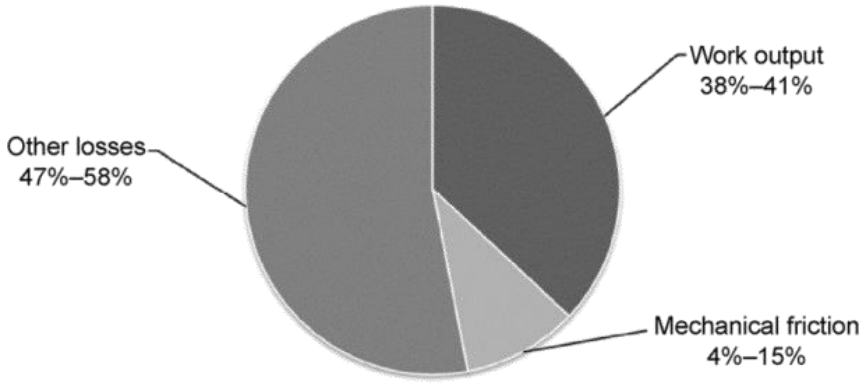

Figure 1.1. Distribution of total energy in a fired engine

The official European reference test for estimating engine efficiency is the NEDC (New European Driving Cycle) test. According with [4], during this test an automotive car equipped with a current two liter engine will produce approximately 120 g of CO_2 emissions per km. The friction power loss of the engine corresponds to 25-30 g of CO_2/km, with a corresponding fuel consumption of roughly 0.9 L/100 km. A general idea of engine component friction distribution is given by Figure 1.2. By optimizing bearings and their environment, which means the lubricant circuit and structural components, a great effect can be achieved on engine efficiency and emissions.

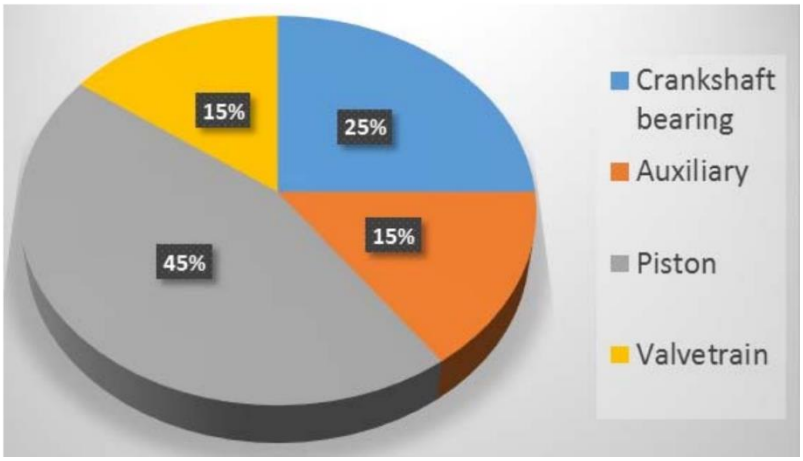

Figure 1.2. Engine friction distribution

In [5] an investigation of the influence of lubricant's properties on fuel efficiency is presented. It is important to notice that lowering the viscosity and frictional properties of fluid doesn't always lead to improvement in efficiency. Furthermore, it is highlighted that it is quite difficult to quantify the effect of changes in lubricant properties on fuel efficiency.

At the same time, the performance of internal combustion engines has constantly increased, this involving a consequent increase of the loads that contacts have to sustain. In particular, the conrod small end-piston pin coupling is one of the most critical engine part, since limited contact surfaces have to sustain high inertial and combustion forces [6]. High loads combined with temperature and risk of lubricant starvation may cause surface damages such as scuffing or seizure [7] [8].

The measures adopted to avoid contacts failure, such as clearance adjustments, oil supply pressures increment, hardening of materials coating, are often dictated by experience, rather than considerations based on dedicated calculations. Developing methodologies aimed to properly predict the tribological behaviour of lubricated contact is, therefore, mandatory. However, several difficulties have to be faced when approaching the lubrication problems, due to its strong non-linearity.

Reynold equation, instead of full Navier-Stokes equation, is commonly employed to tackle the lubrication problem, since the assumptions it is based on are satisfied in the majority of the relevant cases. Starting from it, various formulations have been proposed to handle the cavitation phenomenon. Under severe loading conditions, direct solid to solid contact may also occur, resulting in a non-negligible contribution to the load support given by the arising asperity contact pressure.

In this PhD activity, the algorithm proposed by Giacopini et al in [9] and [10], based on a complementarity formulation of the Reynold equation, is employed to solve the hydrodynamic problem in presence of cavitation. Two different methodologies are employed to tackle the direct metal to metal contact problem that arise in mixed lubrication condition, the first based on a linear complementarity formulation of the asperity contact problem first proposed in [11], and the latter based on the standard Greenwood/Tripp [12] theory. The influence of the adopted asperity contact model on the results are investigated, with a particular focus on the calibration of the particular model.

The percentage of load sustained by asperity contact pressure at given oil film thickness is strictly correlated to the roughness profiles of the two mating surfaces [13]. The Greenwood-Tripp model describes this correlation through a direct non-linear relation between surfaces clearance and contact stiffness, that need some non-standard roughness parameter in order to be set. To understand this parameter and to suggest some criteria for their calculation from typically available roughness data, an optical measurement of the roughness profiles of the two mating surfaces was performed and a procedure was implemented capable to calculate them starting from their definition.

The analysis object is the elastohydrodynamic analysis of the conrod small-end/piston pin coupling of an high performance Ducati motorbike engine. During some preliminary test performed at early stage of the design process, under severe loading conditions, some unusual

failure of the conrod small-end and wear of the outer surface of the piston pin were registered. This practical case is chosen as an applicative example to show the various steps, results and conclusions of the presented methodology.

2. Managing of the hydrodynamic problem

2.1 Overview

Approaching the tribological analysis of lubricated contact, the strong non-linearity of the problem must be faced:

- depending on the local hydrodynamic pressure, vapor or gases bubbles may appear in the oil film, thus involving discontinuity in lubricant pressure field;
- the value of pressure strongly depends on the oil film thickness, but, due to the surfaces' elastic deflection, the oil film thickness depends on pressure in turn;
- in mixed or boundary lubrication conditions, direct metal to metal contact occurs, so that part of the load is sustained by the fluid pressure, and part by the arising asperity contact pressure developed at roughness summits contact.

In this session, the way the first of this problem, the cavitation problem, is tackled is shown. In the diverging region of the geometry, where the fluid pressure drops below the vapor pressure, or the saturation pressure of the dissolved gasses, rupture in oil film happens and a non-active region of the lubricant domain can be identified. In this cavitated zone, the lubricant properties vary significantly. The 2D Reynold equation is commonly adopted instead of full Navier-Stokes equation to evaluate lubricant pressure knowing the contacting surfaces geometry, gap and relative velocity. To deal with the cavitation phenomenon, numerical treatments and modifications to its formulation have to be introduced. Various formulations have been proposed.

In [14] Jakobsson and Floberg proposed a film rupture model, based on mass flow continuity through the cavitation region capable of identify the boundaries of the cavitated zone. Within the cavitated zone the pressure is considered to be constant and equal the gas or vapor pressure of the lubricant, while the solution of the Reynolds equation gives the lubricant

pressure at the active counterparts. At the inception of the cavitation zone, according with Swift-Stieber model (also known as Reynolds condition), this model predicts a null pressure gradient, required by the flow continuity conditions. In [15] Floberg postulates the conservation of liquid mass flow through the whole cavitation zone, but without mass transfer between liquid lubricant and vapor or gas bubble at uniform pressure. The Jakobsson-Floberg-Olsson (JFO) model applies to dynamic load situations in which the surfaces may also undergo (time varying) squeeze film motions [16]. No bubble's dynamic is here considered and the cavitation zone changes instantaneously as the surfaces' squeeze speed changes, i.e. the phase change of liquid into vapor (or vice-versa) takes place at infinitesimally small times.

Sun and Brewe [17] note that the characteristic time for liquid vaporization (or vapor condensation) is very small when compared to the typical period of typical rotating machinery (> 1 ms), while on the other hand, the characteristic time for gas diffusion is orders of magnitude larger. Hence, the authors conclude that a dynamic cavitation bubble must contain fluid vapor since dissolved gases will not have enough time to come out of solution in a typical dynamic loading cycle. Braun and Hendricks [18] measured the pressure and chemical contents within the cavitation zone in a steadily loaded, fully flooded journal bearing. These authors, however, noted the appearance of sub ambient pressures in the cavity zone formed by gasses coming out of solution from the lubricant. The authors argue that a phase change (oil vaporization) requires of a source of energy not readily available in actual operation.

In [19] and [20], Erold and Adams develop an ingenious cavitation algorithm that incorporate the JFO model into a single Reynolds equation valid in the whole fluid domain and doesn't require the explicit location of the cavitation boundaries. A switch function $g(p)$ is introduced that is null in non-active zone and one if the pressure is greater than the cavitation pressure. The function also switches the character of the flow continuity (Reynolds) equation from elliptic to parabolic in the full film and cavitation regions, respectively.

Later developments have concentrated mainly on the implementation of fast and efficient numerical methods for the solution of the Elrod algorithm with applications to practical bearing configurations, and including dynamically loaded conditions [21] [22] [23] [24].

Some attempts to solve the problem of determining the active and cavitated regions using concept of complementarity can be found in [25] [26] [27]. However, those methods solve

the Reynolds equation in the whole domain assuming a constant lubricant density, which leads to an incomplete identification of film rupture and to an incorrect detection of film reformation, since the mass conservation is not ensured.
In the present work, the algorithm first proposed by Giacopini et al. in [10] is employed to deal with the cavitation problem. This algorithm ensures the mass conservation within the whole domain and is based on a newly defined set of complementarity variables.

2.2 Governing equation

There are two approach available to model hydrodynamic and elastohydrodynamic lubrication problems. The first one is based on the solution of the Navier-Stokes equations and allows an accurate analysis of the fluid behaviour, at the expense of higher computational cost and complexity. The other method is based on the Reynolds equation which is an integrated version of Navier-Stokes equation across the film thickness. This second approach has been widely employed in lubrication studies because it combines good accuracy of the solution and low computational cost.
The Reynolds equation is derived from the Navier-Stokes equations under the following assumptions:

- Inertial and body forces are negligible
- Pressure and viscosity are constant through the lubricant film
- The lubricant flow is laminar
- No slip at the boundary surfaces
- Viscous forces are dominant, while the inertial and surface tension forces are negligible
- Shear stress and velocity gradients are only significant across the lubricant film
- The lubricant is a Newtonian fluid
- The lubricant boundary surfaces are parallel or at a small angle with respect to each other

These assumptions are usually encountered in common lubrication problems and, therefore, the Reynolds equation can be employed to obtain an accurate solution.

The Navier-Stokes equations allow to investigate the property of the fluid along the direction of the film thickness, whereas the Reynolds equations threat the fluid properties constant along the thickness direction.
The classic formulation of the Reynolds equation in two dimensions is:

$$\frac{\partial}{\partial x}\left[\frac{\rho h^3}{6\mu}\frac{\partial p}{\partial x}\right]+\frac{\partial}{\partial y}\left[\frac{\rho h^3}{6\mu}\frac{\partial p}{\partial y}\right] = \frac{\partial}{\partial x}[\rho h(u_1+u_2)]+\frac{\partial}{\partial x}[\rho h(v_1+v_2)]+2\frac{\partial}{\partial t}(\rho h) \tag{2.1}$$

where ρ is the fluid density, x and y are the spatial coordinates, μ is the fluid viscosity, h is the film thickness, p is the pressure, t is time and u_1, u_2, v_1 and v_2 are the boundary surface speeds in x and y directions.

2.3 Complementarity formulation of the Reynolds equation in presence of cavitation

To solve the cavitation problem, a complementary formulation of the Reynolds equation is adopted. This approach allows to use well known iterative algorithm for the solution of linear complementarity problem, which leads to a solution in few steps. For aim of simplicity, the complementarity formulation will be derived for a one-dimensional domain since the same approach can be easily extended for a two-dimensional domain.
Let ρ_p be the density of the lubricant at the given pressure, and $\rho = \rho(x,t,p)$ the density of the mixture of oil and gases. The domain of the cavitation problem can be divided in two sub-domains: the active region, where no cavitation occurs and ρ equals ρ_p, and the cavitated region, where ρ is always lower than ρ_p. Therefore, the void fraction r, defined as:

$$r = 1-\frac{\rho}{\rho_p} \tag{2.2}$$

is equal to zero in the active region, where the hydrodynamic pressure p is strictly positive, and varies in the range $0 < r < 1$ in the non-active zone, where p is equal to the cavitation pressure p_c. Considering p_c equal to zero, a sign restriction on the value of pressure p arises since $p \geq 0$ in the whole domain. The two variables p and r can therefore be identified as complementarity variables, and complementarity constraints can be written as:

$$\begin{gathered} p \geq 0 \\ r \geq 0 \\ p \cdot r = 0 \end{gathered} \tag{2.3}$$

(note that if $p_c \neq 0$, complementarity subsist between $p - p_c$ and r).
Consider the Reynolds equation in its one-dimensional form for unsteady and compressible flow:

$$\frac{\partial}{\partial x}\left[\frac{\rho h^3}{6\mu}\frac{\partial p}{\partial x}\right] - 2\frac{\partial}{\partial t}[\rho h] - U\frac{\partial}{\partial x}[\rho h] = 0 \tag{2.4}$$

where h is the film thickness, U the sliding speed and μ the fluid viscosity. Eq. (2.4) is valid both in the full film region (active region) and in the cavitated (non-active) region.
For a compressible fluid, density is a function of pressure and it can be explicitly expressed by the general formula:

$$\rho_p = \rho_c f(p) \tag{2.5}$$

where ρ_c is the density at cavitation and $f(p)$ is the functional connection between ρ_p and p.
Introduce the variable Φ such as:

$$\Phi = (\rho_p - \rho) \tag{2.6}$$

Such variable is zero in the active region and varies in the range $0 < \Phi < \rho_p$ in the non-active zone. Normalising Φ using ρ_p, the definition of r, Eqn. (2.2) arises.
Substituting Eq. (2.6) into Eq. (2.4) it is possible to obtain:

$$\frac{\partial}{\partial x}\left[(\rho_c f(p)-\Phi)\frac{h^3}{6\mu}\frac{\partial p}{\partial x}\right]-2\frac{\partial}{\partial t}[(\rho_c f(p)-\Phi)h] - U\frac{\partial}{\partial x}[(\rho_c f(p)-\Phi)h]=0 \tag{2.7}$$

Rearranging Eq. (2.7) as follows:

$$\frac{\partial}{\partial x}\left[\rho_c f(p)\left(1-\frac{\Phi}{\rho_c f(p)}\right)\frac{h^3}{6\mu}\frac{\partial p}{\partial x}\right]-2\frac{\partial}{\partial t}\left[\rho_c f(p)\left(1-\frac{\Phi}{\rho_c f(p)}\right)h\right] - U\frac{\partial}{\partial x}\left[\rho_c f(p)\left(1-\frac{\Phi}{\rho_c f(p)}\right)h\right]=0 \tag{2.8}$$

and noticing that complementarity variable r can be rewritten as:

$$r=\frac{\Phi}{\rho_c f(p)} \tag{2.9}$$

Eq. (2.8) becomes:

$$\frac{\partial}{\partial x}\left[\rho_c f(p)(1-\mathrm{r})\frac{h^3}{6\mu}\frac{\partial p}{\partial x}\right]-2\frac{\partial}{\partial t}[\rho_c f(p)(1-\mathrm{r})h] - U\frac{\partial}{\partial x}[\rho_c f(p)(1-\mathrm{r})h]=0 \tag{2.10}$$

Expanding Eq. (2.10):

$$\frac{\partial}{\partial x}\left[f(p)\frac{h^3}{6\mu}\frac{\partial p}{\partial x}\right]-\frac{\partial}{\partial x}\left[f(p)r\frac{h^3}{6\mu}\frac{\partial p}{\partial x}\right]-2\frac{\partial}{\partial t}[f(p)h]+2\frac{\partial}{\partial t}[f(p)rh] - U\frac{\partial}{\partial x}[f(p)h]+U\frac{\partial}{\partial x}[f(p)rh]=0 \tag{2.11}$$

Let us focus on the term:

$$\frac{\partial}{\partial x}\left[f(p)r\frac{h^3}{6\mu}\frac{\partial p}{\partial x}\right] \tag{2.12}$$

In the non-active region, $\frac{\partial p}{\partial x} = 0$ because the pressure is considered constant and equal to p_c, whereas, in the active region, r, it is equal to zero. The term in Eq. (2.12) is, therefore, equal to zero in the whole domain.

Moreover, the terms containing the product between $f(p)$ and r can be simplified by substituting $f(p) = 1$. In facts, where $r \geq 0$ (the non-active regions), $f(p) = 1$, while, where $f(p) \neq 1, r = 0$.

Therefore, Eq. (2.12) becomes:

$$\frac{\partial}{\partial x}\left[f(p)\frac{h^3}{6\mu}\frac{\partial p}{\partial x}\right] - 2\frac{\partial}{\partial t}[f(p)h] + 2\frac{\partial}{\partial t}[rh] - U\frac{\partial}{\partial x}[f(p)h] + U\frac{\partial}{\partial x}[rh] = 0 \tag{2.13}$$

In conclusion, the cavitation problem can be formulated as follow:

$$\begin{gathered}\frac{\partial}{\partial x}\left[f(p)\frac{h^3}{6\mu}\frac{\partial p}{\partial x}\right] - 2\frac{\partial}{\partial t}[f(p)h] + 2\frac{\partial}{\partial t}[rh] - U\frac{\partial}{\partial x}[f(p)h] + U\frac{\partial}{\partial x}[rh] = 0 \\ p \geq 0 \\ r \geq 0 \\ p \cdot r = 0\end{gathered} \tag{2.14}$$

Since no assumption has been made about $f(p)$, any compressibility models available in pertinent literature can be employed.

2.3.1 Compressibility, piezoviscosity and non-Newtonian behaviour of fluids

The formulation described by Eq.(2.14) can be suitably modified to consider more fluid realistic behaviour, including the variation of the viscosity as a function of pressure (piezoviscosity) and of the shear rate (non-Newtonian behaviour) and the dependency of density on pressure (compressibility).

To handle fluid compressibility, is it possible to employ different formulation of $f(p)$, that can be found in literature.

In [23], Vijayaraghavan and Keith employed a constant fluid bulk modulus formulation to analyse the behaviour of compressible fluids in finite journal bearings. However, in real lubricants the bulk modulus depends on density and this formulation is valid only in a limited range of pressure [24].

In [28] Dowson and Higginson proposed a more complete formulation, that is in good agreement with experimental results for pressure values up to 400 MPa [29]. Two constant coefficients are introduced that depend on the specific lubricant. The value of this coefficients was investigated in [24] to best fit the experimental data for mineral oil found in [30].

Jacobson and Vinet [31] proposed a relation between pressure and density that shows the best results even for very high pressure values. The relation is not analytically invertible, but iterative method such as Newton-Raphson method, can be employed to evaluate density at given pressure [32].

By properly updating the value of viscosity in Eq. (2.14), is it possible to consider the influence of pressure (piezoviscous effect) and shear rate (non-Newtonian behaviour). In particular, the viscosity can be evaluated as a function of pressure starting from the value μ_0 that characterises the fluid at low pressures and shear rates. Typically adopted relation can be found in [33], modified by Roelands in [34] to better fit the experimental data of pressure effect on viscosity under isothermal conditions, and in [35].

Piezoviscosity helps the fluid to sustain the external load, and can stabilise the motion of the components supported by the formation of the fluid film [36]. On the other hand, introducing the variation of viscosity as a function of pressure could lead to instability, being the viscosity a function of pressure in a way that increase of pressure causes an increase of viscosity and considering that, at given film profile, the higher is the viscosity the higher is the pressure. One way to achieve this is to consider the shear thinning behaviour of the lubricant. Since the shear rate is affected by both the sliding speed and the pressure gradient within the fluid, this second relation has the capability to limit the pressure rise due to piezoviscosity and to stabilise the numerical solution to finite values. Relation proposed to correct the viscosity value in order to consider this effect can be found in [37].

2.3.2 Functional connection between the complementarity variables

Let us consider, merely to simplify the discussion, the one-dimensional steady state Reynolds equation for compressible and non isoviscous fluids in pure sliding:

$$\frac{\partial}{\partial x}\left[f(p)\frac{h^3}{6\mu}\frac{\partial p}{\partial x}\right] - U\frac{\partial}{\partial x}[f(p)h] + U\frac{\partial}{\partial x}[rh] = 0 \tag{2.15}$$

Integrating twice with respect to x gives:

$$p = -6\mu U\int_0^x \frac{r}{f(p)h^2}dy + 6\mu U\int_0^x \frac{1}{h^2}dy + 6\mu A_1\int_0^x \frac{1}{f(p)h^3}dy + A_2 \tag{2.16}$$

Considering the following boundary conditions:

$$p(0) = p_0; p(a) = p_a \tag{2.17}$$

where a is the lubricated contact length and p_0 and p_a represent the inlet and the outlet pressure, respectively, we can easily determine the value of the constants of integration, A_1 and A_2:

$$A_1 = \frac{(p_a - p_0) + 6\mu U\int_0^a \frac{r}{f(p)h^2}dy - 6\mu U\int_0^a \frac{dy}{h^2}}{6\mu\int_0^a \frac{dy}{f(p)h^3}}$$
$$A_2 = p_0 \tag{2.18}$$

Substituting A_1 and A_2:

$$p = -6\mu U \int_0^x \frac{r}{f(p)h^2}dy + 6\mu U \int_0^x \frac{dy}{h^2} + \frac{(p_a - p_0) + 6\mu U \int_0^a \frac{r}{f(p)h^2}dy - 6\mu U \int_0^a \frac{dy}{h^2}}{\int_0^a \frac{dy}{f(p)h^3}} \int_0^x \frac{1}{f(p)h^3}dy + p_0 \tag{2.19}$$

Eq. (2.19) can be written in the following compact form:

$$p = Lr + Q \tag{2.20}$$

Where L represent the operator relating the complementarity variables p and r, and Q is the term that carries the information about boundary conditions of the problem and the shape of the lubricant domain film thickness.

The linear complementarity problem Eq.(2.20) can be numerically solved using different approaches, in this thesis the Galerkin method in the Finite Element Framework [38] is adopted.

2.4 Numerical Implementation

In this section, the Finite Element implementation of the formulation presented in Section 2.3 is derived for a two dimensional domain:

$$\frac{\partial}{\partial x}\left[f(p)\frac{h^3}{6\mu}\frac{\partial p}{\partial x}\right] + \frac{\partial}{\partial y}\left[f(p)\frac{h^3}{6\mu}\frac{\partial p}{\partial y}\right] - 2\frac{\partial}{\partial t}[f(p)h] + 2\frac{\partial}{\partial t}(rh) - U\frac{\partial}{\partial x}[f(p)h] + U\frac{\partial}{\partial x}(rh) - U\frac{\partial}{\partial y}[f(p)h] + U\frac{\partial}{\partial y}(rh) = 0 \tag{2.21}$$

Eq.(2.21) can be solved numerically using the Galerkin method:

$$\int_{\Omega} W\left[\frac{\partial}{\partial x}\left(f(p)\frac{h^3}{6\mu}\frac{\partial p}{\partial x}\right)+\frac{\partial}{\partial y}\left(f(p)\frac{h^3}{6\mu}\frac{\partial p}{\partial y}\right)-2\frac{\partial}{\partial t}(f(p)h)+2\frac{\partial}{\partial t}(rh)\right.$$
$$-U_x\frac{\partial}{\partial x}(f(p)h)-U_y\frac{\partial}{\partial y}(f(p)h)+U_x\frac{\partial}{\partial x}(rh) \qquad (2.22)$$
$$\left.+U_y\frac{\partial}{\partial y}(rh)\right]d\Omega=0$$

where Ω is the lubrication domain W is the test function.

When evaluating the diffusion terms, an integration by parts is generally introduced:

$$\int_{\Omega} W\frac{\partial}{\partial x}\left(f(p)\frac{h^3}{6\mu}\frac{\partial p}{\partial x}\right)d\Omega = W\left(f(p)\frac{h^3}{6\mu}\frac{\partial p}{\partial x}\right)\Big|_{\Omega_0}-\int_{\Omega}\left(f(p)\frac{h^3}{6\mu}\frac{\partial W}{\partial x}\frac{\partial p}{\partial x}\right)d\Omega \qquad (2.23)$$

$$\int_{\Omega} W\frac{\partial}{\partial y}\left(f(p)\frac{h^3}{6\mu}\frac{\partial p}{\partial y}\right)d\Omega = W\left(f(p)\frac{h^3}{6\mu}\frac{\partial p}{\partial y}\right)\Big|_{\Omega_0}-\int_{\Omega}\left(f(p)\frac{h^3}{6\mu}\frac{\partial W}{\partial y}\frac{\partial p}{\partial y}\right)d\Omega \qquad (2.24)$$

These integrations by parts lead to a weak form of Eq.(2.22). The two first right hand side terms of Eq.(2.23) and Eq.(2.24) should be evaluated on the domain boundaries. However, these terms can be neglected because a pressure value is usually prescribed along these boundaries [39]. Expanding all the terms of the Eq.(2.22), and considering Eq. (2.23) and Eq. (2.24), it is possible to obtain:

$$
\begin{aligned}
-\int_{\Omega} \frac{f(p)h^3}{6\mu}\frac{\partial W}{\partial x}\frac{\partial p}{\partial x}d\Omega - \int_{\Omega} \frac{f(p)h^3}{6\mu}\frac{\partial W}{\partial y}\frac{\partial p}{\partial y}d\Omega - \int_{\Omega} W2\frac{\partial (f(p)h)}{\partial t}d\Omega \\
+\int_{\Omega} W2\frac{\partial (rh)}{\partial t}d\Omega - \int_{\Omega} WU_x\frac{\partial (f(p)h)}{\partial x}d\Omega \\
-\int_{\Omega} WU_y\frac{\partial (f(p)h)}{\partial y}d\Omega + \int_{\Omega} WU_x\frac{\partial (rh)}{\partial x}d\Omega \\
+\int_{\Omega} WU_y\frac{\partial (rh)}{\partial y}d\Omega = 0
\end{aligned}
\tag{2.25}
$$

Then the lubrication domain can be divided into a finite number of elements and Eq.(2.25) can be discretized and solved over each element domain Ω_e.

Using proper shape function N_i, a general variable Φ can be evaluated inside each element as:

$$
\Phi \approx \sum_{i=1}^{N_n} N_i \Phi_i \tag{2.26}
$$

where N_n is the number of nodes per element, N_i is the shape function and Φ_i is the value of the variable Φ at node i. For a two-dimensional problem, bilinear shape function can be used:

$$
\begin{aligned}
N_1 &= (1-\xi)(1-\eta)\frac{1}{4} \\
N_2 &= (1+\xi)(1-\eta)\frac{1}{4} \\
N_3 &= (1+\xi)(1+\eta)\frac{1}{4} \\
N_4 &= (1-\xi)(1+\eta)\frac{1}{4}
\end{aligned}
\tag{2.27}
$$

where ξ and η are the element local coordinates. As a consequence, it is possible to obtain:

$$
\frac{\partial \Phi}{\partial x} \approx \sum_{i=1}^{N_n} \frac{\partial}{\partial x} N_i \Phi_i \tag{2.28}
$$

Employing the Gaussian quadrature rule for the numerical integration, the discretized form of Eq.(2.28) on the general j-th node of the element Ω_e becomes:

$$\begin{aligned} F_j(\Omega_e) = & -\sum_{m=1}^{N_{gp}}\left[\sum_{k=1}^{N_n}\frac{{h_m}^3}{6\mu}f(p)_m\left(\frac{\partial N_{mk}}{\partial x}\frac{\partial W_{mj}}{\partial x}+\frac{\partial N_{mk}}{\partial y}\frac{\partial W_{mj}}{\partial y}\right)p_k\right]w_m\,\Delta\Omega_m \\ & +\sum_{m=1}^{N_{gp}}\left[\sum_{k=1}^{N_n}W_{mj}\left(\frac{\partial N_{mk}}{\partial x}r_k h_k\right)(U_x+U_y)\right]w_m\Delta\Omega_m \\ & -\sum_{m=1}^{N_{gp}}\left[W_{mj}\left(\frac{\partial}{\partial x}f(p)_m h_m\right)(U_x+U_y)\right]w_m\Delta\Omega_m \\ & +\frac{2}{\Delta t}\sum_{m=1}^{N_{gp}}\left[\sum_{k=1}^{N_n}W_{mj}N_{mk}\big(r_k(t)h_k(t)-r_k(t-\Delta t)h_k(t-\Delta t)\big)\right]w_m\,\Delta\Omega_m \\ & -\frac{2}{\Delta t}\sum_{m=1}^{N_{gp}}\left[W_{mj}f\big(p(t)\big)_m\big(h_m(t)-h_m(t-\Delta t)\big)\right]w_m\,\Delta\Omega_m=0 \end{aligned} \tag{2.29}$$

where the m-index defines a general Gauss point, w_m is the corresponding weight, $\Delta\Omega_m$ is the determinant of the coordinate transformation from the global coordinate system to the local coordinate system, the k-index defines a general element node and N_{gp} and N_n represent the number of Gauss points and nodes for each element, respectively.

Writing Eq.(2.29) for each node of the domain, a system of non-linear algebraic equations is obtained in the following form:

$$[A]p+[B]r+C=0 \tag{2.30}$$

Where:

$$\begin{aligned} A_{j,k} = -\sum_{n=1}^{N_e}\Bigg\{\sum_{m=1}^{N_{gp}}\Bigg[\sum_{k=1}^{N_n}\frac{{h_m}^3}{6\mu}f(p_i-1)_m\Bigg(&\frac{\partial N_{mk}}{\partial x}\frac{\partial W_{mj}}{\partial x} \\ &+\frac{\partial N_{mk}}{\partial y}\frac{\partial W_{mj}}{\partial y}\Bigg)\Bigg]w_m\,\Delta\Omega_m\Bigg\} \end{aligned} \tag{2.31}$$

$$B_{j,k} = -\sum_{n=1}^{N_e}\left\{\sum_{m=1}^{N_{gp}}\left[U_x\sum_{k=1}^{N_n}W_{mj}h_k\left(\frac{\partial N_{mk}}{\partial x}\right) + U_y\sum_{k=1}^{N_n}W_{mj}h_k\left(\frac{\partial N_{mk}}{\partial y}\right) + \frac{2}{\Delta t}\sum_{k=1}^{N_n}W_{mj}N_{mk}h_k(t)\right]w_m\,\Delta\Omega_m\right\} \tag{2.32}$$

$$C_j = -\sum_{n=1}^{N_e}\left\{\sum_{m=1}^{N_{gp}}\left[U_xW_{mj}\frac{\partial}{\partial x}(f(p_i-1)_m h_m) + U_yW_{mj}\frac{\partial}{\partial y}(f(p_i-1)_m h_m\right] + \left[2W_{mj}f(p_i-1)_m\frac{h_m(t)-h_m(t-\Delta t)}{\Delta t} + \frac{2}{\Delta t}W_{mj}\sum_{k=1}^{Nn}[N_{mk}r_k(t-\Delta t)h_k(t-\Delta t)]\right]w_m\,\Delta\Omega_m\right\} \tag{2.33}$$

Consider the matrix $[A]$, which derives from the discretization of the Poiseuille term within the Reynolds equation, Eqn.(2.13). After imposing the boundary conditions in terms of pressure and by inverting matrix $[A]$, one obtains:

$$p = -[A]^{-1}[B]r - [A]^{-1}C \rightarrow p = [L]r + Q \tag{2.34}$$

Where

$$[L] = -[A]^{-1}[B]\ and\ Q = -[A]^{-1}C \tag{2.35}$$

The system of algebraic equations (2.34) can now be solved using a suitable algorithm for complementarity problems.

3. *Elastic deflection*

3.1 Overview

In the case of rigid mating surfaces the lubricant film thickness h is entirely defined by the geometry of the bodies. However, in real applications, such as lubricated contact of engine components, this assumption is no longer acceptable, since the elastic deformation of the components is not negligible and strongly affect the lubrication behavior of the coupling in terms of pressure, void fraction and film thickness.

Figure 3.1 depicts the film thickness and the main symbols employed: h_g is the geometric thickness that correspond to the film thickness in the case of rigid bodies, while h_e is the elastic deflection of the solid surfaces induced by to the fluid pressure.

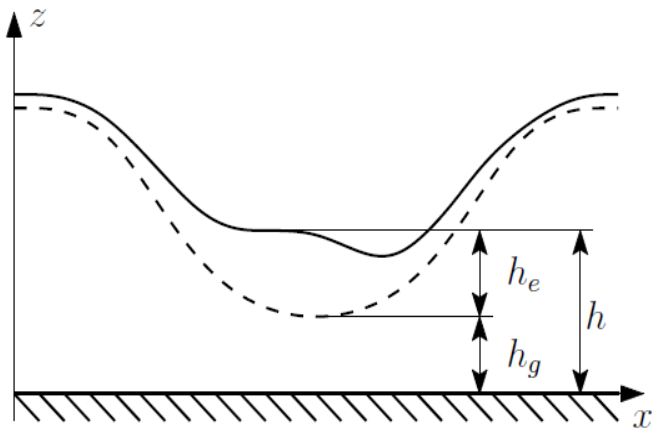

Figure 3.1. Elastic deflection of solid boundary due to fluid film pressure

The influence of the elastic deflection was first investigated in literature focusing on the elastohydrodynamic lubrication of reciprocating rubber seals [40] [41] [42] [43] [44] [45]

[46]. In [47], [48] Field and Nau presented solutions obtained using a direct, or forward iteration scheme in which pressure, deflections, film thickness, and hence pressure are calculated successively. This type of scheme is referred to mathematically by the more general name "*Picard"* or "*functional"* iteration. A high degree of under-relaxation was required between iterations to stabilize the solution, and this resulted in a very large number of iterations. In [49] [50] Rohde and Oh reported a very fast novel and method of solving the elastohydrodynamic equation that employs a Newton iteration scheme.

3.2 Complementarity formulation of the EHL problem

The total film thickness h will be the sum of the geometric film thickness and the elastic deflection of the bodies. Referring to Figure 3.1, is it possible to write:

$$h = h_g + h_e \tag{3.1}$$

Therefore, the HL complementarity formulation of the Reynolds equation in the presence of cavitation presented in Chapter 2 has to be improved to handle the elastic deflections of the contacting bodies. In particular, the EHL complementarity problem can be written as (considering $f(p) = 1$ for the sake of simplicity):

$$\begin{gathered} \frac{\partial}{\partial x}\left[\frac{h(p)^3}{6\mu}\frac{\partial p}{\partial x}\right] - 2\frac{\partial}{\partial t}[h(p)] + 2\frac{\partial}{\partial t}[rh(p)] - U\frac{\partial}{\partial x}[h(p)] + U\frac{\partial}{\partial x}[rh(p)] = 0 \\ h(p) = h_g + h_e = h_g + lp \\ p \geq 0 \\ r \geq 0 \\ p * r = 0 \end{gathered} \tag{3.2}$$

where the total film thickness $h(p)$ is given by the sum of the geometric thickness h_g and the elastic deflection h_e, and l is the linear integral operator that gives the elastic deflection of the solid surfaces h_e as a function of the pressure p. In a discretized domain, it is possible to evaluate the elastic deflection at every point of the domain by an interpolation of the nodal values once proper shape functions have been introduced.

The values of the nodal displacements can be obtained by multiplying a matrix carrying information about the compliance of the domain, C, with the nodal pressures vector, p (i.e. in a discretized geometry the operator l is represented by a compliance matrix of the bodies C reduced to the nodes of the lubricated surfaces).

The non-linear nature of the coupling of the Reynolds equation and the elastic deflection requires the implementation of an iterative procedure. At each step i, h is evaluated with the pressure distribution p_{i-1}, computed at the previous step. Then the Reynolds equation in terms of p and r is solved giving the new pressure distribution p_i. This procedure loops until suitable convergence criteria are satisfied. However, such explicit method is not appropriate for the highly non-linear (stiff) behaviour of the system of Eq.(3.2), which describes the EHL problem.

Convergence issues arise and proper under-relaxation factors are required. Nevertheless, the introduction of under-relaxation techniques increases the computational cost and the time required to obtain the numerical solution. Moreover, the convergence is far from being guaranteed. Therefore, a suitable form of the Newton method has been introduced to tackle this problem.

4. Asperity contact problem

4.1 Overview

When the load capacity of the fluid film is not able to sustain the external loads, a direct contact between the solid surfaces asperities of the lubricated bodies occurs. In this case, the supporting load is provided partly by the hydrodynamic oil film pressure and partly by the asperities direct contact pressure. This lubrication regime is well known as the *mixed lubrication* regime.

When two macroscopically flat bodies with micro-roughness come in contact, the contact occurs at multiple asperities of arbitrary shapes, and varying sizes and heights. Deformation occurs in the region of the contact spots, establishing stresses that oppose the applied load. The sum of the areas of all the contact spots constitutes the real (true) area of contact, and for most materials with applied load, this will be only a small fraction of the apparent (nominal) area of contact (that which would occur if the surfaces were perfectly smooth). When two surfaces move relative to each other, the adhesion of these asperities and other sources of surface interactions contribute to friction force. Repeated surface interactions and surface and subsurface stresses, developed at the interface, result in the formation of wear particles and eventual failure. Thus, the contact modelling of two rough surfaces is of considerable interest in the study of friction and wear [51], [52] [53].

Modelling of the contact of rough surfaces is difficult and has been treated in many papers using a number of approaches over the past three decades. The difficulty in the development of a theoretical model is that the surface is a random structure and may be anisotropic, so that stochastic models must be used. The classical statistical model for a combination of elastic and plastic contacts between rough surfaces is that proposed by Greenwood and Williamson in [54], and deepened by Greenwood and Tripp in [12], which assumes that surfaces are

composed of hemispherically tipped asperities of uniform radius of curvature, with their heights following a gaussian distribution about a mean plane.

Their model was modified by Whitehouse and Archard [55] and Onions and Archard [56]. Nayak [57], Bush et al. [58], Gibson [59] and McCool [60] developed an elastic contact model that treated asperities as elliptical paraboloids with randomly oriented elliptical contact areas. Slight modifications to these models have been presented in several papers (e.g., see [61], [62], [63], [64] [65]). Kotwal and Bhushan [66] developed a statistical model for non-gaussian surfaces.

With the advent of computer technology, a measured surface profile can be digitized and used for computer simulation [67] [68] [69] [70]. Digital maps of pairs of different surfaces can be brought together to simulate contact inside the computer and contours of contacts can be predicted. In computer simulations, the resulting contour maps can be analylzed to give contact parameters for various interplanar separations of the rough surfaces. However, one still has to select scan size and lateral resolution of the instrument relevant for the interface problem on hand [71].

Several numerical techniques have been developed and used to solve contact problems of rough surfaces numerically. Finite element methods [72] have been used to solve plane-strain elastic contact problems with only a few cylindrical asperities in contact [73]. For 3-D rough surface contact problems with many asperities of arbitrary shape, requirements of large number of mesh elements make the finite element approach unfeasible. One of the techniques provides a deterministic solution to stresses and areas for the approach of two real rough surfaces [74] [75] [76] [77]. This technique takes full account of the interaction of deformation from all contact points and predicts the contact geometry of real surfaces under loading. It provides useful information on the contact pressure, number of contacts, their sizes and distributions, and the spacing between contacts.

In this activity, two different approach to the asperity contact problem were implemented to mimic the mixed lubrication condition: the first based on a standard Greenwood Tripp theory and the latter based on a complementarity formulation of the direct metal to metal contact problem and on the Finite Element Method [78] [79] [80].

4.2 Complementarity formulation of the asperity contact problem

4.2.1 Finite Element contact model

If we consider a constrained body, that is a body with no rigid body motions, it is possible to extract the compliance matrix of the contact nodes via static reduction of the complete stiffness matrix. The equation governing the static problem $(\ddot{x} = \dot{x} = 0)$ reduces to:

$$\underline{\underline{K}} \cdot \overline{x} = \bar{F} \tag{4.1}$$

Figure 4.1 sketches the FE models of two bodies in contact: A and B. For each body there is a subset of nodes, b_A and b_B, which are the boundary nodes and are marked in red. The interior nodes, i_A and i_B, are depicted in blue.

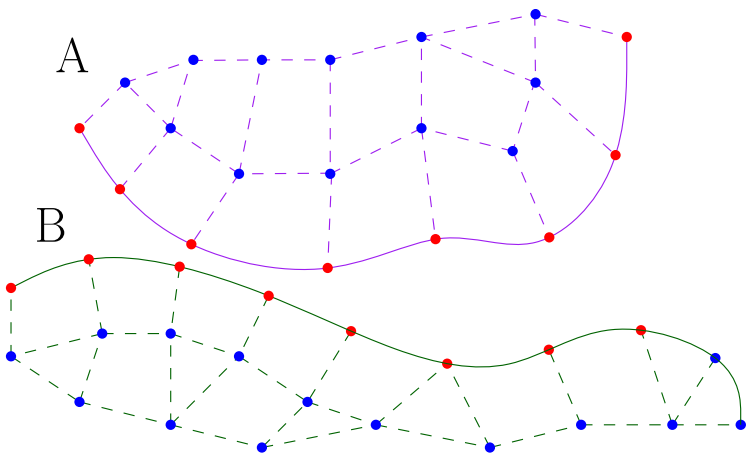

Figure 4.1. Schematic of two contact bodies. The red nodes are contact (boundary) nodes while the blue ones are interior nodes

Consider the stiffness matrix $\underline{\underline{K_A}}$ of the contact body A. It is possible to partition the stiffness matrix as follows:

$$\underline{\underline{K_A}} = \begin{bmatrix} \underline{\underline{K_{bb}}} & \underline{\underline{K_{bi}}} \\ \underline{\underline{K_{ib}}} & \underline{\underline{K_{ii}}} \end{bmatrix} \tag{4.2}$$

$$\begin{bmatrix} \underline{\underline{K_{bb}}} & \underline{\underline{K_{bi}}} \\ \underline{\underline{K_{ib}}} & \underline{\underline{K_{ii}}} \end{bmatrix} \begin{bmatrix} \overline{x_b} \\ \overline{x_i} \end{bmatrix} = \begin{bmatrix} \overline{F_b} \\ \overline{F_i} \end{bmatrix} \tag{4.3}$$

where the subscript b refers to the boundary nodes and the subscript i to the interior nodes. If the bodies are at rest and the only load applied to the system is the contact force, it follows that the external force on the inner nodes is:

$$\overline{F_i} = 0 \tag{4.4}$$

Moreover, only x_b is desired. Writing out the set of equations from Eqn.(4.3):

$$\begin{cases} \underline{\underline{K_{bb}}} \cdot \overline{x_b} + \underline{\underline{K_{bi}}} \cdot \overline{x_i} = \overline{F_b} \\ \underline{\underline{K_{ib}}} \cdot \overline{x_b} + \underline{\underline{K_{ii}}} \cdot \overline{x_i} = \overline{0} \end{cases} \tag{4.5}$$

The second equation can be rearranged as:

$$-\underline{\underline{K_{ii}}}^{-1} \cdot \underline{\underline{K_{ib}}} \cdot \overline{x_b} = \overline{x_i} \tag{4.6}$$

Substituting Eqn.(4.5) into Eqn.(4.6):

$$\underline{\underline{K_{bb}}} \cdot \overline{x_b} - \underline{\underline{K_{bi}}} \cdot \underline{\underline{K_{ii}}}^{-1} \cdot \overline{x_b} = \overline{x_i} \tag{4.7}$$

In matrix form:

$$\underline{\underline{K_{red,A}}} \cdot \overline{x_b} = \overline{F_b} \tag{4.8}$$

Where

$$\underline{\underline{K_{red,A}}} = \underline{\underline{K_{bb}}} - \underline{\underline{K_{bi}}} \cdot \underline{\underline{K_{ii}}}^{-1} \cdot \underline{\underline{K_{ib}}} \tag{4.9}$$

Note the matrix inversion. This requires a non-singular stiffness sub-matrix. The matrix $\underline{\underline{K_{red,A}}}$ has to be inverted to obtain the compliance matrix $\underline{\underline{C_A}}$ that links the forces to the deformations between the contact nodes.

$$\underline{\underline{C_A}} = \underline{\underline{K_{red,A}}}^{-1} \tag{4.10}$$

The compliance matrices of the two touching bodies are summed element-wise to obtain the total compliance:

$$\underline{\underline{C}} = \underline{\underline{C_A}} + \underline{\underline{C_B}} \tag{4.11}$$

4.2.2 LCP formulation of direct asperity contact

The linear complementarity formulation of the asperity contact problem, first presented in [11] is summarized in the following for the sake of clarity.

Consider the case shown in Figure 4.2, occurred at an iterative step of the EHL problems solving algorithm proposed in the previous sections. Let h_0 be the film height at which asperity contact occurs (considered null in the figure).

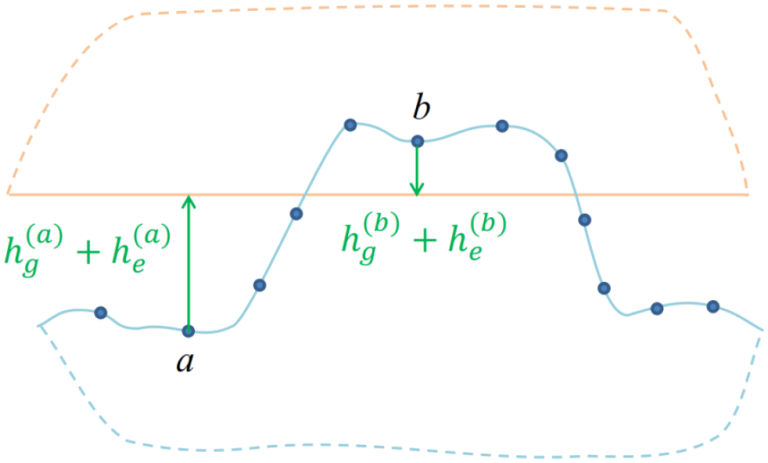

Figure 4.2. Iterative step solution in which asperity contact problem must be solved.

Considering the a node, the solution of the hydro-elastic problem gives:

$$h^{(a)} = h_g^{(a)} + h_e^{(a)} > h_0 \tag{4.12}$$

For that node, the asperity contact pressure $p_a^{(a)}$ will be, therefore, null.
On the other side, for the node b:

$$h^{(b)} = h_g^{(b)} + h_e^{(b)} < h_0 \tag{4.13}$$

so that a non-null (and positive) asperity contact pressure $p_a^{(b)}$ exist, such that:

$$[\underline{\underline{C}} \cdot \overline{p}_a]^{(b)} = -(h_g^{(b)} + h_e^{(b)} - h_0) \tag{4.14}$$

Complementarity variables can be identified considering the asperity contact pressure, p_a, and the gap between the surfaces' asperities, $h - h_0$. In fact, if the film thickness h is higher than the critical value h_0, no direct contact occurs and so p_a equals zero while $h - h_0$ is greater than zero. On the contrary, when the film thickness h reaches the critical value h_0, a direct contact occurs and therefore, $h - h_0$ equals zero while p_a is greater than zero.
The asperity contact linear complementarity problem can be, therefore, written as:

$$\begin{gathered}\overline{h}_{ray,dry} = \overline{h} - h_0 = \overline{h}_g + \underline{\underline{C}} \cdot \overline{p} + \underline{\underline{C}} \cdot \overline{p}_a - h_0 \\ \overline{p}_a \geq \overline{0} \\ \overline{h}_{ray,dry} \geq \overline{0} \\ \overline{p}_a^T \cdot \overline{h}_{ray,dry} = \overline{0}\end{gathered} \tag{4.15}$$

where h_g is the geometric film thickness, that is the thickness calculated considering the nominal surface geometries in the case of rigid bodies, C is the compliance matrix describing the elastic behavior of the assembly and p is the hydrodynamic pressure.

The solution of the problem (4.15) allows to correct the value of $\overline{h}$ obtained solving the pure elasto-hydrodynamic problem, in order to consider the asperity contact. Is it possible to define a new variable,

$$\overline{h}_{dry} = \overline{h}_{ray,dry} + h_0 - \overline{h}_e - \overline{h}_g = [\underline{\underline{C}} \cdot \overline{p}_a] \tag{4.16}$$

representing the portion of elastic deformation due to solid to solid contact. Figure 4.3 depicts the case of Figure 4.2, in which the value of calculated oil film thickness were updated considering the solution of problem (4.15) .

The composite arithmetic average roughness of the two mating surfaces, R_a, can be employed to estimate the value of h_0:

$$h_0 = R_{a1} + R_{a2} \tag{4.17}$$

being R_{a1} and R_{a2} the arithmetic average roughness of the two surfaces.

This formulation allows to solve the non-linear asperity contact problem adopting suitable pivoting algorithms developed for the solution of complementarity problems [81] capable to find out a solution in a finite number of steps without the need of any convergence criteria.

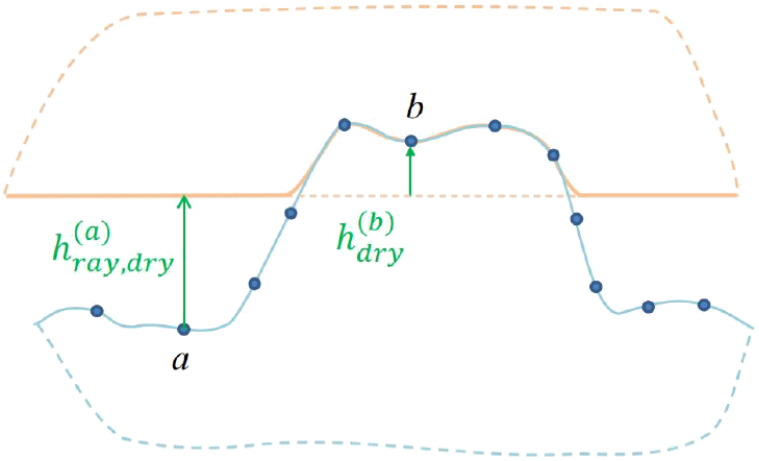

Figure 4.3. Update of *h* considering the solution of the asperity contact problem

4.2.3 Newton method for EHL problems

The Newton method introduced in section 3.2, developed considering the asperity contact problem, is here described.

To unfold the mathematical theory of the Newton method applied to the EHL problem, we will start again with the Reynolds equation in one dimension for incompressible and isoviscous fluids. These restrictions are made for brevity, but the same outline can be followed with the Reynolds equation for a compressible, piezoviscous and shear thinning lubricant.

This equation is coupled with the elastic deflection equation. This set of equations is:

$$\begin{cases} \dfrac{\partial}{\partial x}\left(\dfrac{h^3}{6\mu}\dfrac{\partial p}{\partial x}\right) - 2\dfrac{\partial h}{\partial t} + 2\dfrac{\partial (rh)}{\partial t} - U\dfrac{\partial h}{\partial x} + U\dfrac{\partial (rh)}{\partial x} = 0 \\ h = h_g + h_e + h_{dry} \end{cases} \tag{4.18}$$

Let M be the linear integral operator linking the variable p and p_a, so that:

$$p_a = Mp + N \tag{4.19}$$

The way M and N are evaluated will be shown later. Is it possible to write:

$$h = h_g + h_e + h_{dry} = h_g + Cp + Cp_a = h_g + Cp + CMp + CN \\ = \left(h_g + CN\right) + (C + CM)p = h_g^* + C^* p \tag{4.20}$$

Eq. (4.18) becomes:

$$\frac{\partial}{\partial x}\left[\frac{\left(h_g^* + C^* p\right)^3}{6\mu}\frac{\partial p}{\partial x}\right] - 2\frac{\partial\left(h_g^* + C^* p\right)}{\partial t} + 2\frac{\partial\left[r\left(h_g^* + C^* p\right)\right]}{\partial t} \\ - U\frac{\partial\left(h_g^* + C^* p\right)}{\partial x} + U\frac{\partial\left[r\left(h_g^* + C^* p\right)\right]}{\partial x} = 0 \\ h = h_g^* + C^* p \tag{4.21}$$

Following the Rohde's formulation [49],the system of equation can be written as nonlinear integro-differential operator equation for p

$$F(p) = 0 \tag{4.22}$$

The problem (4.22) is solved adopting a suitable Newton method:

$$F(p_s) + F'(p_s)\varepsilon_s = 0 \tag{4.23}$$

Where $\varepsilon = p_{s+1} - p_s$ is the error and F' is the functional derivative, or Frechet – Gateaux derivative, of F, defined by:

$$F'(p)\varepsilon = \frac{d}{d\delta}F(p + \delta\varepsilon)\Big|_{\delta=0} \tag{4.24}$$

By substitution of p with $p + \delta\varepsilon$ in Eq (4.21), one obtains:

$$F(p+\delta\varepsilon) = \frac{\partial}{\partial x}\left[\frac{\left(h_g^* + C^*(p+\delta\varepsilon)\right)^3}{6\mu}\frac{\partial(p+\delta\varepsilon)}{\partial x}\right] - 2\frac{\partial\left(h_g^* + C^*(p+\delta\varepsilon)\right)}{\partial t} + 2\frac{\partial\left[r\left(h_g^* + C^*(p+\delta\varepsilon)\right)\right]}{\partial t} - U\frac{\partial\left(h_g^* + C^*(p+\delta\varepsilon)\right)}{\partial x} + U\frac{\partial\left[r\left(h_g^* + C^*(p+\delta\varepsilon)\right)\right]}{\partial x} \tag{4.25}$$

Deriving with respect to δ :

$$\begin{aligned}\frac{d}{d\delta}[F(p+\delta\varepsilon)] &= \frac{\partial}{\partial x}\frac{1}{6\mu}\left[3\left(h_g^* + C^*(p+\delta\varepsilon)\right)^2 C^*\varepsilon\frac{\partial(p+\delta\varepsilon)}{\partial x}\right] \\ &+ \frac{\partial}{\partial x}\frac{1}{6\mu}\left[\left(h_g^* + C^*(p+\delta\varepsilon)\right)^3\frac{\partial\varepsilon}{\partial x}\right] - 2\frac{\partial(C^*\varepsilon)}{\partial t} \\ &+ 2\frac{\partial[r(C^*\varepsilon)]}{\partial t} - U\frac{\partial(C^*\varepsilon)}{\partial x} + U\frac{\partial[r(C^*\varepsilon)]}{\partial x}\end{aligned} \tag{4.26}$$

That imposing $\delta = 0$ gives:

$$\begin{aligned}F'(p)*\varepsilon &= \frac{d}{d\delta}[F(p+\delta\varepsilon)]\Big|_{\delta=0} \\ &= \frac{\partial}{\partial x}\frac{1}{6\mu}\left[3\left(h_g^* + C^*p\right)^2 C^*\varepsilon\frac{\partial p}{\partial x}\right] + \frac{\partial}{\partial x}\frac{1}{6\mu}\left[\left(h_g^* + C^*p\right)^3\frac{\partial\varepsilon}{\partial x}\right] \\ &- 2\frac{\partial(C^*\varepsilon)}{\partial t} + 2\frac{\partial[r(C^*\varepsilon)]}{\partial t} - U\frac{\partial(C^*\varepsilon)}{\partial x} + U\frac{\partial[r(C^*\varepsilon)]}{\partial x}\end{aligned} \tag{4.27}$$

So, the Newton method (4.23) can be written as:

$$\begin{aligned}
&\frac{\partial}{\partial x}\left[\frac{\left(h_g^* + C^* p\right)^3}{6\mu}\frac{\partial p}{\partial x}\right] - 2\frac{\partial\left(h_g^* + C^* p\right)}{\partial t} + 2\frac{\partial\left[r\left(h_g^* + C^* p\right)\right]}{\partial t} \\
&\quad - U\frac{\partial\left(h_g^* + C^* p\right)}{\partial x} + U\frac{\partial\left[r\left(h_g^* + C^* p\right)\right]}{\partial x} \\
&\quad + \frac{\partial}{\partial x}\frac{1}{6\mu}\left[3\left(h_g^* + C^* p\right)^2 C^* \varepsilon\frac{\partial p}{\partial x}\right] + \frac{\partial}{\partial x}\frac{1}{6\mu}\left[\left(h_g^* + C^* p\right)^3\frac{\partial \varepsilon}{\partial x}\right] \\
&\quad - 2\frac{\partial(C^*\varepsilon)}{\partial t} + 2\frac{\partial[r(C^*\varepsilon)]}{\partial t} - U\frac{\partial(C^*\varepsilon)}{\partial x} + U\frac{\partial[r(C^*\varepsilon)]}{\partial x} = 0
\end{aligned} \tag{4.28}$$

Simplifying:

$$\begin{aligned}
&\frac{\partial}{\partial x}\left[\frac{\left(h_g^* + C^* p\right)^3}{6\mu}\frac{\partial(p+\varepsilon)}{\partial x}\right] - 2\frac{\partial\left[h_g^* + C^*(p+\varepsilon)\right]}{\partial t} + 2\frac{\partial\left[r\left(h_g^* + C^*(p+\varepsilon)\right)\right]}{\partial t} \\
&\quad - U\frac{\partial\left[h_g^* + C^*(p+\varepsilon)\right]}{\partial x} + U\frac{\partial\left[r\left(h_g^* + C^*(p+\varepsilon)\right)\right]}{\partial x} \\
&\quad + \frac{\partial}{\partial x}\frac{1}{6\mu}\left[3\left(h_g^* + C^* p\right)^2 C^* \varepsilon\frac{\partial p}{\partial x}\right] = 0
\end{aligned} \tag{4.29}$$

Let us focus on the last term of Eq. (4.29). Considering that:

$$\varepsilon = \varepsilon + p - p \tag{4.30}$$

is it possible to obtain:

$$\begin{aligned}
&\frac{\partial}{\partial x}\left[\frac{\left(h_g^* + C^* p\right)^3}{6\mu}\frac{\partial(p+\varepsilon)}{\partial x}\right] - 2\frac{\partial\left[h_g^* + C^*(p+\varepsilon)\right]}{\partial t} + 2\frac{\partial\left[r\left(h_g^* + C^*(p+\varepsilon)\right)\right]}{\partial t} \\
&\quad - U\frac{\partial\left[h_g^* + C^*(p+\varepsilon)\right]}{\partial x} + U\frac{\partial\left[r\left(h_g^* + C^*(p+\varepsilon)\right)\right]}{\partial x} \\
&\quad + \frac{\partial}{\partial x}\frac{1}{6\mu}\left[3\left(h_g^* + C^* p\right)^2 C^*(p+\varepsilon)\frac{\partial p}{\partial x}\right] \\
&\quad - \frac{\partial}{\partial x}\frac{1}{6\mu}\left[3\left(h_g^* + C^* p\right)^2 C^* p\frac{\partial p}{\partial x}\right] = 0
\end{aligned} \tag{4.31}$$

The terms of Eq. (4.31) containing both p and r can be evaluated considering that $p + \varepsilon \cong p$, so:

$$\begin{aligned}
&\boxed{\frac{\partial}{\partial x}\left[\frac{\left(h_g^* + C^* p\right)^3}{6\mu}\frac{\partial(p+\varepsilon)}{\partial x}\right]} - 2\frac{\partial\left[h_g^* + C^*(p+\varepsilon)\right]}{\partial t} + 2\frac{\partial\left[r\left(h_g^* + C^* p\right)\right]}{\partial t} \\
&\quad - U\frac{\partial\left[h_g^* + C^*(p+\varepsilon)\right]}{\partial x} + U\frac{\partial\left[r\left(h_g^* + C^* p\right)\right]}{\partial x} \\
&\quad + \boxed{\frac{\partial}{\partial x}\frac{1}{6\mu}\left[3\left(h_g^* + C^* p\right)^2 C^*(p+\varepsilon)\frac{\partial p}{\partial x}\right]} \\
&\quad - \boxed{\frac{\partial}{\partial x}\frac{1}{6\mu}\left[3\left(h_g^* + C^* p\right)^2 C^* p\frac{\partial p}{\partial x}\right]} = 0
\end{aligned} \tag{4.32}$$

The numerical implementation is similar to the one shown in section 2.4 for the hydrodynamic problem. In applying the Galerkin method, the terms highlighted in the boxes of Eq.(4.32) are integrated by parts.

4.2.4 Correlation between hydrodynamic and asperity contact pressure

In this section, the way the terms *M* and *N* of eq. (4.19) are evaluated is shown. Consider the LCP formulation of the asperity contact problem

$$\begin{gathered}
\overline{h}_{ray,dry} = \underline{\underline{C}} \cdot \overline{p}_a + \left[\overline{h}_g + \overline{h}_e - h_0\right] \\
\overline{p}_a \geq \overline{0} \\
\overline{h}_{ray,dry} \geq \overline{0} \\
\overline{p}_a^T \cdot \overline{h}_{ray,dry} = \overline{0}
\end{gathered} \tag{4.33}$$

That can be written as:

$$\underline{\underline{I}} \cdot \overline{h}_{ray,dry} - \underline{\underline{C}} \cdot \overline{p}_a = \underline{\underline{L}} \cdot \overline{B} = \left[\overline{h}_g + \overline{h}_e - h_0\right] \tag{4.34}$$

Where $\underline{\underline{L}}$ is a matrix whose i-th column is the i-th column of the identity matrix $\underline{\underline{I}}$, if $\left[\overline{h}_{ray,dry}\right]_i > 0$ and then $\left[\overline{p}_a\right]_i = 0$, or the i-th column of the matrix $-\underline{\underline{C}}$, if $\left[\overline{h}_{ray,dry}\right]_i = 0$ and then $\left[\overline{p}_a\right]_i > 0$, while $\overline{B}$ is a vector whose i-th element holds $\left[\overline{h}_{ray,dry}\right]_i$ if $\left[\overline{h}_{ray,dry}\right]_i > 0$ and then $\left[\overline{p}_a\right]_i = 0$, or $\left[\overline{p}_a\right]_i$, if $\left[\overline{h}_{ray,dry}\right]_i = 0$ and then $\left[\overline{p}_a\right]_i > 0$.

Therefore, knowing the solution of problem (4.37), it is easy to obtain the matrix $\underline{\underline{L}}$.

From eq.(4.38):

$$\overline{B} = \underline{\underline{L}}^{-1} \cdot \left[\overline{h}_g + \overline{h}_e - h_0\right] \tag{4.35}$$

Let $\underline{\underline{L}}^{-1^*}$ be the matrix obtained from $\underline{\underline{L}}^{-1}$, by substitution of its i-th row with a null row, if $\left[\overline{h}_{ray,dry}\right]_i > 0$. It follows:

$$\begin{aligned} \overline{p}_a &= \underline{\underline{L}}^{-1^*} \cdot \left[\overline{h}_g + \overline{h}_e - h_0\right] = \underline{\underline{L}}^{-1^*} \cdot \left[\overline{h}_g + \underline{\underline{C}} \cdot \overline{p} - h_0\right] \\ &= \underbrace{\underline{\underline{L}}^{-1^*} \cdot \underline{\underline{C}}}_{\underline{\underline{M}}} \cdot \overline{p} + \underbrace{\underline{\underline{L}}^{-1^*} \cdot \left[\overline{h}_g - h_0\right]}_{\underline{\underline{N}}} = \underline{\underline{M}} \cdot \overline{p} + \overline{N} \end{aligned} \tag{4.36}$$

4.3 Greenwood/Tripp fundamentals

The LCP approach to the asperity contact problems has the advantage of stability, robustness and simplicity in set up, but it does not take into account the peculiar characteristics of the roughness profiles of the mating surfaces. In fact, according to this formulation, different roughness profiles having the same composite arithmetical average roughness R_a will leads to the same results.

A more common approach to the direct contact problem is to couple the Reynolds equation with the Greenwood/Williamson [54] or Greenwood/Tripp [12] model to relate the distance between the two surfaces and the possible arise of an asperity contact pressure. The roughness

profiles of the surfaces are approximated by a uniform distribution of spherical asperities, in contact with a smooth plane. The distribution of asperity summits is assumed to be Gaussian. The pressure is calculated according to the Hertzian contact theory, resulting in a direct relation between surface gap and asperity contact pressure. This approach, therefore, is sensitive to the specific asperity profile shapes, and needs an accurate knowledge of the whole roughness profile to be properly set.

In particular, the necessary input data are:

- the composite mean summit height δ_s,
- the composite height standard deviation of the asperity summits σ_s,
- the mean radius of the asperity peaks β,
- the peaks density η.

Such data are non-standard roughness parameters, usually not available from common roughness measurement equipment. At its basis, the model considers that, when the two surfaces enter in contact, the asperity heights start to interact, and the resulting asperity contact pressure p_a can be estimated as:

$$p_a = \underbrace{\frac{16\sqrt{2\pi}}{15}(\sigma_s \beta \eta)^2 \sqrt{\frac{\sigma_s}{\beta}}}_{K} E^* F_{5/2}(H_s) \tag{4.37}$$

where E^* is the composite elastic modulus of the contacting bodies and $F_{5/2}$ is a statistical function introduced to match the assumed Gaussian distribution of asperities. In this contribution, the following is employed in order to evaluate $F_{5/2}$ [82]:

$$F_{5/2}(H_s) = \begin{cases} 4.4086 * 10^{-5}(4 - Hs)^{6.804} & , H_s \leq 4 \\ 0 & , H_s > 4 \end{cases} \tag{4.38}$$

A different approximation of the $F_{5/2}$ function can be found in [83].

The non-dimensional summit clearance, H_s, is defined as:

$$H_s = \frac{h - \delta_s}{\sigma_s} \tag{4.39}$$

being h the gap between the two surfaces. The elastic factor K,

$$K = \frac{16\sqrt{2\pi}}{15}(\sigma_s \beta \eta)^2 \sqrt{\frac{\sigma_s}{\beta}} \tag{4.40}$$

can be considered as an indicator of the stiffness of the asperity contact pressure – surfaces gap relation. Figure 4.4 shows three different asperity contact pressure – surfaces gap curves obtained adopting different elastic factor K and same value of σ_s (0.879 μm), δ_s (0.77 μm) and E^* (115.38 GPa).

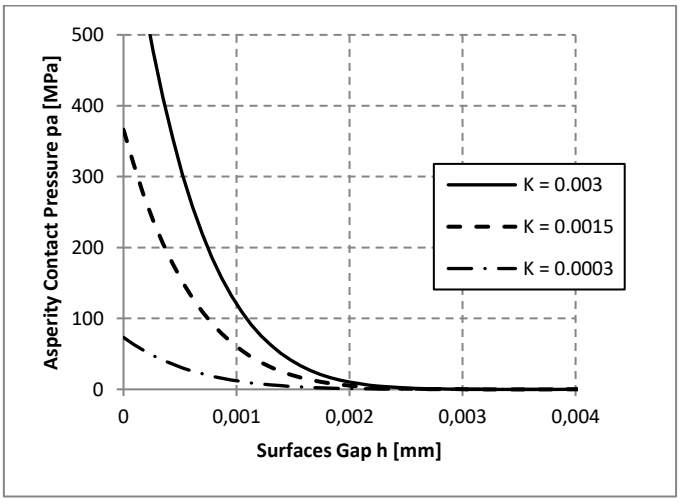

Figure 4.4. Influence of elastic factor on pa-h relation.

Standard values, based on some limited experiences, are typically used in order to set Greenwood/Tripp asperity contact model.

Eq.(4.38) shows how, using Greenwood/Tripp theory, a non-negligible asperity contact pressure is calculated also when h is higher than δ_s. In particular, when h equals $\delta_s + 4\sigma_s$,

the highest asperity summits begin to have a certain probability to touch each other, thus resulting in a contribution of the load carrying capacity given by the asperity contact pressure. Eq.(4.37) cannot be directly employed in order to correct the minimum film thickness as a function of the contact pressure p_a since a severe non linear problem usually arise (especially for low values of the minimum film thickness). In order to tackle this non linearity, numerical techniques are usually employed [84]. In this activity, a Newton method has been introduced. In particular, the direct contact problem:

$$\overline{h} - \overline{h}_g - \overline{h}_e - \underline{\underline{C}} \cdot \overline{p_a}(\overline{h}) = \overline{0} \tag{4.41}$$

has been linearized in the form:

$$\left[\overline{h} - \overline{h}_g - \overline{h}_e - \underline{\underline{C}} \cdot \overline{p_a}(\overline{h})\right]_{\overline{h_k}} + \left[\underline{\underline{I}} - \underline{\underline{C}} \cdot \begin{bmatrix} \ddots & & \\ & \frac{dp_a^{[i]}}{dh^{[i]}} & \\ & & \ddots \end{bmatrix}\right]_{\overline{h_k}} \overline{dh} = \overline{0} \tag{4.42}$$

The method stops when a suitable convergence is reached on p_a.

The asperity contact solver is integrated in the cavitation problem solving algorithm as follow:

1. starting from the knowledge of the geometrical oil film thickness, the cavitation problem is solved and a first attempt value for the hydrodynamic pressure and the void ratio is calculated
2. the oil film thickness is updated considering the elastic deflection of the body due to the first attempt hydrodynamic pressure evaluated
3. with the updated value of oil film thickness, the asperity contact problem is solved adopting the Newton method (4.42), and the total pressure evaluated
4. the method iterates until a suitable convergence is reached on p_{tot}

5. *Linear complementarity problems (LCP) solving algorithms*

5.1 Overview

As shown in previous section, the methodology here presented adopts formulation of both the hydrodynamic and asperity contact problems in terms of linear complementarity problems (LCP) [85].

An n-dimensional LCP is to find a set of vectors $\overline{w} \in R^n$ and $\overline{z} \in R^n$ that satisfy:

$$\overline{w} = \underline{\underline{M}}\overline{z} + \overline{q} \tag{5.1}$$

$$\overline{w} \geq \overline{0}, \overline{z} \geq \overline{0}, \overline{w}^T \overline{z} = \overline{0} \tag{5.2}$$

for a given square matrix $\underline{\underline{M}} \in R^{n \times n}$ and vector $\overline{q} \in R^n$. The condition (5.2) can be denote as:

$$\overline{w} \geq 0 \perp \overline{z} \geq 0 \tag{5.3}$$

LCPs can be solved by either iterative or pivot-based approach. Iterative approaches (e.g. [86]) utilize the fact that the solution of an LCP is the equilibrium point of the associated quadratic cost function and employ numerical root-finding techniques such as Newton's method to find the equilibrium. Pivot-based approaches (such as Lemke Algorithm [87]), on the other hand, sequentially pivot a pair of elements of $\overline{w}$ and $\overline{z}$ according to specific rules until all elements of $\overline{q}$ of the pivoted equation become zero or positive. Once such pivot

sequence is found, we can obtain the pivoted solution by setting $\overline{w} = \overline{q}$, $\overline{z} = \overline{0}$ and then moving the pivoted elements back to the original vectors.

Iterative approaches are generally easier to implement and numerically robust, although convergence is proven only for a limited class of $\underline{\underline{M}}$. Pivot-based approaches are theoretically guaranteed to find a solution with finite number of trials (2^n) for general problems, and several systematic procedures are proposed to efficiently find a solution [85]. However, it is known that pivot-based approaches often suffer from numerical problem especially for large-scale and/or ill-conditioned problems. There have been a body of research on developing efficient and robust methods for solving LCPs in the context of collision/contact modelling. Jourdan et al. [88] applied an iterative LCP solver similar to Gauss-Seidel algorithm to frictional contacts of rigid bodies and proved convergence in most practical cases. Forg et al. [89] utilized the sparsity of $\underline{\underline{M}}$ to accelerate an iterative LCP solver. Stewart et al. [90] formulated frictional contacts between rigid bodies as an LCP and applied Lemke Algorithm. Lloyd [91] also utilized the structure of $\underline{\underline{M}}$ in rigid-body contact model for reducing the computational cost for Lemke Algorithm. Guendelman et al. [92] combined a number of stabilization techniques to obtain visually plausible simulation results for highly complex scenes. All of these papers address contact dynamics between free rigid bodies, in which case $\underline{\underline{M}}$ is generally sparse and the LCP is likely to be relatively easily solved by both iterative and pivot-based approaches.

Lemke Algorithm has been successfully applied to contact problems of articulated rigid bodies by Kry and Pai [93]. The main contribution of this paper is the improvement of Lemke Algorithm to deal with large-scale and ill-conditioned LCPs derived from frictional contacts between articulated rigid bodies of arbitrary geometry.

A well-known extension of Lemke Algorithm is *lexicographic ordering* [85], [94] to solve cycling problem where the same pivot sequence is infinitely repeated when an inappropriate pivot choice is made. The problem is often encountered in ill-conditioned problems and the extension has been employed in [90], [91], [95].

The pivoting algorithm shown in [81], the basic LEMKE method and the FBNS [96] iterative algorithm were implemented in order to solve the LCP problems. The same results can be

obtained adopting the 3 different solvers, with a huge advantage in terms of computational time required for the LCP solving employing the FBNS algorithm.
In the following those methods are summarized for the sake of clarity.

5.2 Pivoting algorithm

The matrix $\underline{\underline{M}}$ of eq. (5.1) is assumed positive semidefinite. Each principal minor of $\underline{\underline{M}}$ is nonnegative since $\underline{\underline{M}}$ is positive semidefinite. This implies:

$$M_{ii} \geq 0, \quad i = 1, \cdots, n \tag{5.4}$$

$$\Delta_{ij} = M_{ii}M_{jj} - M_{ij}M_{ji} \geq 0, \quad i = 1, \cdots, n \tag{5.5}$$

And

$$M_{ij} = -M_{ji} \; if \quad M_{ii}M_{jj} = 0 \tag{5.6}$$

A single principal pivot transform of the system (5.1) in position (i, i) consists in solving the i-th equation of (5.1):

$$w_i = q_i + \sum_{k=1}^{n} M_{ik} z_k \quad M_{ii} > 0 \tag{5.7}$$

for the variable z_i:

$$z_i = M_{ii}^{-1} \left(-q_i + w_i - \sum_{\substack{k=1 \\ k \neq 1}}^{n} M_{ik} z_k \right) \tag{5.8}$$

and substituting this expression of z_i in the other equations of (5.1) which then become:

$$w_l = (q_l - M_{li}M_{ii}^{-1}q_i) + M_{li}M_{ii}^{-1}w_i + \sum_{\substack{k=1 \\ k\neq 1}}^{n}(M_{lk} - M_{li}M_{ii}^{-1}M_{ik})z_k \qquad l = 1,\cdots,n \quad l \neq i. \tag{5.9}$$

The vectors of the dependent and independent variables become respectively:

$$\overline{w}^{*T} = [w_1 \quad w_2 \quad \cdots \quad z_i \quad \cdots \quad w_n] \quad \overline{z}^{*T} = [z_1 \quad z_2 \quad \cdots \quad w_i \quad \cdots \quad z_n] \tag{5.10}$$

A double principal pivot transform of the system (5.1) in the positions (i,j) and (j,i) consists in making the variables z_i, z_j dependent and the variables w_i, w_j independent in system (5.1); the 2×2 minor of $\underline{\underline{M}}$, whose determinant is $\Delta_{ij} > 0$, is employed as a double pivot. From this double substitution

$$z_i = \Delta_{ij}^{-1}\left[-M_{jj}q_i + M_{ij}q_j + M_{jj}w_i - M_{ij}w_j - \sum_{\substack{k=1 \\ k\neq i,k\neq j}}^{n}\left(M_{jj}M_{ik} - M_{ij}M_{jk}\right)z_k\right] \tag{5.11}$$

$$z_j = \Delta_{ij}^{-1}\left[-M_{ii}q_j + M_{ji}q_i + M_{ii}w_j - M_{ji}w_i - \sum_{\substack{k=1 \\ k\neq i,k\neq j}}^{n}\left(M_{jk}M_{ii} - M_{ji}M_{ik}\right)z_k\right] \tag{5.12}$$

$$w_l = q_l + \Delta_{ij}^{-1}\left(-\alpha_{ijl}q_i - \beta_{ijl}q_j + \alpha_{ijl}w_i + \beta_{ijl}w_j\right) + \sum_{\substack{k=1 \\ k\neq i,k\neq j}}^{n}\left(M_{lk} - \Delta_{ij}^{-1}\left(\alpha_{ijl}M_{ik} + \beta_{ijl}M_{jk}\right)\right)z_k \quad l = 1,\dots,n, \quad l \neq i,j \tag{5.13}$$

Where $\alpha_{ijl} = M_{li}M_{jj} - M_{lj}M_{ji} \quad \beta = M_{ii}M_{lj} - M_{li}M_{ij}$

The vectors of the dependent and independent variables become respectively:

$$\begin{aligned} \overline{w}^{*T} &= [w_1 \quad w_2 \quad \cdots \quad z_i \quad \cdots \quad z_j \quad \cdots \quad w_n] \\ \overline{z}^{*T} &= [z_1 \quad z_2 \quad \cdots \quad w_i \quad \cdots \quad w_j \quad \cdots \quad z_n] \end{aligned} \tag{5.14}$$

The new system obtained from (5.1) by means of either transform is expressed as

$$\overline{w}^* = \overline{q}^* - \underline{\underline{M}}^* \cdot \overline{z}^* \tag{5.15}$$

Where $\underline{\underline{M}}^*$ is still positive. By setting $\overline{z} = \overline{0}$ in Eq. (5.1) the solution $[\overline{w}, \overline{z}] = [\overline{q}, \overline{0}]$ is complementary; by setting $\overline{z}^* = \overline{0}$ in Eq.(5.15), $[\overline{w}^*, \overline{z}^*] = [\overline{q}^*, \overline{0}]$ is still a complementary solution for system (5.1).

5.2.1 Properties of pivoting transformation

A single principal pivot transform has the following properties:

1. By virtue of the structure of $\underline{\underline{M}}$ and taking into account eq. (5.9) if $M_{il} = M_{li}$, then $M^*_{il} = -M^*_{li}$; and if $M_{lk} = M_{kl}$ then $M^*_{lk} = M^*_{kl}$.
2. If $q_i < 0$, q^*_i is greater than zero (eq. (5.27)).
3. For each l such that $q_l < 0$, $M_{li} > 0$, $M_{li}^{-1} q_l \geq M_{ii}^{-1} q_i$ it follows from (5.28) that:

$$q^*_l = q_l - M_{li} M_{ii}^{-1} q_i \geq 0 \tag{5.16}$$

A double principal pivot transform has the following properties:

4. Symmetry or skew-symmetry among a pair of entries in symmetric positions with respect to the main diagonal of the matrix $\underline{\underline{M}}$ change according to property 1 with regard to the rows i, j and columns i, j of $\underline{\underline{M}}$; as a consequence, if $M_{ij} = -M_{ji}$, then $M^*_{ij} = -M^*_{ji}$.
5. If $q_i < 0$, then

$$q^*_j = \Delta_{ij}^{-1} M_{ji} q_i > 0 \tag{5.17}$$

Moreover, if $q^*_i > 0$, then

$$q_i^* = \Delta_{ij}^{-1}\left(-M_{jj}q_i + M_{ij}q_j\right) > 0 \tag{5.18}$$

Consider the set

$$\overline{W} = \{w_h | q_h < 0, M_{hh} > 0, 1 \leq h \leq n\} \tag{5.19}$$

and (for each $w_h \in \overline{W}$) the number p_h of negative entries of $\overline{q}$ which become nonnegative owing to a pivot in position (h, h) (property 3). An element of $\overline{W}$ for which p_h assumes its maximum value is referred to as $w_{h'}$.
For an index i ($q_i < 0$) let $M_{ii} > 0$. Then for each index k belonging to the set

$$\overline{K} = \{k | q_k \geq 0, M_{ki} < 0, M_{ii}^{-1}q_i < M_{ki}^{-1}q_k, 1 \leq k \leq n, k \neq i\} \tag{5.20}$$

it follows that $q_k < 0$ by a simple pivot transform in position (i, i). If the set $\overline{K}$ is empty, the pivot transform in position (i, i) leads to a complementary solution $[\overline{w}^*, \overline{z}^*] = [\overline{q}^*, \overline{0}]$ having (at least, prop. 3) a negative entry less ($\overline{q_i}^*$, prop. 2). If the set $\overline{K}$ is nonempty, let $k^* \in \overline{K}$ be an index such that

$$M_{k^*i}^{-1}q_{k^*} = \max\left\{M_{ki}^{-1}q_k | k \in \overline{K}\right\} \tag{5.21}$$

The variable w_{k^*} in vector $\overline{w}$ is referred to as the "blocking" variable for z_i [94] because the linear function w_{k^*}, among all the linear functions

$$w_k = q_k + M_{ki}z_i, \quad k \in \overline{K} \tag{5.22}$$

is the first which drops to zero when z_i increases starting from zero.

5.2.2 Principal pivoting method

The following iterative procedure is connected with the algorithm due to Dantzig and Cottle [97] [94]; a suitable criterion is introduced to select the variable on which a cycle of pivot transforms (the "major cycle") is open.

All the quantities pertaining to iteration s (or t) are labeled with s (or t); the vectors $\overline{w}^s$ ($\overline{w}^{st}$) and $\overline{z}^s$ ($\overline{z}^{st}$) collect the dependent and independent variables at iteration s (or t, nested in the iteration s).

1. Define a real scalar $\delta > 1$. Set $s = 0$ and assume $[\overline{w}^0, \overline{z}^0] = [\overline{w}, \overline{z}] = [\overline{q}, \overline{0}]$ as the starting solution.
2. If $\overline{q}^s \geq \overline{0}$, terminate; $[\overline{w}^s, \overline{z}^s] = [\overline{q}^s, \overline{0}]$ solve the problem. Otherwise:
3. If the set:

$$\overline{W}^s = \{w_h^s | q_h^s < 0, M_{hh}^s > 0, 1 \leq h \leq n\}$$

   is empty, go to 6. Otherwise:

4. Let $w_{h'}^s \in \overline{W}^s$ the variable (of lowest index) to which corresponds the largest number of negative entries of $\overline{q}^s$ that become greater than or equal to zero by replacing $w_{h'}^s$ with $z_{h'}^s$ in the dependent set of variables.
5.
   a. Set $t = 0, \overline{w}^{s0} = \overline{w}^s, \overline{z}^{s0} = \overline{z}^s, \overline{q}^{s0} = \overline{q}^s, \underline{\underline{M}}^{s0} = \underline{\underline{M}}^s$
   b. If the set

$$\overline{K}^{st} = \{k | q_k^{st} \geq 0, M_{ki}^{st} < 0, \frac{q_{h'}^{st}}{M_{h'h'}^{st}} < \frac{q_k^{st}}{M_{kh'}^{st}}, 1 \leq k \leq n, k \neq h'\}$$

   Is empty, go to 5e, Otherwise:

   c. Select $k^* \in \overline{K}^{st}$ such that $\frac{q_{k^*}^{st}}{M_{k^*i}^{st}} = \max\left\{\frac{q_k^{st}}{M_{ki}^{st}} | k \in \overline{K}^{st}\right\}$;

If the index k^* is not unique, the lowest value is assumed for it. If $M_{k^*k^*}^{st}$ is zero, go to 5f. Otherwise:

   d. $w_{k^*}^{st}$ is made independent and $z_{k^*}^{st}$ dependent with a single pivot in position (k^*, k^*) .Replace t with $t + 1$ and return to 5b.
   e. $w_{h'}^{st}$ is made independent and $z_{h'}^{st}$ dependent by a single pivot in position (h', h') . Go to 8.
   f. A double pivot in position $(h', k^*), (k^*, h')$ is performed. Go to 8.

6. Let $q_i^s < 0$ and $q_k^s \geq 0, 1 \leq k < i$. If $M_{ij}^s \leq 0, i \leq j \leq n$, terminate, (the problem has no solution because the i-th equation is not transformable in any equivalent one with a positive value for the known term). Otherwise:
7.
    a. If there is no $q_k^s > 0$ with $M_{ki}^s < 0, k \neq i, k \leq n$ go to 7b. Otherwise a double pivot in positions (i, k^*), (k^*, i) is performed with k^* such that
    $$\frac{q_{k^*}^s}{M_{k^*i}^s} = \max\left\{\frac{q_k^s}{M_{ki}^s} \;\middle|\; q_{ki}^s > 0, M_{ki}^s < 0, 1 \leq k \leq n\right\}$$
    Go to 8.
    b. Let
    $$q_{min}^s = \min\{q_h^s | q_h^s < 0, M_{hi}^s < 0, 1 \leq h \leq n\}$$
    And $b^s = \delta|q_{min}^s|$. Define k^* such that
    $$\frac{b^s - q_{k^*}^s}{M_{k^*i}^s} = \max\left\{\frac{b^s - q_h^s}{M_{hi}^s} \;\middle|\; q_h^s < 0, M_{hi}^s < 0, 1 \leq h \leq n\right\}$$
    And perform a double pivot in positions $(i, k^*), (k^*, i)$
8. Replace s with $s + 1$. Go to 2.

Steps 5a-5e constitute the major cycle in the case that $\underline{\underline{M}}$ is positive definite; at the end of a major cycle, q_h^s, (at least prop. 3) has turned nonnegative, while none of the nonnegative entries of $\overline{q}^s$ has turned negative. A (finite) sequence of major cycles solves the problem [[94], theorem 11]. Step 4 has been introduced on purpose in this procedure as a (merely local) criterion aimed at maximizing the number of negative entries of $\overline{q}_s$ which at the end of a major cycle become nonnegative.

Steps 5f, 6, 7a, 7b are possibly executed only when $\underline{\underline{M}}$ is positive semidefinite [97] (some diagonal entries in the matrix $\underline{\underline{M^s}}$ may be zero). The double pivot transforms in steps 5f and 7a lead to entries of $\overline{q}^s$ in the positions h' and k^* which are both positive (prop. V). For this reason, priority is given in this procedure to the transform in step 7a over the one in the subsequent step 7b. In step 7a (7b), $w_{k^*}^s$ is still the blocking variable for z_i^s in the sense that it is the first among the dependent variables whose value drops to zero $(-b^s)$ when z_i^s is

increased starting from zero and the other dependent variables are kept at zero. Step 7b is aimed at transforming the i-th equation into an equivalent one with a positive known term.

5.3 LEMKE Algorithm

We first show the outline of Lemke Algorithm [87] as explained in [91]. In general, pivot-based methods try to find a partition of Eq.(5.1):

$$\begin{pmatrix} \overline{w}_{\tilde{\alpha}} \\ \overline{w}_{\tilde{\beta}} \end{pmatrix} = \begin{pmatrix} \underline{\underline{M}}_{\tilde{\alpha}\alpha} & \underline{\underline{M}}_{\tilde{\alpha}\beta} \\ \underline{\underline{M}}_{\tilde{\beta}\alpha} & \underline{\underline{M}}_{\tilde{\beta}\beta} \end{pmatrix} \cdot \begin{pmatrix} \overline{z}_{\alpha} \\ \overline{z}_{\beta} \end{pmatrix} + \begin{pmatrix} \overline{q}_{\tilde{\alpha}} \\ \overline{q}_{\tilde{\beta}} \end{pmatrix} \tag{5.23}$$

such that the pivoted system

$$\begin{pmatrix} \overline{z}_{\alpha} \\ \overline{w}_{\tilde{\beta}} \end{pmatrix} = \underline{\underline{M}}' \cdot \begin{pmatrix} \overline{w}_{\tilde{\alpha}} \\ \overline{z}_{\beta} \end{pmatrix} + \overline{q}' \tag{5.24}$$

satisfies the following conditions:

- $\overline{w}_{\tilde{\alpha}}$ and $\overline{z}_{\alpha}$ contain the same set of indices
- $\overline{q} \geq \overline{0}$.

The vectors $\left(\overline{z}_{\alpha}^{T} \quad \overline{w}_{\tilde{\beta}}^{T}\right)^{T}$ and $\left(\overline{w}_{\tilde{\alpha}}^{T} \quad \overline{z}_{\beta}^{T}\right)^{T}$ are called *basic* and *non-basic* variables, respectively. $\underline{\underline{M}}'$ and $\overline{q}'$ are computed from the original matrix and vector as follows:

$$\underline{\underline{M}}' = \begin{pmatrix} \underline{\underline{M}}_{\tilde{\alpha}\alpha}^{-1} & -\underline{\underline{M}}_{\tilde{\alpha}\alpha}^{-1} \cdot \underline{\underline{M}}_{\tilde{\alpha}\beta} \\ \underline{\underline{M}}_{\tilde{\beta}\alpha} \cdot \underline{\underline{M}}_{\tilde{\alpha}\alpha}^{-1} & \underline{\underline{M}}_{\tilde{\beta}\beta} - \underline{\underline{M}}_{\tilde{\beta}\alpha} \cdot \underline{\underline{M}}_{\tilde{\alpha}\alpha}^{-1} \cdot \underline{\underline{M}}_{\tilde{\alpha}\beta} \end{pmatrix} \tag{5.25}$$

$$\overline{q}' = \begin{pmatrix} \overline{q}'_{\tilde{\alpha}} \\ \overline{q}'_{\tilde{\beta}} \end{pmatrix} \begin{pmatrix} -\underline{\underline{M}}_{\tilde{\alpha}\alpha}^{-1} \cdot \overline{q}_{\tilde{\alpha}} \\ \overline{q}_{\tilde{\beta}} - \underline{\underline{M}}_{\tilde{\beta}\alpha} \cdot \underline{\underline{M}}_{\tilde{\alpha}\alpha}^{-1} \cdot \overline{q}_{\tilde{\alpha}} \end{pmatrix} \tag{5.26}$$

Once such pivot is found, we can easily obtain the solution as:

$$\overline{w}_{\widetilde{\alpha}} = \overline{0} \quad \overline{w}_{\widetilde{\beta}} = \overline{q}'_{\widetilde{\beta}} \quad \overline{z}_{\alpha} = \overline{q}'_{\widetilde{\alpha}} \quad \overline{z}_{\beta} = \overline{0} \tag{5.27}$$

Lemke Algorithm is one of the systematic methods to efficiently find an appropriate pivot. In Lemke Algorithm, we first introduce an auxiliary variable z_0 and modify the original LCP (5.1) as follows:

$$\overline{w} = \underline{\underline{M}} \begin{pmatrix} \overline{z} \\ z_0 \end{pmatrix} + \overline{q} \tag{5.28}$$

Where

$$\underline{\underline{\overline{M}}} = \begin{pmatrix} \underline{\underline{M}} & \overline{c} \end{pmatrix} \tag{5.29}$$

$$\overline{c} = (1 \quad 1 \quad \cdots \quad 1)^T \tag{5.30}$$

The solution of Eq.(5.28) can be found by the following steps:

1. If $\overline{q} \geq \overline{0}$, stop: $\overline{w} = \overline{q}, \overline{z} = \overline{0}$ is the solution. Otherwise, obtain $r = \arg\min\left(\frac{q_i}{c_i}\right)$ and pivot z_0 with w_r. Compute $\underline{\underline{\overline{M}}}'$ and $\overline{q}'$, and set the *driving variable* $y_r = z_r$.
2. Let m' denote the column vector of $\underline{\underline{\overline{M}}}'$ corresponding to y_r. If $m' \geq 0$, stop: there is no solution or this algorithm cannot solve the LCP. Otherwise, obtain $s = \arg\min\left\{-\frac{q_i}{m'_i} | m'_i \leq 0\right\}$ and let y_s denote the s-th element of the basic variables.
3. Pivot y_s with y_r and update $\underline{\underline{\overline{M}}}'$ and $\overline{q}'$. If $y_s = z_0$, stop: $\overline{q}'$ gives the solution. Otherwise set y_r to the complement of y_s and return to Step 2.

After Step 1, $\overline{q}' \geq \overline{0}$ holds with the choice of r and the update rule Eq.(5.26). Similarly, all elements of subsequent $\overline{q}'$ are always equal to or larger than 0 with the choice of s in Step 2. The second condition above is therefore satisfied at every iteration. In Step 3, the first condition is met by setting the driving variable to the complement of the previously pivoted basic variable y_s, and by terminating when z_0 returns to a non-basic variable.

5.4 FBNS Algorithm

We propose a two-step algorithm, called Fischer-Burmeister-Newton-Schur (FBNS) for solving the prob (5.1). It must be noticed that prob. (5.1) can be written as:

$$\overline{w} = \underline{\underline{M}}\overline{z} + \overline{q} \;\rightarrow \overline{G} = \overline{G}(\overline{w}, \overline{z}) = \overline{0} \tag{5.31}$$

In the first step, the constraint $\overline{w}^T\overline{z} = \overline{0}$ is replaced by a system $\overline{F} = \overline{F}(\overline{w}, \overline{z}) = \overline{0}$ of N Fischer-Burmeister (FB) equations. Similar systems have previously been used for replacing complementarity constraints in problems with explicit nonlinear relationship between variables [98]. Here, the FB equations are defined as:

$$F_j = F_j(w_j, z_j) = w_j + z_j - \sqrt{w_j^2 + z_j^2} = 0 \quad j = 1, \dots, N \tag{5.32}$$

The solution of the equations satisfies the complementarity constraint. We note here that the Jacobian matrices $\underline{\underline{J}}_{F,w} = \frac{\partial \overline{F}}{\partial \overline{w}}$ and $\underline{\underline{J}}_{F,z} = \frac{\partial \overline{F}}{\partial \overline{z}}$ are diagonal with the elements given by

$$J_{F,w}^{(j)} = 1 - \frac{w_j}{\sqrt{w_j^2 + z_j^2}}$$

and

$$J_{F,z}^{(j)} = 1 - \frac{z_j}{\sqrt{w_j^2 + z_j^2}}$$

respectively. The replacement of the constraint thus results in an unconstrained system of $2N$ equations consisting of two systems $\overline{F}$ and $\overline{G}$.

The second step is an efficient solution of the unconstrained system. Since the system is continuously differentiable, the Newton method can be applied to find the solution iteratively, that is $\overline{w}^{(k+1)} = \overline{w}^{(k)} + \delta\overline{w}^{(k)}$ and $\overline{z}^{(k+1)} = \overline{z}^{(k)} + \delta\overline{z}^{(k)}$, where $\delta\overline{w}^{(k)}$ and $\delta\overline{z}^{(k)}$ are the solution updates at the k-th iteration. The updates would normally be calculated by solving the following system of linear algebraic equations:

$$\underline{\underline{J}}\begin{bmatrix}\delta\overline{w}^{(k)}\\ \delta\overline{z}^{(k)}\end{bmatrix} = \begin{bmatrix}\underline{\underline{J}}_{F,w} & \underline{\underline{J}}_{F,z}\\ \underline{\underline{J}}_{G,w} & \underline{\underline{J}}_{G,z}\end{bmatrix}\begin{bmatrix}\delta\overline{w}\\ \delta\overline{z}\end{bmatrix} = -\begin{bmatrix}\overline{F}\\ \overline{G}\end{bmatrix} \; at \; (\overline{w} \quad \overline{z}) = (\overline{w}^{(k)} \quad \overline{z}^{(k)}) \tag{5.33}$$

Where $\underline{\underline{J}}_{G,w} = \frac{\partial\overline{G}}{\partial\overline{w}}$ and $\underline{\underline{J}}_{G,z} = \frac{\partial\overline{G}}{\partial\overline{z}}$. However, the difficulties of solving the system in this form are that its size is twice the size of the original system $\overline{G}$ and that $\underline{\underline{J}}$ will typically be worse conditioned than $\underline{\underline{J}}_{G,w}$ and $\underline{\underline{J}}_{G,z}$. These difficulties are addressed as follow.

First, note that $\max\left(J_{F,w}^{(j)}, J_{F,z}^{(j)}\right) \in [1-\sqrt{2}, 2]$ for all w_j and z_j except when both are zero. By swapping the j-th and $(j+N)-$th columns of $\underline{\underline{J}}$ when ,it is thus possible to construct a reordered matrix $\underline{\underline{J}}_r$ whose the top-letf N-by-N submatrix ($\underline{\underline{A}}_F$ in Eq (5.34)) is diagonal, has positive elements and its condition number is at most $4+2\sqrt{2}$. After reordering, the system in Eq. (5.33) can be rewritten as:

$$\underline{\underline{J}}_r\begin{bmatrix}\delta\overline{a}\\ \delta\overline{b}\end{bmatrix} = \begin{bmatrix}\underline{\underline{A}}_F & \underline{\underline{B}}_F\\ \underline{\underline{A}}_G & \underline{\underline{B}}_G\end{bmatrix}\begin{bmatrix}\delta\overline{a}\\ \delta\overline{b}\end{bmatrix} = -\begin{bmatrix}\overline{F}\\ \overline{G}\end{bmatrix} \tag{5.34}$$

Where $\delta\overline{a}$ and $\delta\overline{b}$ denote the reordered solution updates and $\underline{\underline{A}}_F$, $\underline{\underline{B}}_F$, $\underline{\underline{A}}_G$ and $\underline{\underline{B}}_G$ are reordered Jacobian matrices. The above procedure fails when $w_j = z_j = 0$ in which case $J_{F,w}^{(j)}$ and $J_{F,z}^{(j)}$ are undefined. This can occur on the contact boundaries when the ambient and cavitation pressure are set equal. To rectify this, w_j or z_j can be set to any small positive number so that $J_{F,w}^{(j)}$ and $J_{F,z}^{(j)}$ become well-defined with virtually no compromise to the solution accuracy.

Second, we exploit the properties of $\underline{\underline{A}}_F$ and solve Eq.(5.34) using Schur complement of $\underline{\underline{J}}_r$ with respect to $\underline{\underline{A}}_F$. This produces the following two linear system of size N each that need to be solved sequentially:

$$\begin{gathered}\left(\underline{\underline{B}}_G - \underline{\underline{A}}_G \underline{\underline{A}}_F^{-1} \underline{\underline{B}}_F\right) \delta\overline{b} = -\overline{G} + \underline{\underline{A}}_G \underline{\underline{A}}_F^{-1} \overline{F} \\ \underline{\underline{A}}_F \delta\overline{a} = -\overline{F} - \underline{\underline{B}}_F \delta\overline{b}\end{gathered} \tag{5.35}$$

Under reasonable assumptions, the matrix $\underline{\underline{B}}_G - \underline{\underline{A}}_G \underline{\underline{A}}_F^{-1} \underline{\underline{B}}_F$ is nonsingular at the solution which ensures superlinear convergence of the Newton method if the initial value of the complementarity variables are sufficiently close to that solution [99].

A proof showing that the matrix $\underline{\underline{B}}_G - \underline{\underline{A}}_G \underline{\underline{A}}_F^{-1} \underline{\underline{B}}_F$ is well-conditioned has not yet been obtained. In practice, however, we found that its condition number was always lower than that of $\underline{\underline{J}}$.

The complete FBNS algorithm proceed as follows. First, initial values are assigned to the complementarity variables. The system $\overline{F}$ and $\overline{G}$ are then constructed and combined. Next, the combined system are solved iteratively where in each step the updates $\delta\overline{w}^{(k)}$ and $\delta\overline{z}^{(k)}$ are calculated using Schur complement of the reordered system in Eq.(5.35). The iterations are performed until stopping criteria are satisfied, typically until the norm of the updates and the nonlinear residual are below chosen thresholds.

6. Application

6.1 Overview

The algorithm presented in this contribution has been adopted for the elastohydrodynamic analysis of the contact between the conrod small end and the piston pin of a high performance Ducati motorbike engine.

The conrod small-end/piston pin coupling is one of the most critical engine part from a tribological point of view since it operates under severe running conditions [6]. In fact, high loads combined with high temperature and the risk of lubricant starvation may cause surface damages such as scuffing or seizure [7] [8]. In order to preserve the mating surfaces, a bush is usually press-fitted into the conrod small-end to mitigate the contact [100] [101] [102]. Nevertheless, a recent trend is observed of removing the conrod small-end bush with the aim of sparing problems related to the coupling between the bush and the conrod [103] and to save money by avoiding the press-fit process and the subsequent bush machining.

Differently from the conrod big-end/crank pin coupling, that has been widely investigated both theoretically and experimentally in several contributions in the pertinent literature [104] [105] [78] [79], only few contributions can be found focusing on the tribological behaviour of the conrod small-end/piston pin coupling [6], [106] [107] [108] [109] [110]. This lack of modelling is probably related to the difficulties that have to be faced in the definition of the operating conditions of the coupling between the conrod small-end and the piston pin, in terms of both determining the relative speed between the contact surfaces [111] [112] and mimicking the lubricant feeding mechanism [107]. In fact, the way the hydrodynamic lubrication process sustains the external load in the conrod big-end bearing strongly differs from the one encountered in the small-end counterpart [110].

In the conrod big-end, the hydrodynamic load capacity is mainly generated by the high relative rotational speed between the conrod and the crankshaft. On the contrary, the relative rotational speed between the conrod small-end and the piston pin is low and only an oscillation between the mating surfaces occurs. Moreover, the piston pin generally floats with respect to the two other components in contact with it, namely the conrod and the piston [6]. For this reason, it is not possible to exactly define the relative speed between the mating surfaces of the small-end and of the piston pin. Therefore, the dominant effect in the lubrication of the small-end is the film squeeze caused by the alternating combustion/inertial loads acting on the coupling, while sliding hydrodynamic effects are usually negligible [80]. Figure 6.1 depicts the component under investigation.

Figure 6.1. Conrod and piston pin of the engine under investigation.

6.2 Application

In the application of small-end bearing analysis, the *squeeze* effect, related to the time dependent term of the Reynolds equation Eq. (2.1), constitutes the major contribution to the load support mechanism [80]. An uncertainty instead exists on the contribution of the sliding speed between the small-end and the piston pin. In fact, the piston pin has a rigid body motion around its axis and therefore it is not possible to univocally determine the relative velocity between the mating surfaces. Both the cases with a zero and maximum sliding velocity have been considered with the maximum velocity equal:

$$v_{pist} = \frac{\partial \varphi}{\partial \theta}\ \omega\ r_{pin} = \frac{r_{pin}\omega\ cos(\theta)\ \lambda}{\sqrt{1 - sin(\theta)^2 \lambda^2}} \tag{6.1}$$

where φ is the conrod tilt angle, θ is the cranck angle, r_{pin} is the outer radius of the pin and λ is the ratio between the crank radius and the conrod length. Differences in the results of the two cases are negligible so in the present contribution a null velocity is considered.

6.3 Governing equation and Numerical Algorithm

The newton method of Eqn.(4.23), together with the selected direct contact algorithm, allows the hydrodynamic pressure p, the void ratio r, the asperity contact pressure p_a and the film thickness h to be evaluated for a certain position of the piston pin center. For each step of simulation, the correct piston pin center position can be obtained considering that the single components of the external load, $Fx(t)$ and $Fy(t)$, have to be balanced by the total pressure distribution integrated over the simulation domain, see Figure 6.2:

$$\begin{aligned} \int_{\Omega} p_{tot}(\alpha)\cos(\alpha)\, d\Omega + Fx(t) = 0 \\ \int_{\Omega} p_{tot}(\alpha)\sin(\alpha)\, d\Omega + Fy(t) = 0 \end{aligned} \tag{6.2}$$

Also in this case, a Newton method has been employed in order to iteratively find the correct piston pin center position for each simulation step. In particular, the Jacobian matrix has been numerically evaluated by computing the total pressure distribution for a small displacement of the pin center position in each direction.
Figure 6.3 depicts he flow chart of the algorithm employed.

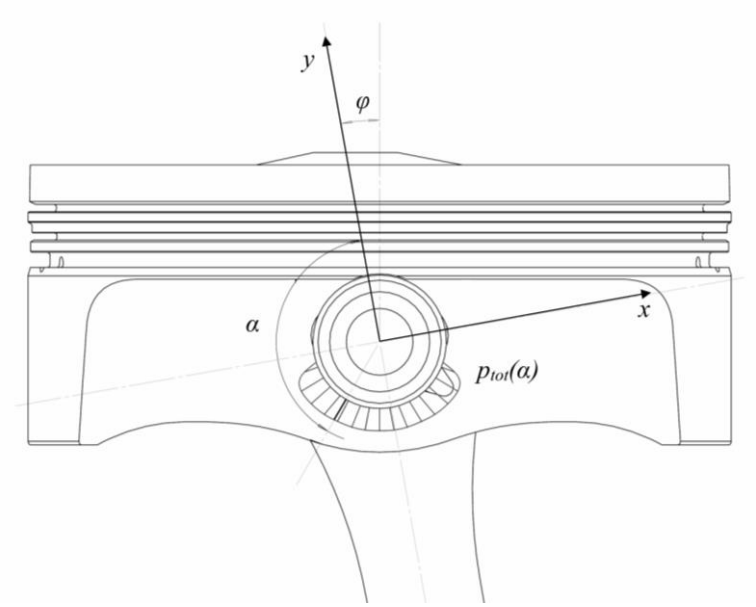

Figure 6.2 Schematic of the coordinate system

6.4 Finite Element compliance matrix

In order to evaluate the compliance matrix of the components, Finite Element models of the conrod small end and of the piston/piston pin assembly have been prepared. A proper symmetry plane has been considered. Figure 6.4 shows the discretization adopted for all the components. In order to remove the rigid body motions, the cross section of the conrod shank has been clamped at a distance from the contact area twice the pin outer diameter [113]. At the same way, the piston has been clamped in correspondence of the piston top area.

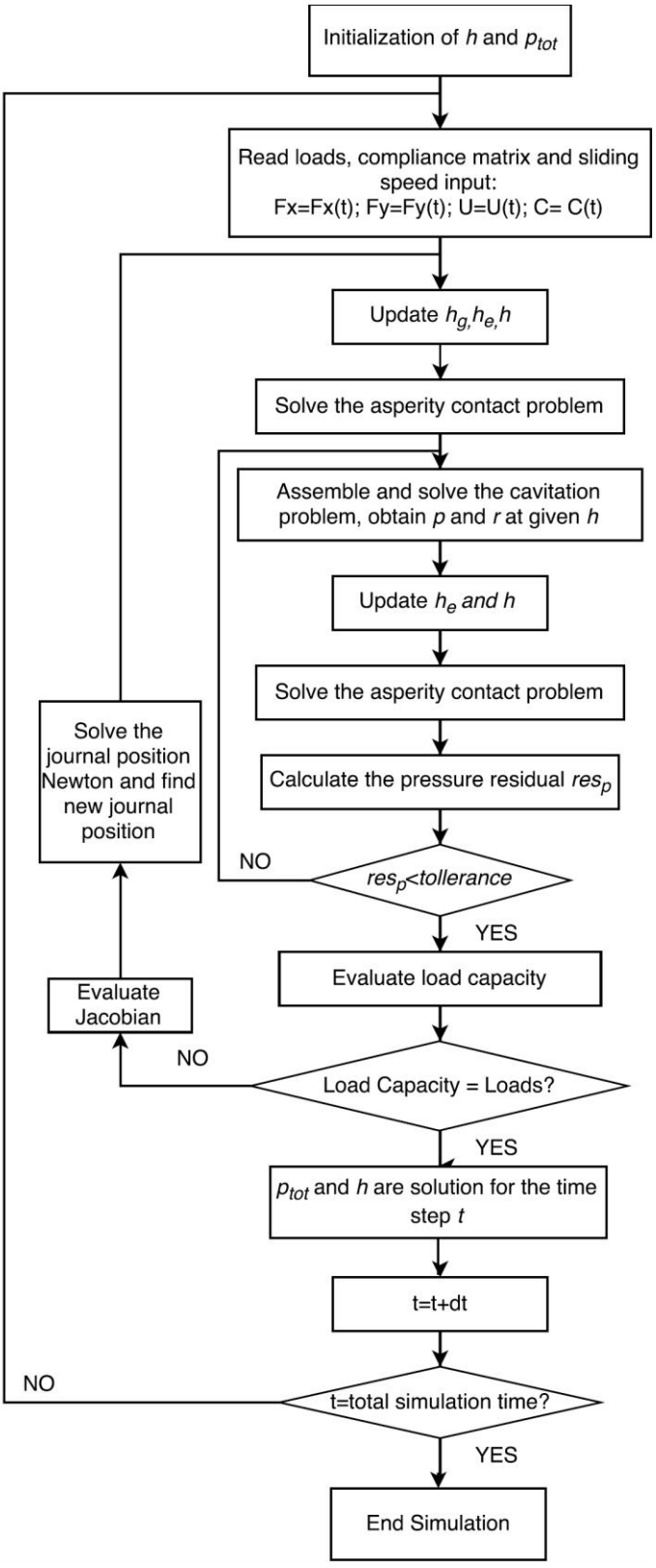

Figure 6.3. Flow chart of EHD algorithm

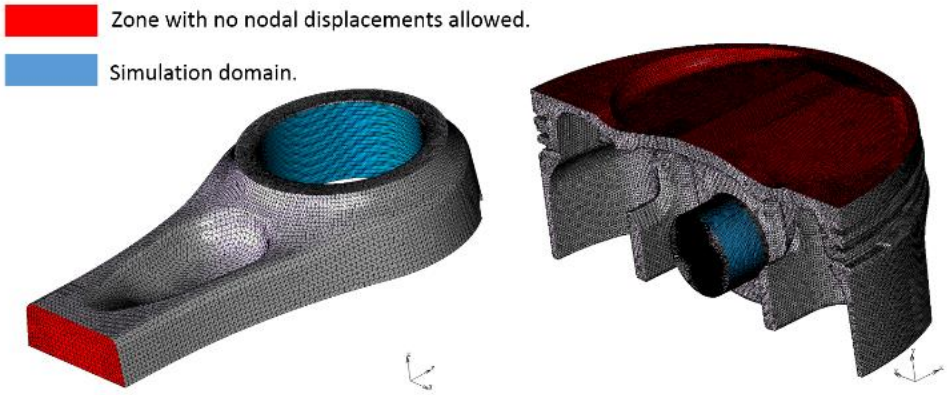

Figure 6.4. Finite Element discretization

Table 6.1 collects the elastic properties of the material adopted.

Component	**Young modulus *E* (MPa)**	**Poisson ratio υ**
Conrod	210.000	0.3
Piston pin	210.000	0.3
Piston	75.000	0.33

Table 6.1. Material properties of assembly component

The two compliance matrices have been then modified by a proper Python routine in order to obtain a relation between a generic radial pressure applied to any of the nodes in the contact area and radial displacements of all nodes. The total compliance of the contact surfaces has been evaluated composing the two compliance matrices. Finally, a proper downsampling technique has been employed in order to match the compliance matrix dimensions with the fluid mesh dimensions. In particular, 100 elements in the circumferential direction and 12 elements in the axial direction have been employed.

Figure 6.5 shows the radial displacements evaluated at the contact area when a uniform unitary pressure is applied.

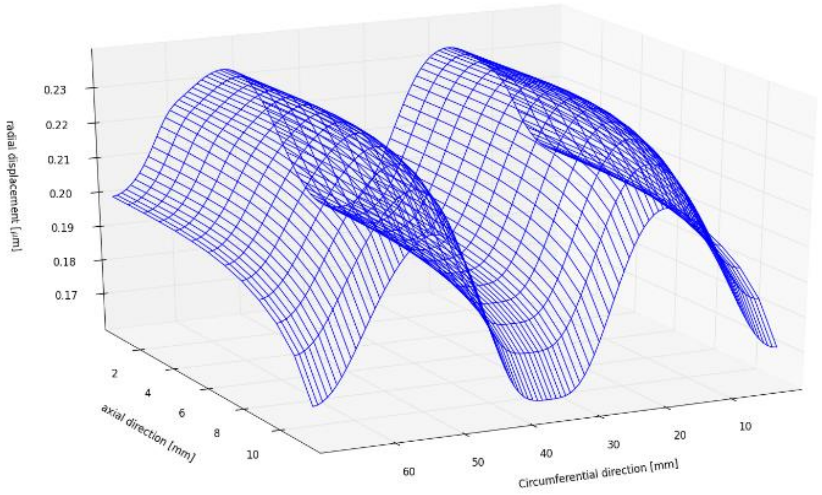

Figure 6.5. Radial displacement under the action of unitary radial pressure.

6.5 Oil model and boundary condition

Table 6.2 collects the main lubricant properties adopted to set up the model. In the preliminary investigation presented in this contribution, non-Newtonian and piezoviscous fluid behaviour has been neglected in order to simplify the simulations. Such behaviours could be easily introduced in future simulations with simple modifications [9].

Temperature (°C)	**Density ρ (kg/m^3)**	**Dynamic viscosity μ (cP)**
140	777.0	6.3

Table 6.2. Lubricant properties as a function of temperature

The correct amount of lubricant inside the contact area is guaranteed by two supply holes, Figure 6.6.

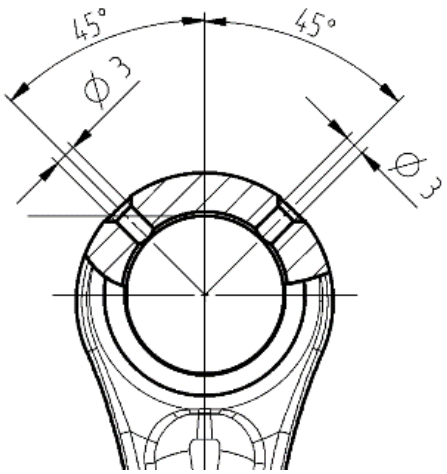

Figure 6.6. Oil supply shemes

A constant pressure condition has been applied to the nodes in correspondence of the two supply holes, Figure 6.7.

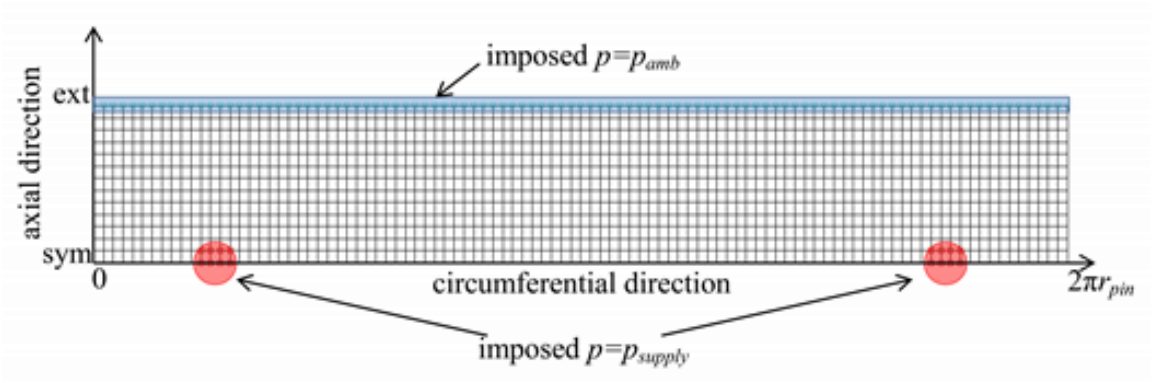

Figure 6.7. Schematic of boundary condition

6.6 External Load

Both inertial forces and combustion forces have been considered as a function of the crank angle. According to the adopted coordinate system, Figure 6.2, both inertial forces and combustion forces contribute to the load component directed along the *y* axis, while only the inertial forces due to the rotational motion of the conrod contribute to the load component directed along the *x* axis. Figure 6.8 shows the loads applied to the system. Crank angle equal zero corresponds to top dead center position during combustion.

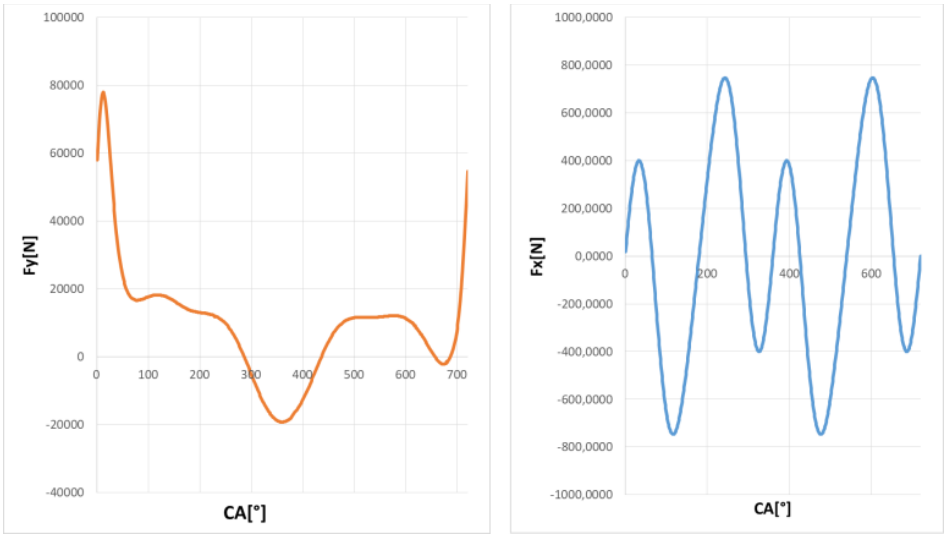

Figure 6.8. External forces.

6.7 Simulation Data

Table 6.3 collects the main input parameters adopted for the simulations

Piston-pin external radius	r_{pin}	11.0	mm
Piston-pin internal radius	r_{i_pin}	5.5	mm
Small-end axial length	t	11.15	mm
Radial clearance	c_r	0.02175	mm
Small End Roughness	R_{a1}	0.7	µm
Piston Pin Roughness	R_{a2}	0.07	µm
Total Roughness	R_a	0.77	µm
Crankcase pressure	p_{amb}	0.05	MPa
Cavitation pressure	p_c	0.0	MPa
Supply oil pressure	p_{sup}	0.05	MPa
Rotational speed	rpm	8500	rpm

Table 6.3.Simulation Data

6.8 Asperity contact model calibration

The asperity contact models presented in the previous section need different parameters to be set up. Both the models consider non-linear sprigs linking two opposite nodes of the facing surfaces, with a compliance that varies as a function of the film thickness, h. These fictitious springs work in series with the compliance matrices of the assembly components. Referring the Greenwood/Tripp algorithm (referred as G/T), a continuous non-linear stiffness curve is considered following Eq. (4.37). Moving to the complementarity formulation of the direct contact (referred as LCP), a discontinuous behaviour of these fictitious springs is obtained. In facts, a null stiffness is considered for $h > h_0$, while an infinite stiffness results for $h = h_0$. In order to refer the two models to the same asperity profile, the different parameters in Eq. (4.37) have to be chosen in a way that a consistent direct pressure support to the load carrying capacity is obtained when the film thickness reaches a value similar to the critical film thickness of the complementarity model, h_0. In particular, in this first simulation, h_0 has been chosen equal to the total roughness R_a of the mating surfaces. For the Greenwood/Tripp model, the mean summit height $\delta_{s1,2}$ of each surface and the height standard deviation of the asperity summits of each surface, $\sigma_{s1,2}$, have been chosen equal half of the roughness $R_{a\,1,2}$ of each contacting surface. The elastic factor K has been chose equal to a standard value $K = 0.003$. Lower values of the elastic factor K usually lead to convergence problems since an asperity contact pressure p_a not high enough to prevent penetration between the contacting bodies could be evaluated. On the other side, too high values of the elastic factor K could bring to high values of the asperity contact pressure p_a with high values oh the film thickness, h. Table 6.4 and Table 6.5 collect the main set up parameters for the two asperity contact models.

Complementarity Formulation			
Description	**Name**	**Formula**	**Value**
Oil Film height at	h_0	$R_{a1} + R_{a2}$	0.77

Table 6.4. Complementarity asperity contact model input.

Greenwood/Tripp			
Description	**Name**	**Formula**	**Value**
S.E. Mean summit height	δ_{s1}	$R_{a1}/2$	0.35 µm
S.E. Root-Mean-Square of summit height	σ_{s1}	$R_{a1}/2$	0.35 µm
Pin Mean summit height	δ_{s2}	$R_{a2}/2$	0.035 µm
Pin Root-Mean-Square of summit height	σ_{s2}	$R_{a2}/2$	0.035 µm
Composite Mean summit height	δ_s	$\delta_{s1+}\,\delta_{s2}$	0.385 µm
Composite Root-Mean-Square of summit height	σ_s	$\sqrt{\sigma_{s1}^2+\sigma_{s2}^2}$	0.352 µm
Elastic Factor	K		0.003

Table 6.5. Greenwood/Tripp asperity contact model input

Figure 6.9 shows the asperity contact pressure-clearance height relationship for the two asperity contact models.

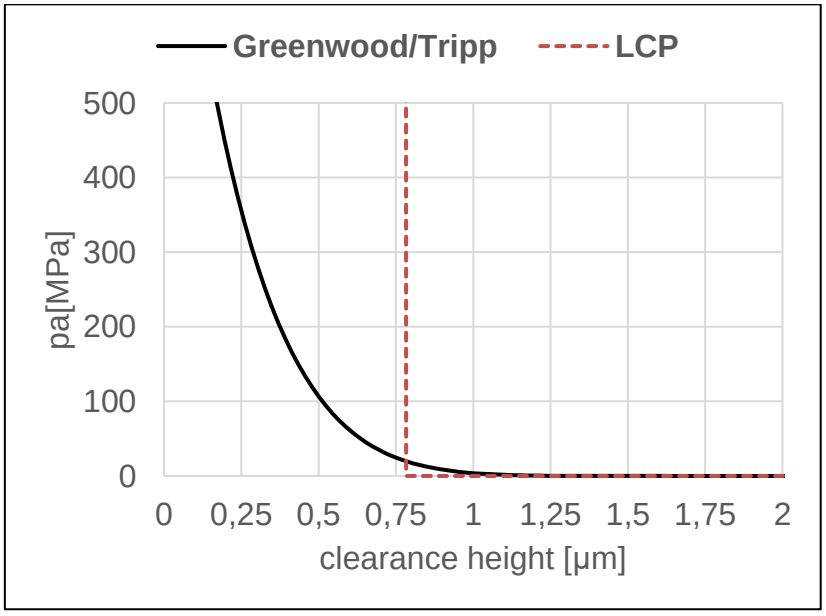

Figure 6.9 Comparison between asperity contact pressure

7. Results

Adopting the pivoting or the LEMKE method in order to solve the cavitation problem, very high simulation time are registered (∼4 day). A strong reduction of simulation time was achieved switching to FBNS solving method (∼20 hr). The simulation time strongly depends on the presence of asperity contact, adopting both the presented asperity contact models (some advantages are registered for the Greenwood/Tripp model). For this reason, the computational cost of simulations of high performance engines, as the one object of this work, are very high.

The influence of the particular asperity contact model adopted for the analysis of the lubricated contact between the conrod small-end and the piston pin is discussed in the following in terms of orbit diagrams of the pin center, minimum film thickness distributions, hydrodynamic pressure, asperity contact pressure and total pressure distributions.

7.1 Piston pin orbit diagram

Figure 7.1 and Figure 1.2 show the pin orbit diagrams for the complementarity asperity contact algorithm and the Greenwood/Tripp algorithm (referred as G/T), respectively. A higher pin displacement is registered along *y* direction due to the higher values of the external loads (inertial and combustion) in this direction. Considering the input parameters adopted, no differences can be appreciated between the two diagrams of Figure 7.1 and Figure 1.2.

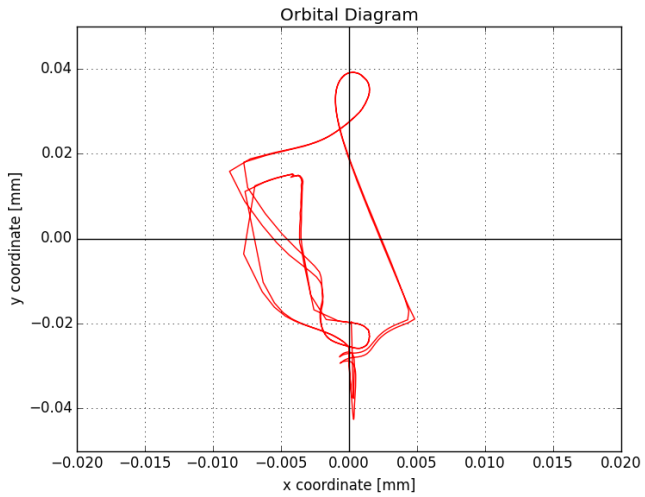

Figure 7.1. Orbit diagram obtained using LCP asperity contact algorithm.

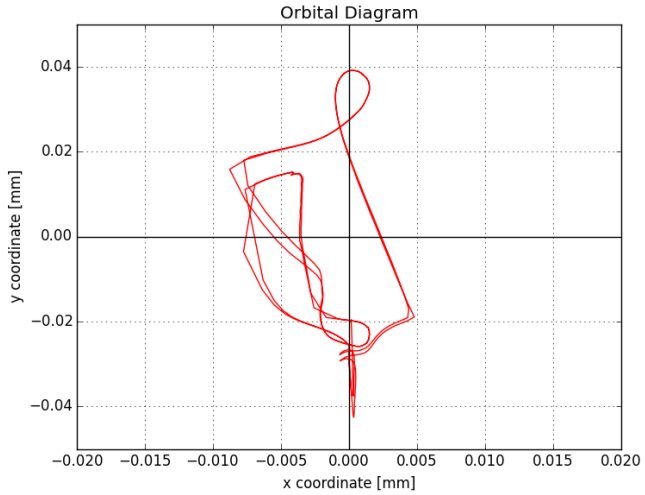

Figure 7.2. Orbit diagram obtained using G/T asperity contact algorithm

7.2 Minimum Oil Film Thickness (MOFT)

Figure 7.3 compares the minimum oil film thickness (MOFT) along the whole engine cycle for the two asperity contact models adopted. The complementarity algorithm prevents a minimum film thickness lower than h_0 to be obtained, while lower values are registered adopting the Greenwood/Tripp method.

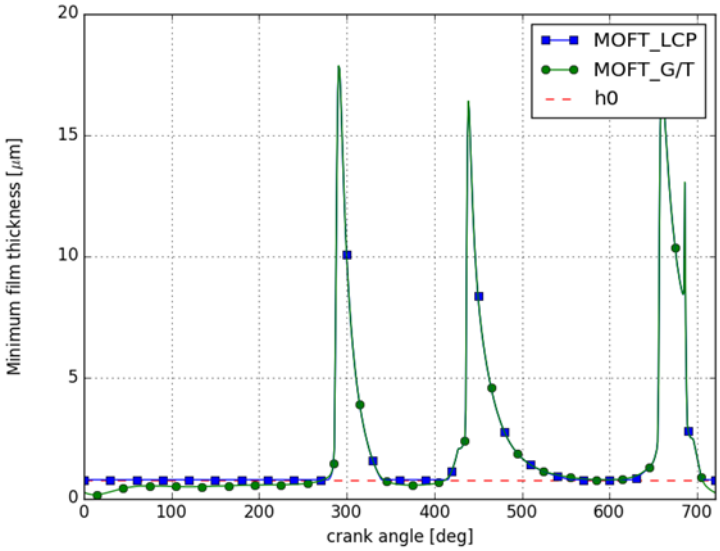

Figure 7.3. Comparison between minimum oil film thickness calculated with the two asperity contact algorithms

To better investigate the differences between the two algorithms, three different portions of the simulation domain have been analysed: the area in the vicinity of the symmetry plane *(sym)*, the area at the external boundary *(ext)* and a zone in the middle of the simulation domain *(mid)*, Figure 7.4.

Figure 7.5 shows a comparison of the minimum oil film thickness for the three portions analysed considering the two asperity contact algorithms adopted. The lower values are obtained at the external boundary while in the vicinity of the symmetry plane the minimum film thickness is always higher than the critical value h_0.

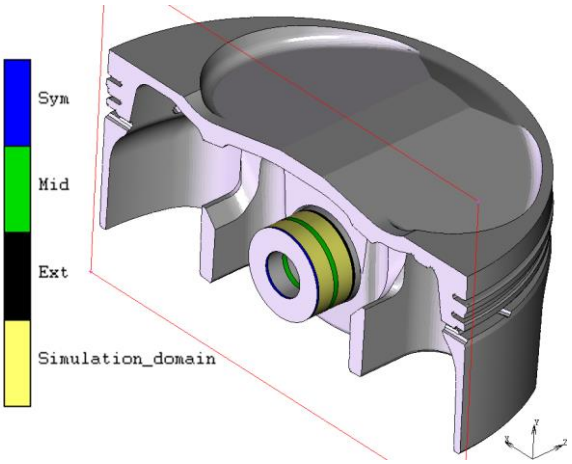

Figure 7.4. Analysed piston pin areas.

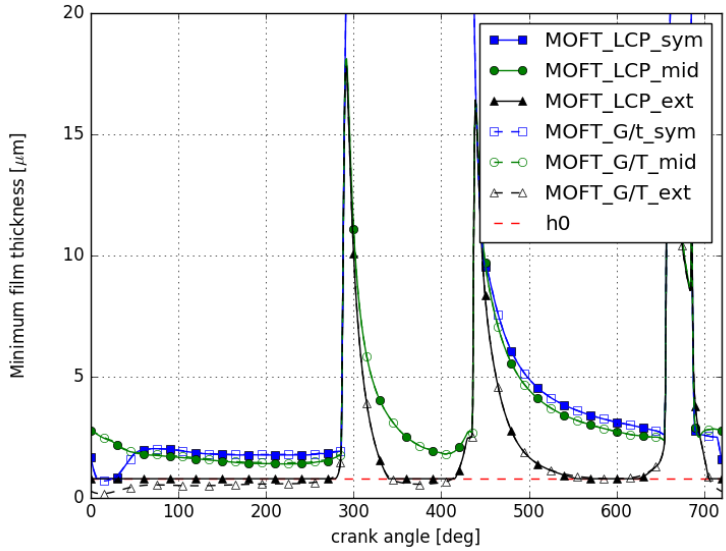

Figure 7.5. MOFT in different section for different asperity contact algorithms.

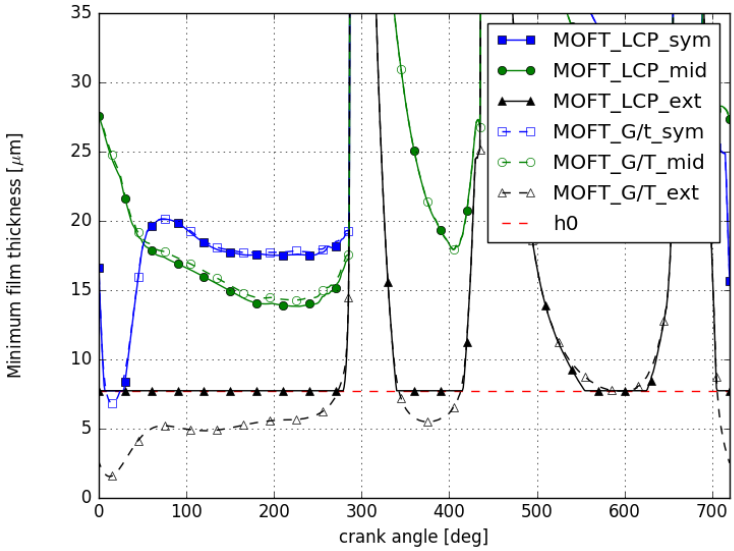

Figure 7.6. MOFT in different section for different asperity contact algorithms - detail.

The detail of Figure 7.6 highlights the portions in the vicinity of the external boundary where the Greenwood/Tripp algorithm registers values of the minimum film thickness lower than h_0.

7.3 Pressure Distributions

Figure 7.7 compares the hydrodynamic pressure distributions averaged over the whole engine cycle. Considering the input parameters adopted, a good agreement is observed between the two distributions. In details, the Greenwood/Tripp algorithm registers values of the hydrodynamic pressure slightly lower than the ones obtained adopting the complementarity formulation of the asperity contact problem.

Figure 7.8 compares the asperity contact pressure distributions averaged over the whole engine cycle. The area subjected to the highest values of direct contact pressure is the external boundary of the simulation domain (*ext* in Figure 7.4) in the vicinity of the conrod shank, where minima film thickness values are also detected. The complementarity formulation of the asperity contact problem registers a more concentrated distribution of the contact pressure, resulting in a higher maximum of the mean asperity pressure value (80 MPa for LCP, 60 MPa for G/T). This result can be explained considering the different relationship between the film thickness and the asperity contact pressure adopted for the two models, Figure 6.9. Figure 7.9 compares the total pressure distributions averaged over the whole engine cycle.

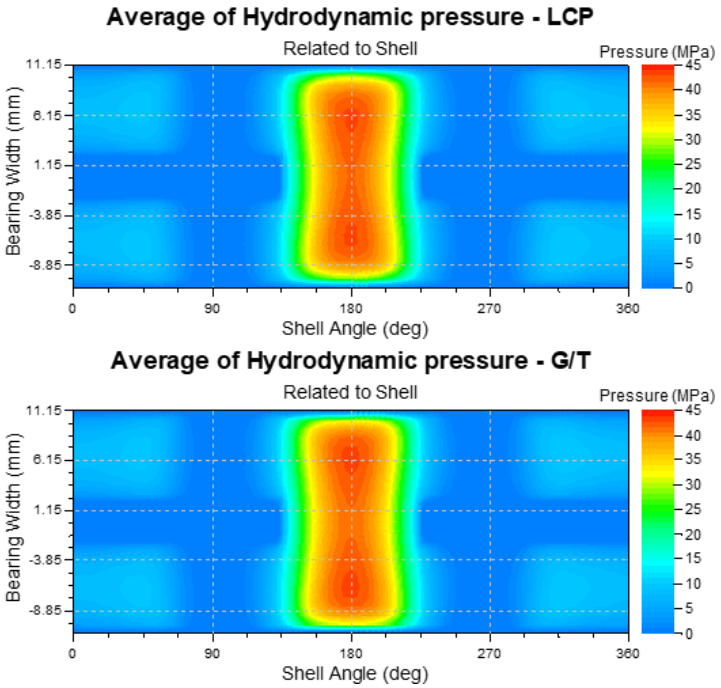

Figure 7.7. Comparison between mean hydrodynamic pressure distributions obtained with the two different asperity contact algorithms.

These results confirm that similar forecasts can be obtained adopting the two different asperity contact models if proper parameters are adopted. In this sense, the complementarity approach is easier to be tuned since only one parameter has to be managed (h_0). Moreover the complementarity nature of the problem avoid convergence issues to be managed.

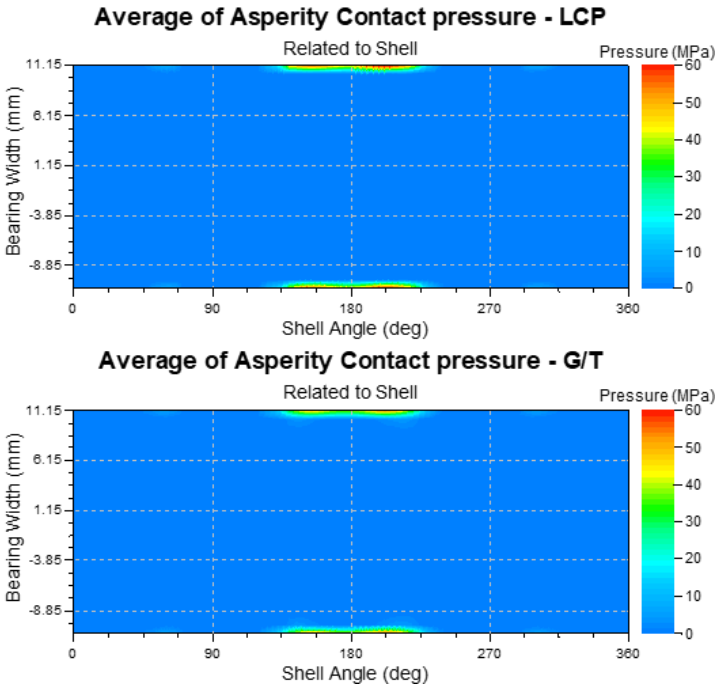

Figure 7.8. Comparison between mean asperity contact pressure distributions obtained with the two different asperity contact algorithms.

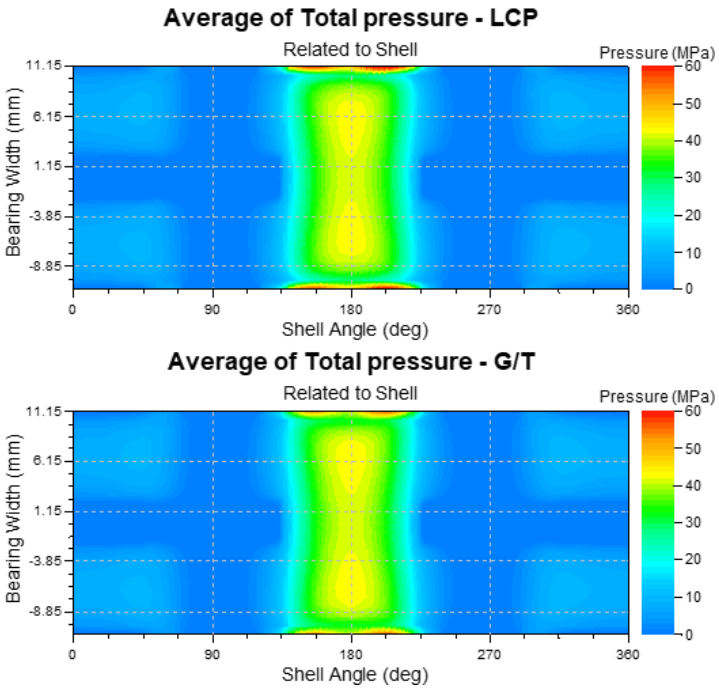

Figure 7.9. Comparison between total pressure distributions obtained with the two different asperity contact algorithms.

7.4 Influence of G/T roughness parameter

Considering that the input parameters to be employed to set up the Greenwood/Tripp model are usually difficult to be identified, a sensitivity analysis has been performed in order to quantify their influence on the results. In particular, two other sets of input parameters compatible with the same roughness R_a have been considered. Two other asperity contact pressure-clearance curves are therefore obtained one "*softer*" and one "*stiffer*" with respect to the original curve of Figure 6.9 (referred as original), see Figure 7.10. Table 7.1 and Table 7.2 collect the new sets of parameters.

Description	Name	Formula	Value
S.E. Mean summit height	δ_{s1}	R_{a1}	0.7 μm
S.E. Root-Mean-Square of summit height	σ_{s1}	$\delta s/\sqrt{2}$	0.54 μm
Pin Mean summit height	δ_{s2}	R_{a2}	0.07 μm
Pin Root-Mean-Square of summit height	σ_{s2}	$\delta s/\sqrt{2}$	0.54 μm
Composite Mean summit height	δ_s	$\delta_{s1+}\,\delta_{s2}$	0.77 μm
Composite Root-Mean-Square of summit height	σ_s	$\sqrt{\sigma_{s1}^2+\sigma_{s2}^2}$	0.77 μm
Elastic Factor	K		0.003

Table 7.1. Input parameter for stiffer G/T asperity contact pressure – clearance relationship.

Description	Name	Formula	Value
S.E. Mean summit height	δ_{s1}	$R_{a1}/4$	0.175 μm
S.E. Root-Mean-Square of summit height	σ_{s1}	$R_{a1}/4$	0.175 μm
Pin Mean summit height	δ_{s2}	$R_{a2}/4$	0.0175 μm
Pin Root-Mean-Square of summit height	σ_{s2}	$R_{a2}/4$	0.0175 μm
Composite Mean summit height	δ_s	$\delta_{s1+}\,\delta_{s2}$	0.1925 μm
Composite Root-Mean-Square of summit height	σ_s	$\sqrt{\sigma_{s1}^2+\sigma_{s2}^2}$	0.1759 μm
Elastic Factor	K		0.0018

Table 7.2. Input parameter for softer G/T asperity contact pressure – clearance relationship.

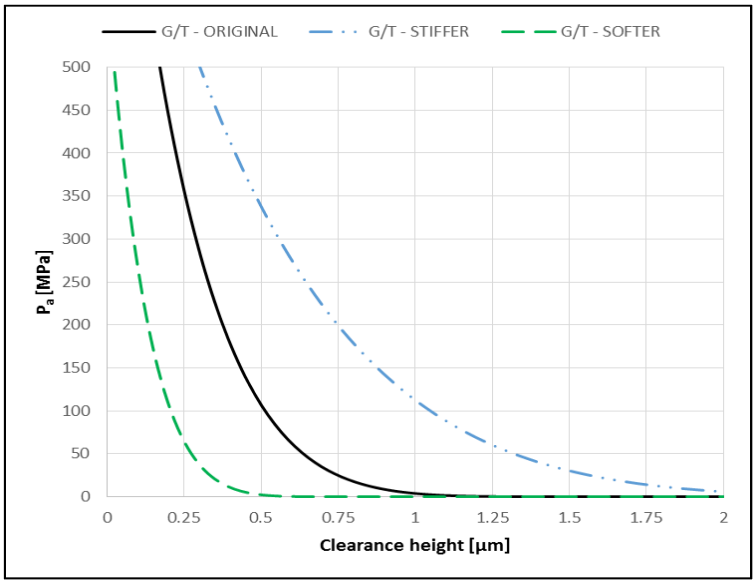

Figure 7.10. New G/T asperity contact pressure-clearance curve

Figure 7.11 compares the minimum oil film thickness (MOFT) along the whole engine cycle for the Greenwood/Tripp algorithm set with the new parameters of Table 7.1 and Table 7.2 and the original parameters of Table 6.5. A higher film thickness is detected when the parameters of Table 7.1 are adopted. In fact, the higher stiffness of the fictitious non-linear springs introduced by the asperity contact model guarantees higher values of the asperity contact pressure p_a, which help to support the external load with higher values of the film thickness. On the contrary, a lower film thickness is detected when the parameters of Table 7.2 are considered since the lower stiffness of the fictitious non-linear springs of the model gives a lower contribution to the load support of the areas where direct contact occurs. Figure 7.12 and Figure 7.13 clarify that the most important differences between the original set of parameters and the softer and stiffer modifications, are confined to the external portion of the contact (see Figure 7.4), where the lower values of film thickness are detected and direct contact occurs.

Figure 7.14 *a)* and *b)* compare, for the different input parameters considered, the averaged hydrodynamic pressure distribution and the averaged asperity contact pressure distribution, respectively. When the parameters of Table 7.1 are adopted, a wider area with high values of asperity contact pressure is detected, thus reducing the contribution to the load support given by the hydrodynamic pressure. At the same time, when the parameters of Table 7.2 are

considered, a higher averaged hydrodynamic pressure is detected because of the lower contribution to the load support given by the asperity contact pressure.

Such results prove that the solution of the problem is strictly dependant on the parameters governing the Greenwood/Tripp algorithm employed to mimic the asperity contact problem.

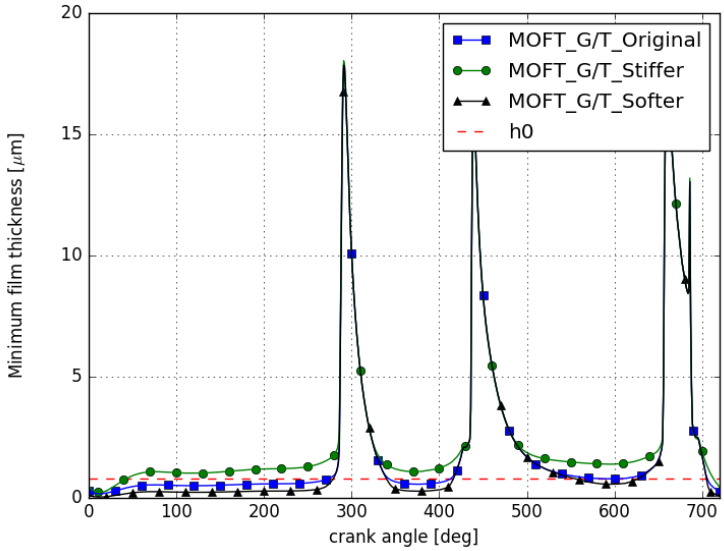

Figure 7.11. Comparison between minimum oil film thickness calculated with different G/T parameters.

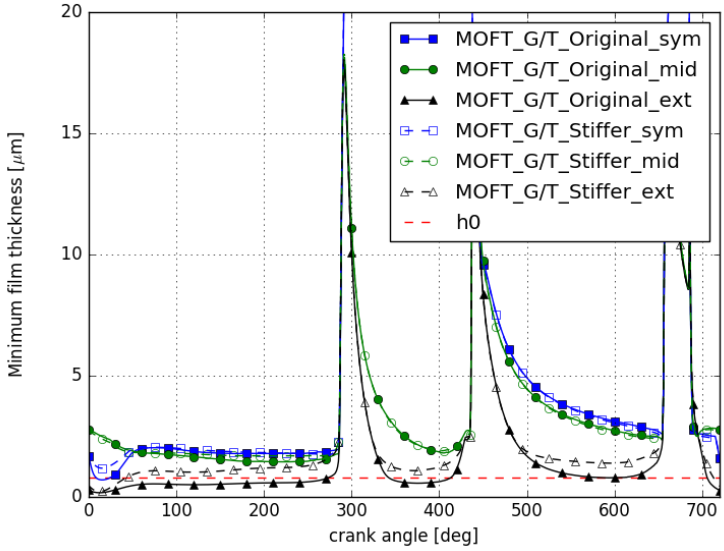

Figure 7.12. MOFT in different sections for G/T set with *original* parameters and G/T set with *stiffer* parameters.

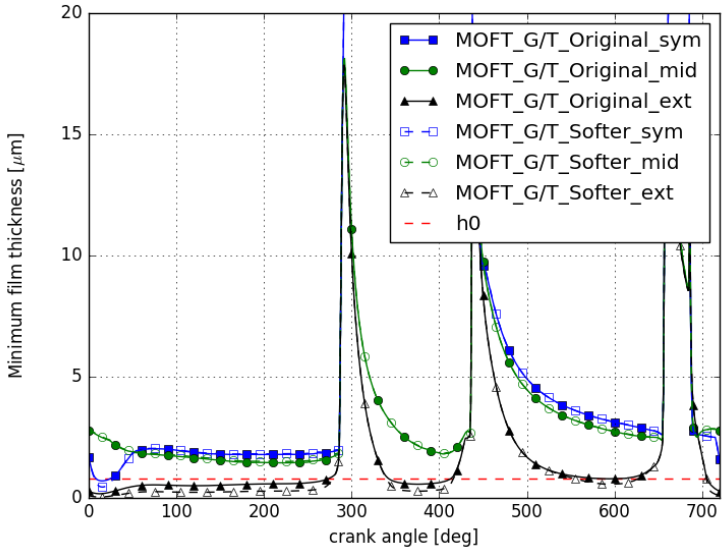

Figure 7.13. MOFT in different sections for G/T set with *original* parameters and G/T set with *softer* parameters.

a) *b)*

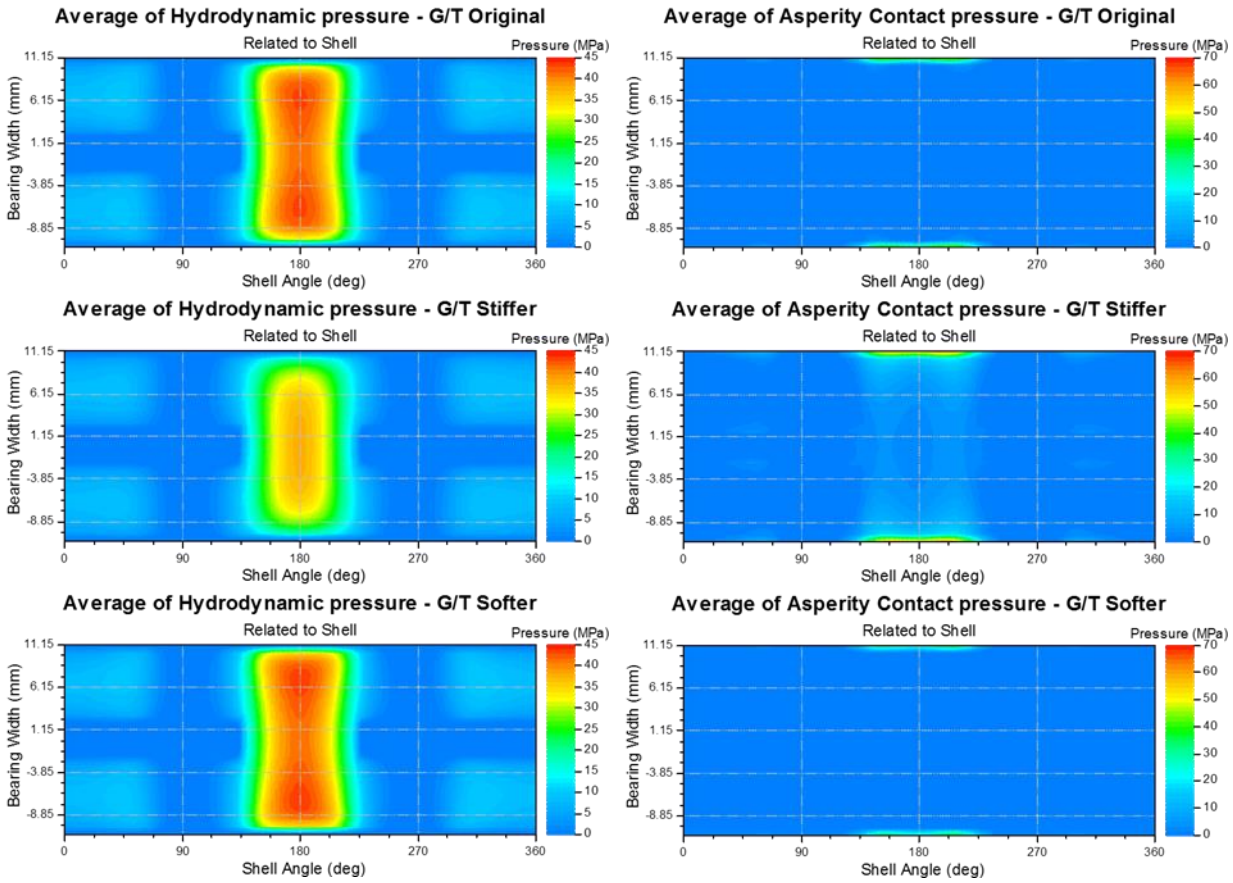

Figure 7.14. Comparison between mean pressure distributions calculated with different G/T parameters.

8. *Excite Power Unit model*

In order to validate the model, a multibody simulation has been performed using the commercial software *AVL Excite Power Unit*. Figure 8.1 shows a schematic of the *Excite* multibody model. To correctly consider the inertial and stiffness information of the connecting rod (element *Conrod1* of the *Excite* model) and of the piston-piston pin assembly (element *P-Pin1* of the *Excite* model), the Craig-Bampton [114] reduced stiffness and mass matrices have been extracted from Finite Element models. In particular, the first 90 modes of the structures have been taken into account during the dynamic reduction and appropriate master nodes have been identified in order to connect each other the different components of the assembly.

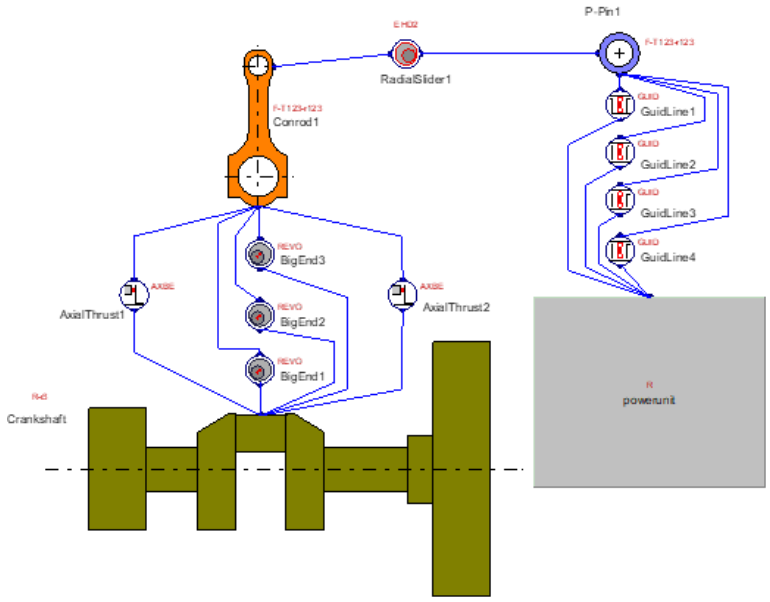

Figure 8.1. *AVL Excite Power Unit* model

In particular, the following degrees of freedom of the master nodes have been selected to correctly guide the multibody model elements:

- the vertical and horizontal displacements of nodes lying in the fluid domain at the interface between the conrod small-end and piston pin (*EHD2* joint);
- the axial displacement (with respect to the crankshaft) of six nodes for each conrod big-end shoulder, to provide axial guidance to the conrod (*AxialThrust* joints);
- all the degrees of freedom of the three reference nodes of the Rbe2 rigid elements created in the big-end bearing zone, used to guide the rotational motion of the conrod (*Revo* joints);
- all the degrees of freedom of the two reference nodes of the Rbe2 rigid elements created on each side of the piston skirt (*GuidLine* joints);
- all the degrees of freedom of the reference node of an Rbe2 rigid element tying the piston top zone (where the combustion load are also applied).

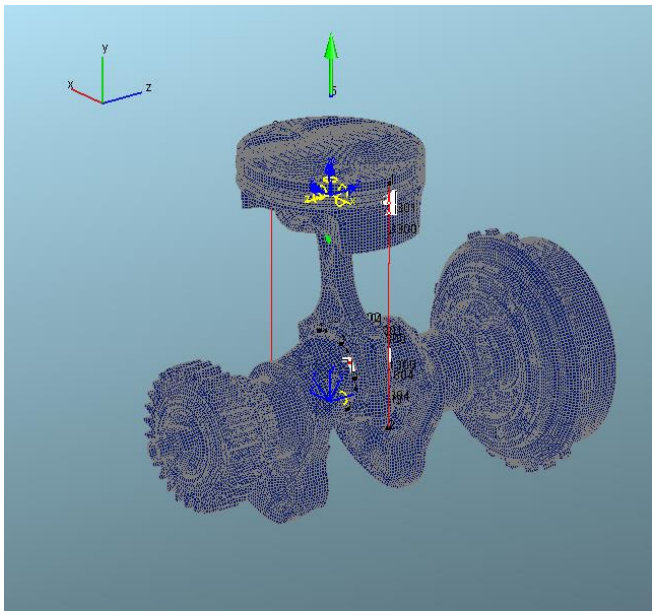

Figure 8.2. 3D View of AVL EXCITE POWER UNIT model.

The crankshaft and the crankcase have been considered as rigid elements. Suitable joints have been then created in order to correctly mimic the motion of the assembly. In particular:

- two *AxialThrust* joints have been used to mimic the axial contact between the conrod big-end and the crankshaft, thus guaranteeing the axial guidance of the conrod assembly;

- four *GuidLine* joints have been used to mimic the contact between the piston skirt and the liner; proper stiffness and damping parameters have been adopted in such a way that the reaction at complete gap recovery can support the maximum lateral force, amplified by a safety factor of 2;
- three *Revo* joints have been used to simulate the conrod big-end/crank pin contact with a stiffness capable to support the maximum combustion force, amplified by a safety factor of 2;
- a *EHD2* joint (*RadialSlider1* in Figure 8.1) has been introduced to mimic the contact interface between the conrod small-end and the piston pin. This joint allows an elastohydrodynamic analysis of the coupling to be performed. In particular, the $p-\theta$ algorithm [20], based on the mass conserving JFO conditions [14] [115] , is adopted to describe the cavitation phenomenon and the surface deflection is taken into account thanks to the Craig-Bampton dynamic reduction of the components in contact. Moreover, the asperity contact problem is modelled considering the Greenwood/Tripp surface contact model, set with the same parameters of Table 6.5. The same fluid mesh dimensions of the previous calculations have been adopted: 100 elements in the circumferential direction and 24 elements in the axial direction (no symmetry planes have been adopted in this case).

8.1 EXCITE Results

Adopting the same FEM discretization of the components involved in the simulations, the computational time of the *EXCITE* simulation and of the method proposed in this thesis are almost the same.

Figure 8.3 compares the results in terms of MOFT obtained by the algorithm developed by the authors with the ones obtained by the *EXCITE* simulation. A very good agreement is obtained thus validating the proposed algorithm.

Figure 8.4 shows the averaged hydrodynamic pressure and the averaged asperity contact pressure distributions. Again a good agreement is obtained with the results of Figure 7.7 and Figure 7.8.

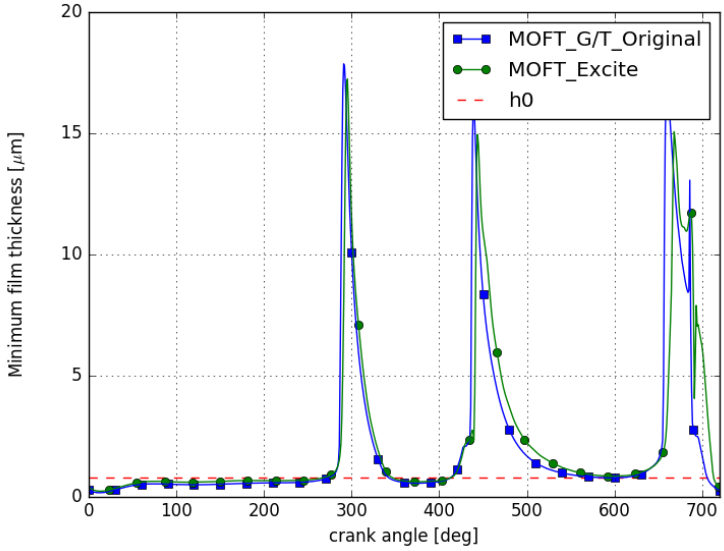

Figure 8.3. Comparison between the proposed algorithm and the EXCITE MOFT results.

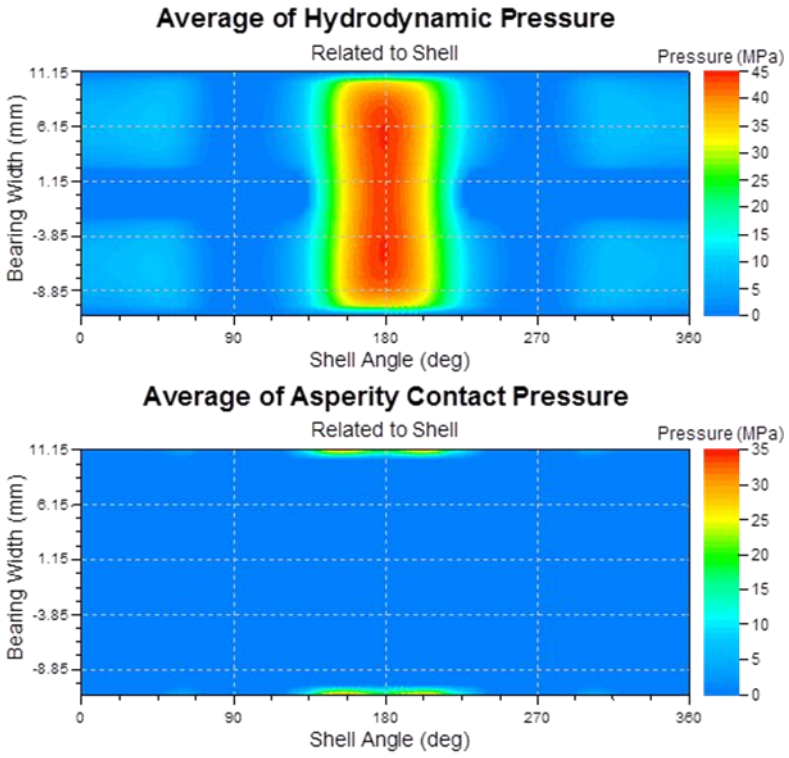

Figure 8.4. Averaged pressure distributions obtained using EXCITE.

8.2 Influence of EXCITE model setting

In order to assess the stability of the results obtained by the EXCITE model, a sensitivity analysis has been performed of the main parameters governing the model. In particular two different models have been prepared where the number of modes considered in the Graig-Bampton dynamic reduction has been doubled (moving from 90 modes to 180 modes) and the number of elements of the fluid mesh of the EHD2 joint at the interface between the small-end and the piston pin have been doubled (moving from 100 to 200 elements in the circumferential direction and from 24 to 48 elements in the axial direction).

Figure 8.5 compares the MOFT obtained considering the modified parameters of the EXCITE model with the one obtained considering the original set up. A perfect matching is registered of the different curves thus proving the stability of the EXCITE model.

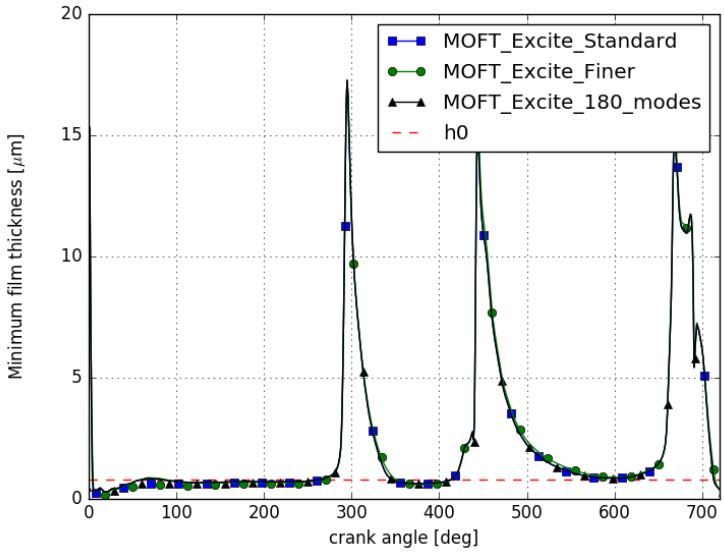

Figure 8.5. Comparison in terms of MOFT of the different EXCITE model set up.

9. *Experimental measurement of roughness data and evaluation of Greenwood/Tripp parameters*

9.1 Overview

In section 7.4 a sensitivity analysis is presented showing that non-negligible differences in the pressure fields can be obtained from simulations set with different input parameters consistent with the same R_a roughness data. As a consequence, a precise measurement of Greenwood/Tripp input data seems to be mandatory in order to obtain fully predictive results. Standard values, based on some limited experiences, are typically used in order to set Greenwood/Tripp asperity contact model. Most of the user guides of commercial software that allow to perform EHD simulations suggest to assume the standard deviation of the asperity heights of the two surfaces (whose composition is σ_s) equal to the *Root Mean Square (RMS)* of the asperity heights of the whole profiles, R_q [116]. In general, this parameter is not provided in engineering drawings, and it is suggested to relate its value to the average height R_a adopting relations listed in Table 9.1:

	$\frac{R_q}{R_a}$
For a simple sine wave	1.11
For Gaussian distribution of surface heights	1.25
For honing	1.45

Table 9.1. Relation between R_q and R_a

A limited literature can be found focusing on how to evaluate the necessary input data β and η. In [12] Greenwood and Tripp suggest that, according to empirical evidences obtained

adopting the equipment described by Greenwood and Williamson in [54], the product $\sigma_s \beta \eta$ is reasonably constant with standard values ranging in the interval 0.03-0.05. In [117] Arcoumanis calculates this parameter using the composite equivalent spectral moments of the surfaces. In [118] Tomanik et al. propose a simple procedure to evaluate the Greenwood/Williamson input data from a measured linear roughness profile. Commercial software user guides suggest to adopt:

$$0.01 < \sigma_s \beta \eta < 0.05 \; ; \; 0.01 < \sqrt{\frac{\sigma_s}{\beta}} \; 0.1 \text{ [116]}$$

or directly,

$$0.0003 \leq K \leq 0.003 \text{ [119]}$$

Empirical validation of the Greenwood and Tripp model in automotive journal bearings can be found in [120] and [121].

In this section, the roughness profiles of the surfaces of the conrod small-end/piston pin coupling analyzed in section 6 are measured adopting an optical measurement equipment. The roughness profile of the outer surface piston pin was measured on a new part, while the roughness profile of the inner surface of the small-end comes from an used conrod. Considering that a DLC Coating is applied to the outer surface of the piston pin, is it possible to assume that this measurement allows to take into account the flattening of the highest asperity peak due to wear. The proposed simulation method allows to simply implement a wear model to update the Greenwood/Tripp curve at every simulation step, considering the calculated asperity contact pressure and the plasticization limit of the material. In this work, this aspect was not investigated and the relation between asperity contact pressure and oil film thickness is the same during the whole simulation time. An algorithm is proposed, aimed to simply estimate the Greenwood/Tripp roughness parameters from the acquired 3D roughness meshes. The resulting data are used to set the EHD analysis of the coupling. The obtained results are compared with those computed by setting the Greenwood/Tripp model with standard values derived from the pertinent literature and with an alternative modelling of the direct contact problem in which a complementarity approach of the problem is adopted.

9.2 Measurement of the roughness profiles

Measurements of the surface roughness of the outer surface of the piston pin and the inner surface of the conrod small-end of the same high performance motorbike engine addressed in section 6 have been performed in order to derive input data for the asperity contact models considered. Roughness of specimens surface has been measured in accordance to DIN EN ISO 4287/4288 and DIN EN ISO 25178. A Nikon LV 150 Confovis Microscope has been used to assess the surface topography with the following configurations:

- 20x microscopic objective;
- 0.595 μm lateral resolution, 10 nm vertical quantisation and automatic field stitching;
- 1000 x 1000 μm^2 scanned area.

A FALS filter (according to ISO 16610-62), with a cut off of 8 μm by 8 μm, and bilateral symmetric threshold filtering (for the removal of spikes) have been applied to the maps for the form removal. Figure 9.1 shows the measured profiles.

The 3D surface average roughness (S_a) has been calculated on the maps. Surface homogeneity has been checked in advance to validate the operation. S_a provides a comprehensive measurement of the surface morphology.

Surface Skewness (S_{sk}) and Surface Kurtosis (S_{ku}) of height distribution have been calculated. S_{sk} describes the asymmetry of peaks/valleys with respect to the median plane. When $S_{sk} = 0$, the measured surface has peaks and valleys symmetrically distributed with respect to the median plane. With $S_{sk} < 0$ valleys are predominant, while $S_{sk} > 0$ indicates a surface preferentially formed of peaks. S_{ku} describes the sharpness of the peaks/valleys. A high value of S_{ku} (> 3) denotes the existence of very sharp peaks. The Abbott-Firestone curve was obtained, which allows to identify separately the height of the peaks (S_{pk}) and the depth of the valleys (S_{vk}).

The measured roughness profiles and the relative Abbott-Firestone curves are shown in Figure 9.1 to Figure 9.3.

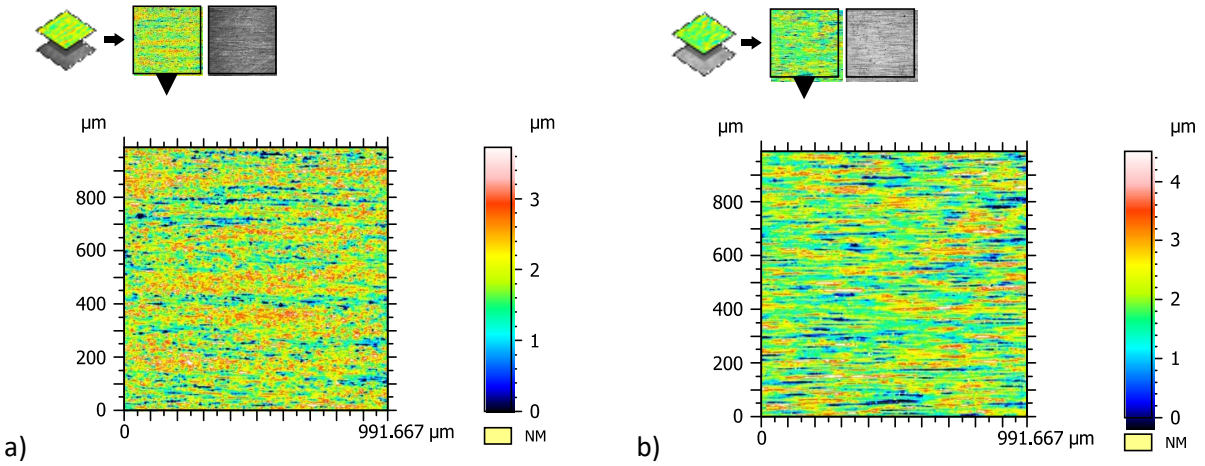

Figure 9.1. Measured profiles: a) Conrod small-end, b) piston pin.

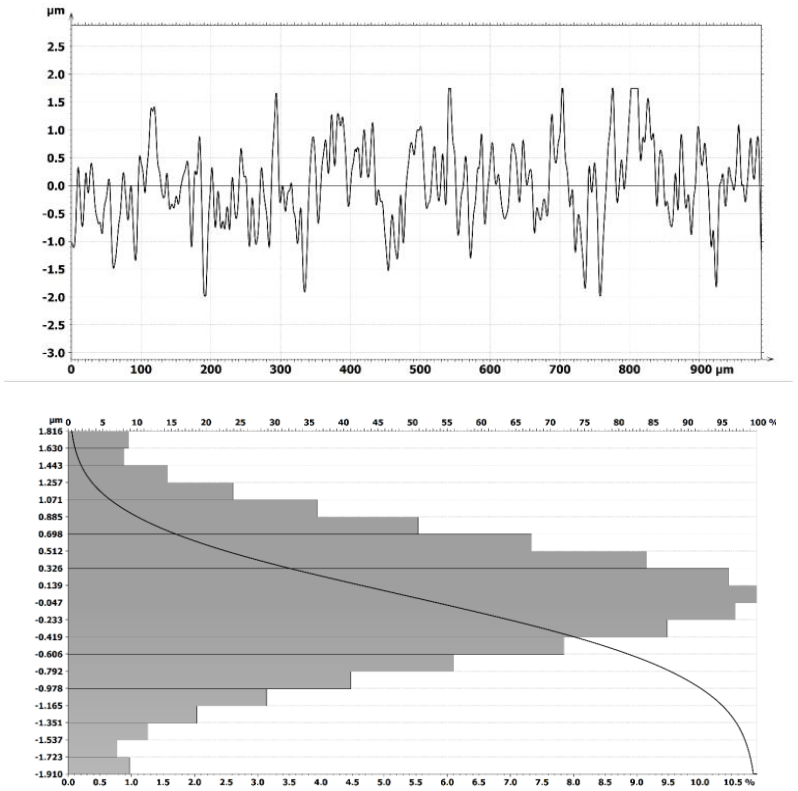

Figure 9.2. Roughness profile and Abbott-Firestone curve for the inner surface of the small-end.

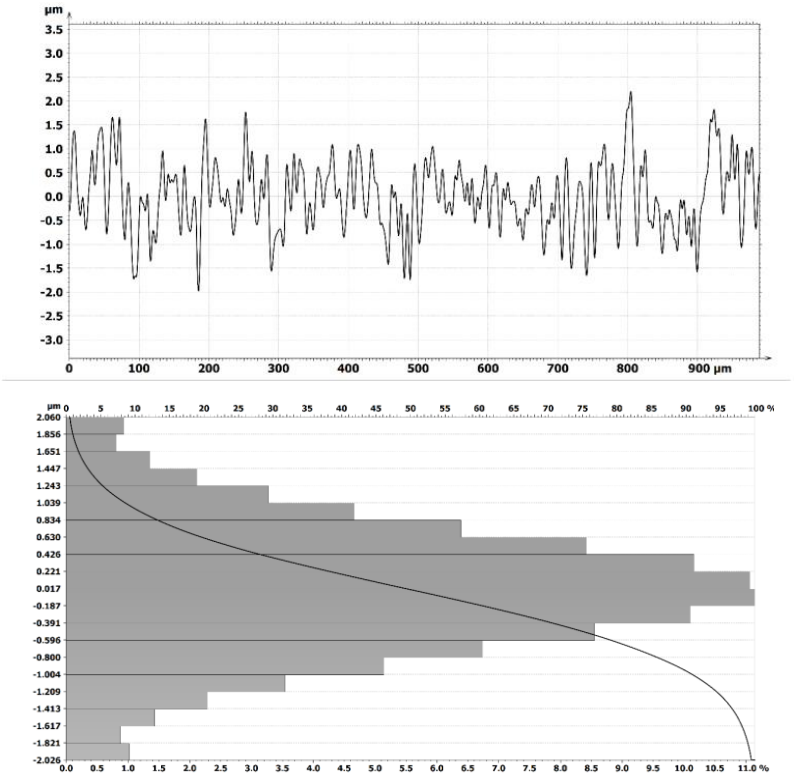

Figure 9.3. Roughness profile and Abbott-Firestone curve for the outer surface of the piston-pin.

9.3 Calculation of the Greenwood/Tripp parameters

9.3.1 Elaboration of the roughness profiles

The measurements provide, for each surface, a 3D map of the roughness profile. A simple procedure has been developed to directly calculate each necessary Greenwood/Tripp roughness parameters, starting from their definition, with particular attention to the evaluation of the mean radius of the asperity peaks, β. Suitable coordinates x and y are considered on the nominal surface, while the coordinate z represents the roughness height. The roughness profiles are provided as a surface mesh in a 3D space, in which the measured nodes are connected by triangular elements. This means that it is quite easy to identify the neighbors of a particular node as the nodes belonging to elements sharing the particular node under consideration.

The developed procedure iterates over the nodes and the following operations are performed at each step i:

1) Verify if the i-th node has four or more neighbors. If the number of neighbors is less than four, the i-th node is not taken into consideration as a possible peak. This passage is necessary to discard edges or zones in which the measured mesh presents holes, even related to local measurement errors.
2) Consider the height of the i-th node and, if it is above the mean surface, compare it with the height of its neighbors. If no neighbor node presents a higher peak, the i-th nodes is an asperity peak and its high z_i will be employed for the calculation of Greenwood/Tripp parameters.
3) If the i-th node is an asperity peak, for each neighbor node, the radius β_{ij} is evaluated of a sphere sharing both the i-th node and the j-th neighbor, and having its center at the same x and y coordinates of the node i. The radius β_i of the sphere used to approximate the asperity peak is the minimum between the evaluated radii, see Figure 9.4. A detailed discussion about the method used to estimate the radius β_i is reported in a specific following section.

At the end of this iteration process, the asperity peaks are isolated from the rest of the profiles, and for each k-th summit, the radius β_k of its approximating sphere and its height δ_k are known.

For each measured surface, it is now possible to estimate the Greenwood/Tripp parameters as:

$$\begin{aligned} \delta_{s1,2} &= \frac{1}{n_s}\sum_{k=1}^{n_s}\delta_k \\ \sigma_{s1,2} &= \sqrt{\frac{1}{n_s}\sum_{k=1}^{n_s}\delta_k^2} \\ \beta_{1,2} &= \frac{1}{n_s}\sum_{k=1}^{n_s}\beta_k \\ \eta_{1,2} &= \frac{n_s}{measured\ Area} = \frac{n_s}{(\max(x)-\min(x))*(\max(y)-\min(y))} \end{aligned} \tag{9.1}$$

where n_s is the number of the asperity summits.

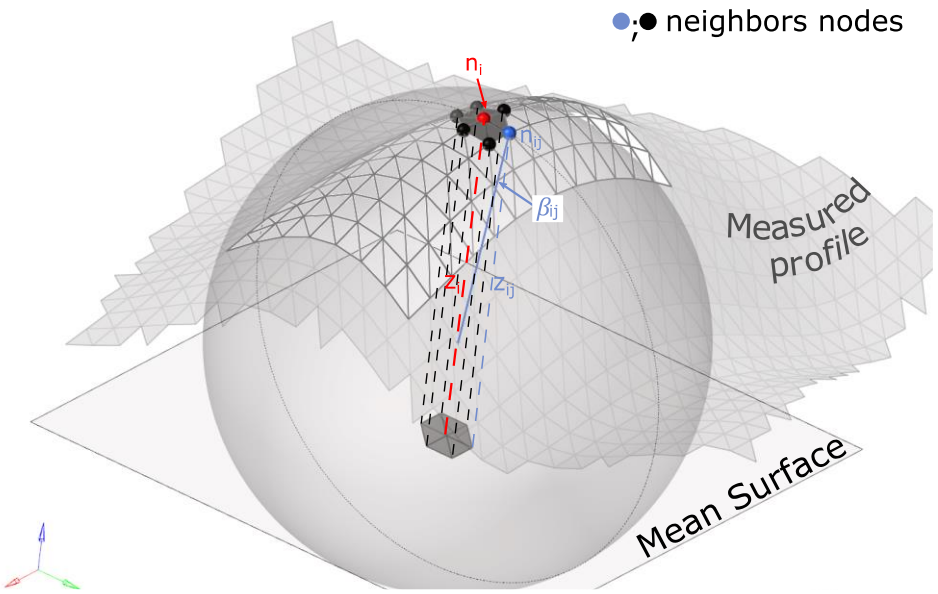

Figure 9.4. Elaboration of the *i*-th node.

9.3.2 Calculation of asperity radius

The definition of the asperity summit radius β is extremely open to several interpretations. The sphere that best approximates the shape of the summits is far from being well defined and a selection of criteria can be identified.

In the case of linear roughness profiles, like those resulting from measurements performed using the stylus instrument, the problem can be easily solved assuming the radius of the circle that passes through the local maximum z_i and its nearest neighbors (z_{i-1}, z_{i+1}) as the radius of the sphere that approximate the peak [118].

In this contribution, where a 3D map of the roughness of the surfaces is provided, the radius β_k of the k-th summit is assumed to be the minimum among the radii of the spheres that have the center on the segment corresponding to the projection of the peak on the nominal surface and pass through the peak node and one of its neighbors.

Figure 9.5 clarifies the procedure and it shows a section of the roughness mesh obtained with a cutting plane passing through the k-th summit and one of its j-th neighbors and normal to the nominal surface.

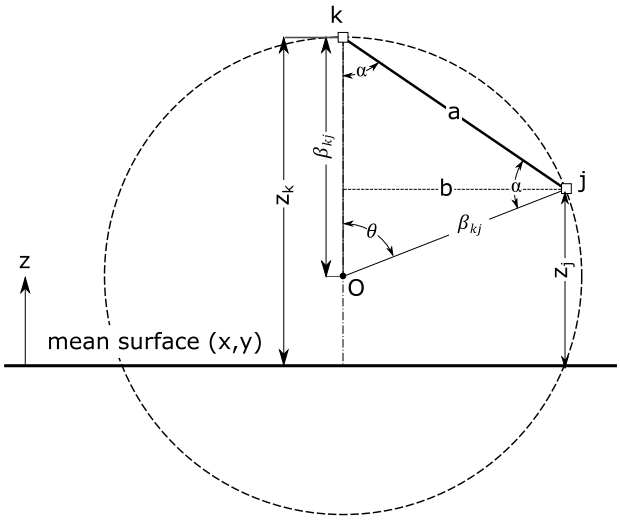

Figure 9.5. Scheme for the identification of summit radius.

The coordinates of the two nodes are known from the measurement, so the two segments a and b can be written as:

$$a = \sqrt{\left(x_k - x_j\right)^2 + \left(y_k - y_j\right)^2 + \left(z_k - z_j\right)^2}$$
$$b = \sqrt{\left(x_k - x_j\right)^2 + \left(y_k - y_j\right)^2} \tag{9.2}$$

The center O is at the same x and y of the peak k. The triangle Okj is isosceles, so it is easy to find:

$$\alpha = \operatorname{asin}\left(\frac{a}{b}\right)$$
$$\theta = \pi - 2 * \alpha \tag{9.3}$$

The segment a is a chord for the circumference centered in O with radius β_{kj} so it is possible to easily write:

$$a = 2 * \beta_{kj} * \sin\left(\frac{\theta}{2}\right) \Rightarrow \beta_{kj} = \frac{a}{2\sin\left(\frac{\theta}{2}\right)} \tag{9.4}$$

The minimum between the radius β_{kj}calculated for each j-th neighbor node is assumed as the radius β_k of the sphere that approximate the summits. Figure 9.6 shows the results of this approach on a portion of the roughness patch of the conrod small end.
Finally, the mean summit radius of the surface's summit β is the mean of the calculated β_k.

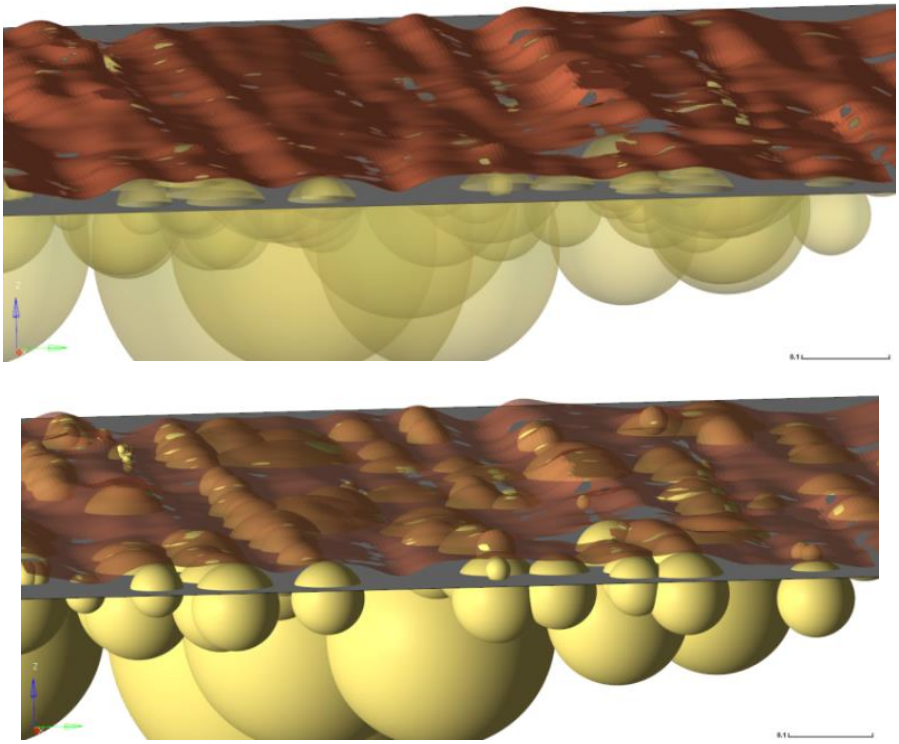

Figure 9.6. Visualization of the calculated approximating spheres on a portion of the roughness patch of the conrod small end.

9.3.3 Resulting Greenwood/Tripp parameters

The resulting Greenwood/Tripp non-standard roughness parameters for the two mating surfaces investigated are shown in Table 9.2.

Parameter		**Conrod SE (1)**	**Piston Pin (2)**
$S_{a\,1,2}$	**[µm]**	0.552	0.638
$S_{q\,1,2}$	**[µm]**	0.694	0.811
$\frac{S_q}{S_a}_{1,2}$	**[-]**	1.258	1.271
$\delta_{s\,1,2}$	**[µm]**	0.626	0.593
$\frac{\delta_s}{S_a}_{1,2}$	**[-]**	1.136	0.930
$\sigma_{s\,1,2}$	**[µm]**	0.876	0.965
$\frac{\sigma_s}{S_a}_{1,2}$	**[-]**	1.587	1.513
$\beta_{1,2}$	**[µm]**	5.043	4.899
$\frac{\beta}{S_a}_{1,2}$	**[-]**	9.144	7.681
$\eta_{1,2}$	**[1/mm²]**	7202	6688
$\sigma_s\beta\eta_{1,2}$	**[-]**	0.032	0.032
$\sqrt{\frac{\sigma_s}{\beta}}_{1,2}$	**[-]**	0.309	0.354

Table 9.2. Resulting Greenwood Tripp Parameter

The parameters are referred as surface roughness parameters, so the arithmetical mean height of the whole surface patch S_a and its root mean square S_q are reported instead of their linear equivalents R_a and R_q. It can been notice that the relation

$$\frac{S_q}{S_a} \approx 1.25 \tag{9.5}$$

shown in Table 9.1 for a Gaussian distribution of surface heights is validated. At the same time a slightly higher ratios of about $1.5 \div 1.6$ have been found between the values σ_s and S_a. The mean summits height δ_s has been found almost equal the arithmetical mean height of the whole profile S_a for both the measured surfaces.

In order to refer to the composite roughness profile, the roughness parameters of the two surfaces must be properly combined. Table 9.3 shows the composite values calculated.

Parameter		**Formula**	**Value**
$\boldsymbol{\delta_s}$	**[µm]**	$\delta_{s1} + \delta_{s2}$	1.220
$\boldsymbol{\sigma_s}$	**[µm]**	$\sqrt{\sigma_{s1}^2 + \sigma_{s2}^2}$	1.303
$\boldsymbol{\beta}$	**[µm]**	$mean(\beta_1, \beta_2)$	4.971
$\boldsymbol{\eta}$	**[1/mm²]**	$mean(\eta_1, \eta_2)$	6945
$\boldsymbol{\sigma_s\beta\eta}$	**[-]**	$\sigma_s\beta\eta$	0.045
$\sqrt{\boldsymbol{\sigma_s/\beta}}$	**[-]**	$\sqrt{\sigma_s/\beta}$	0.512
$\boldsymbol{K}$	**[-]**	$\frac{16\sqrt{2\pi}}{15}(\sigma_s\beta\eta)^2\sqrt{\sigma_s/\beta}$	0.00491

Table 9.3. Composite Greenwood/Tripp parameters.

Looking at the composite values, the product $\sigma_s\beta\eta$ has been found near the superior limit of the typical range $0.01 \div 0.05$, while a value has been found for $\sqrt{\sigma_s/\beta}$ which is out the standard range $0.01 \div 0.1$. Consequently, the resulting value of *K* has been found slightly higher than the usually indicated range $0.0003 \div 0.003$.

9.4 Asperity Contact Model Calibration

The G/T asperity contact model has been set adopting the calculated non-standard roughness parameters (*Case 1*). The results have been compared with those obtained adopting the LCP asperity contact model (*Case 2*), where the measured S_a values have been used to estimate the surfaces gap at incipient metal to metal contact, h_0.

In order to investigate the influence of the governing parameters, a third simulation case (*Case 3*) has been considered in which the Greenwood/Tripp roughness parameters have been estimated starting from the sole value of the measured S_a of the two surfaces while the elastic factor *K* has been chosen equal to the superior limit of the typical range $0.0003 \div 0.003$ [119]. Table 9.4 reassumes the setting of the asperity contact models for the three cases considered.

Case 1. Measured Greenwood/Tripp parameters			
Parameter	**Formula**	**Value**	Unit
$\boldsymbol{\delta_{s\,1}}$	-measured-	0.626	[μm]
$\boldsymbol{\delta_{s\,2}}$	-measured-	0.593	[μm]
$\boldsymbol{\delta_s}$	$\delta_{s1} + \delta_{s2}$	1.220	[μm]
$\boldsymbol{\sigma_{s\,1}}$	-measured-	0.876	[μm]
$\boldsymbol{\sigma_{s\,2}}$	-measured-	0.965	[μm]
$\boldsymbol{\sigma_s}$	$\sqrt{\sigma_{s1}^2 + \sigma_{s2}^2}$	1.303	[μm]
$\boldsymbol{K}$	$\frac{16\sqrt{2\pi}}{15}(\sigma_s\beta\eta)^2\sqrt{\frac{\sigma_s}{\beta}}$	0.00491	[-]
Case 2. Linear Complementarity model, measured Sa			
Parameter	**Formula**	**Value**	**Unit**
$\boldsymbol{h_0}$	$S_{a\,1} + S_{a\,2}$	1,190	[μm]
Case 3. Greenwood/Tripp parameters estimated from measured S_a			
Parameter	**Formula**	**Value**	**Unit**

$\boldsymbol{\delta_{s\,1}}$	$S_{a\,1}$	0.552	[μm]
$\boldsymbol{\delta_{s\,2}}$	S_{a2}	0.638	[μm]
$\boldsymbol{\delta_s}$	$\delta_{s1} + \delta_{s2}$	1.190	[μm]
$\boldsymbol{\sigma_{s\,1}}$	$1.25 * S_{a\,1}$	0.690	[μm]
$\boldsymbol{\sigma_{s\,2}}$	$1.25 * S_{a\,2}$	0.797	[μm]
$\boldsymbol{\sigma_s}$	$\sqrt{\sigma_{s1}^2 + \sigma_{s2}^2}$	1.054	[μm]
$\boldsymbol{K}$	-taken from literature- [119]	0.003	[-]

Table 9.4. Asperity contact model calibration for each case.

Figure 9.7 shows the asperity contact pressure-clearance height relationship for the simulation cases.

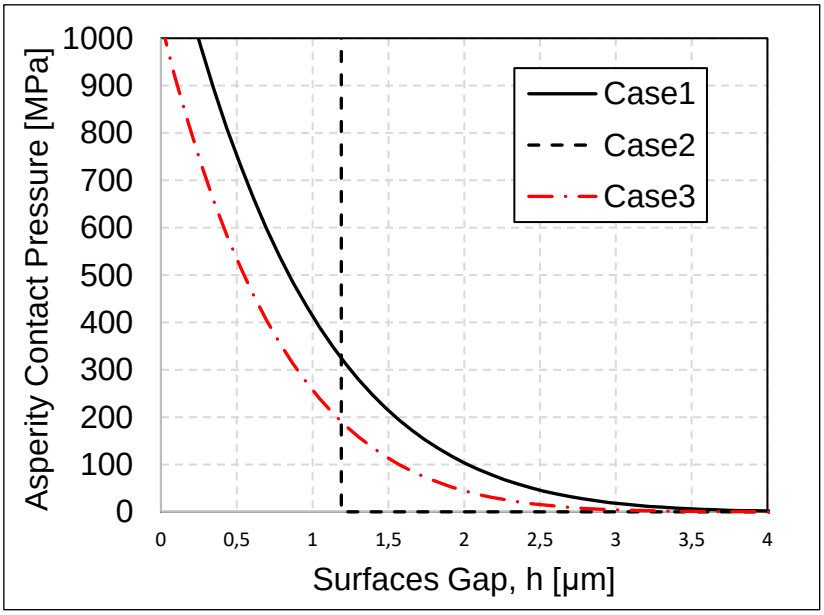

Figure 9.7. Asperity contact pressure-clearance height relation for the simulation cases

9.5 Results

The results are shown in terms of minimum oil film thickness, peak values of hydrodynamic, asperity and total pressure along a single engine cycle, and pressure and void ratio

distributions averaged over the engine cycle. Note that the second simulated engine cycle has been considered in order to avoid variables initialization issues.

9.5.1 Minimum oil film thickness (MOFT) and maximum pressure

Figure 9.8, Figure 9.9, Figure 9.10, Figure 9.11 compare respectively the minimum oil film thickness (MOFT) and the maximum hydrodynamic, asperity contact and total pressure registered along the whole engine cycle, for each simulation case.

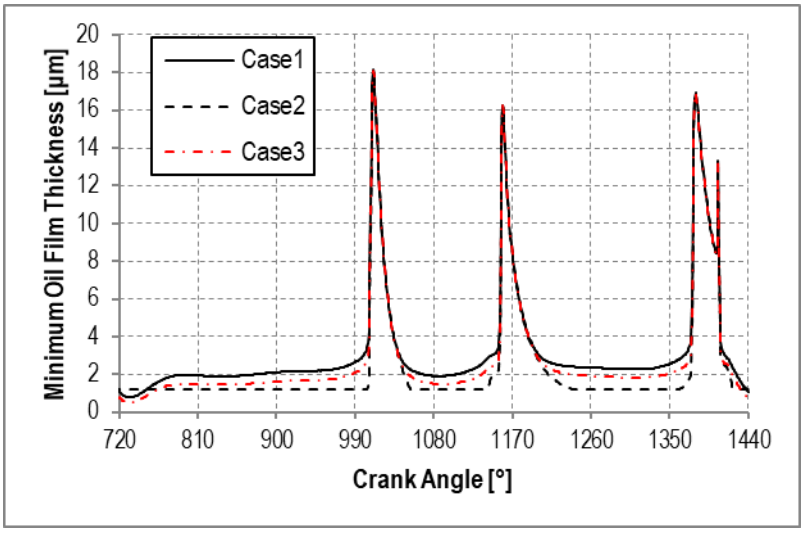

Figure 9.8. Comparison between minimum oil film thickness calculated for each simulation case.

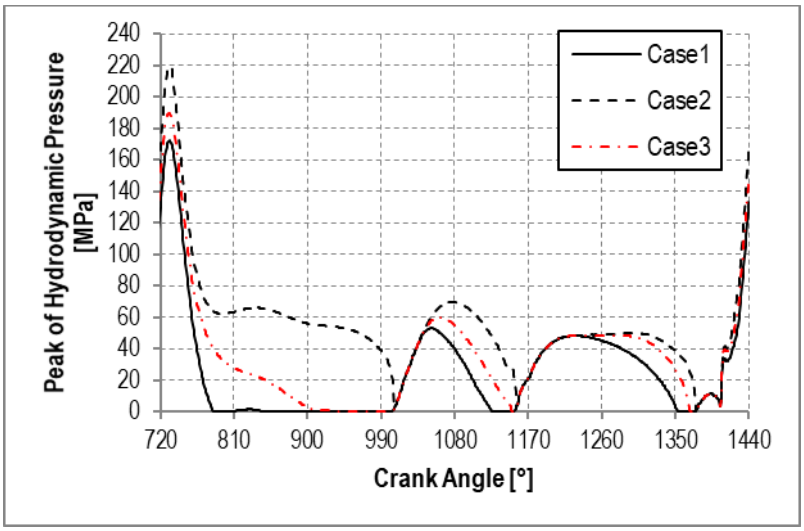

Figure 9.9. Comparison between peak of hydrodynamic pressure calculated for each simulation case.

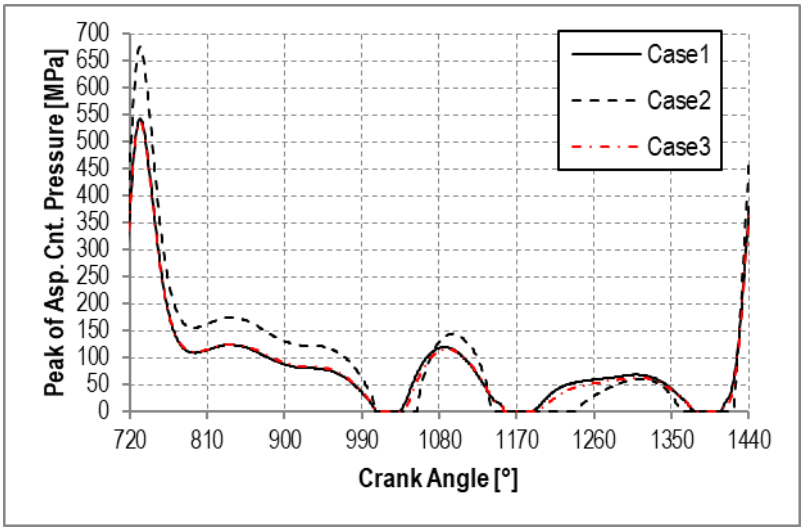

Figure 9.10. Comparison between peak of asperity contact pressure calculated for each simulation case.

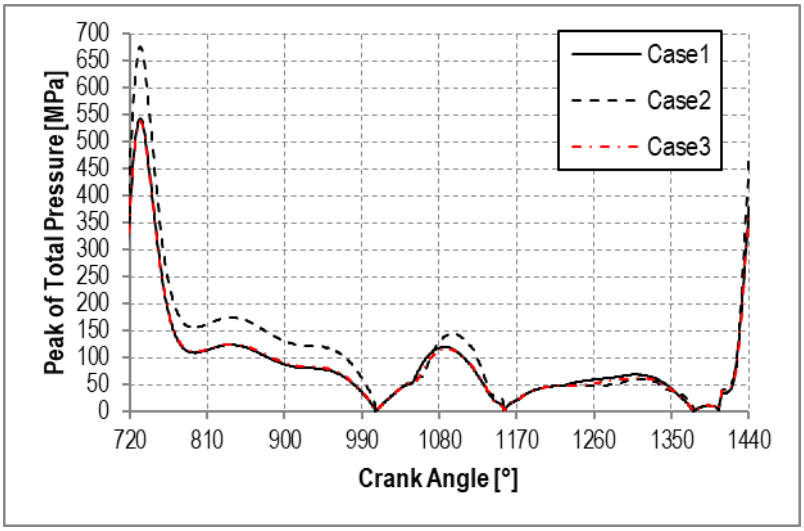

Figure 9.11. Comparison between peak of total pressure calculated for each simulation case.

The highest MOFT values are the same for each simulation case and are registered where no direct metal to metal contact occurs. At these crank angles, the asperity contact pressure is zero, and the (quite small) load is completely sustained by the hydrodynamic pressure.

The lowest MOFT values are registered during combustion, where both hydrodynamic and asperity contact pressure rapidly increase to their highest values. The complementarity algorithm (*Case 2*) prevents a minimum film thickness lower than h_0 to be obtained, while lower values are registered adopting the Greenwood/Tripp method.

The MOFT values of *Case 1* are generally the highest ones, due to the stiffer relation between surface gap and contact pressure. For the same reason, the peaks of hydrodynamic pressure

are generally lower for this case, being higher the percentage of the external load sustained by the direct contact pressure. The maximum values of the asperity contact pressure registered for *Case 1* and *Case 3* are almost the same, thus suggesting that the distribution of the asperity contact pressure of the *Case 3* is more concentrated.
Case 2 registers the minimum value of minimum oil film thickness and the maximum values of both asperity and hydrodynamic pressure. This is due to the discontinuous behavior of the linear complementarity model, that predicts very concentrated areas in the mixed lubrication regime, since no load sustainment is provided by metal to metal contact till the surfaces' gap does not reach the critical value h_0.

9.5.2 Pressure Distributions

Figure 9.12 compares the hydrodynamic pressure distribution averaged over the whole engine cycle obtained for the three simulation cases. The highest values of the hydrodynamic pressure are registered at the center of the simulation domain, in correspondence of the conrod shank. This is consistent with the fact that the highest value of the hydrodynamic load sustainment is registered during combustion, when the piston pin is pushed by gas toward the shank, producing a strong squeeze effect.

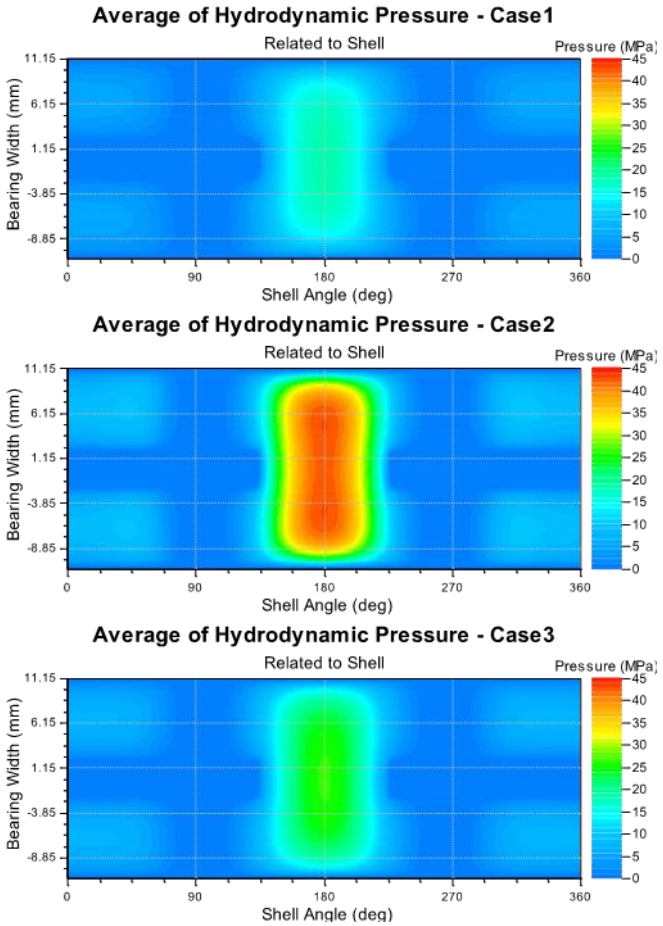

Figure 9.12. Comparison between mean hydrodynamic pressure distributions.

At the axial extremity of the small end, the hydrodynamic sustainment falls to zero (boundary conditions are applied), and asperity contact pressure arises, Figure 9.13. This is due to the bending of the piston pin at combustion, that makes the surfaces gap lower at the external boundary, where minima values of film thickness are detected.

Even if the highest values of averaged hydrodynamic and asperity pressure are registered in the same zones for the three cases, the pressure distribution and absolute values are strongly different.

In particular, the asperity contact pressure distribution is strongly concentrated for *Case 2*, that adopts the linear complementarity formulation of the direct metal to metal contact, resulting in higher values of hydrodynamic pressure in the whole simulation domain.

Case 1 predicts an extend zone at high value of asperity contact pressure in the vicinity of conrod shank, also shared by *Case 3*, where, however, lower values are registered.

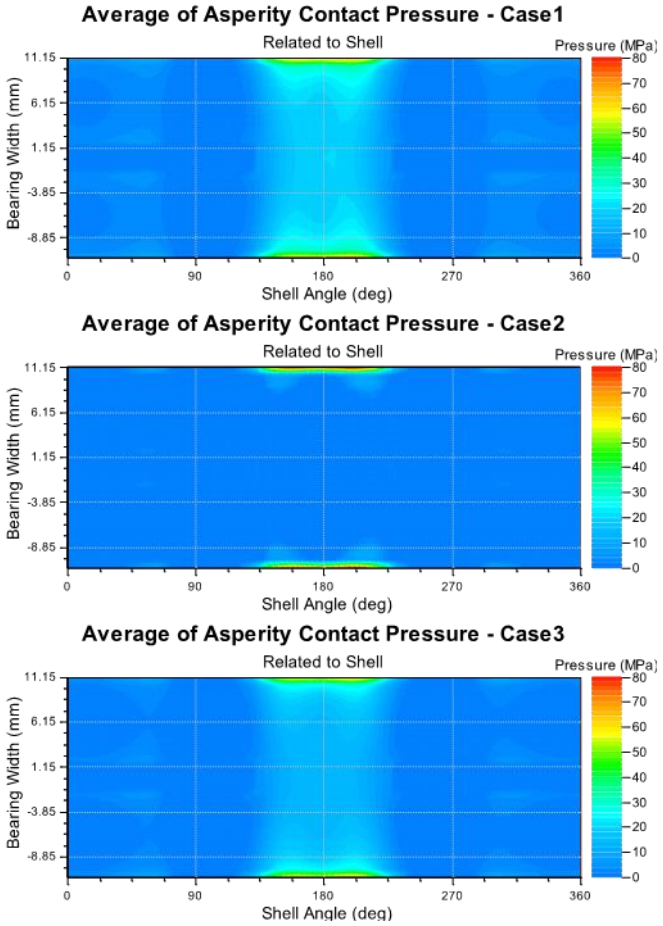

Figure 9.13. Comparison between mean asperity contact pressure distributions.

Figure 9.14 shows a comparison of the averaged distribution of void ratio. The averaged void fraction distributions are similar for the three cases. The small-end groove prevents the void fraction to be high at the center of the simulation domain, in correspondence of the upper portion of the small-end inner surface. The highest vales of r are registered at the top of the small end, in a middle section between the axial position of the groove and the external boundaries of the simulation domain. Relevant averaged values are also registered in the vicinity of the conrod shank, while no cavitation is predicted at the external boundaries.

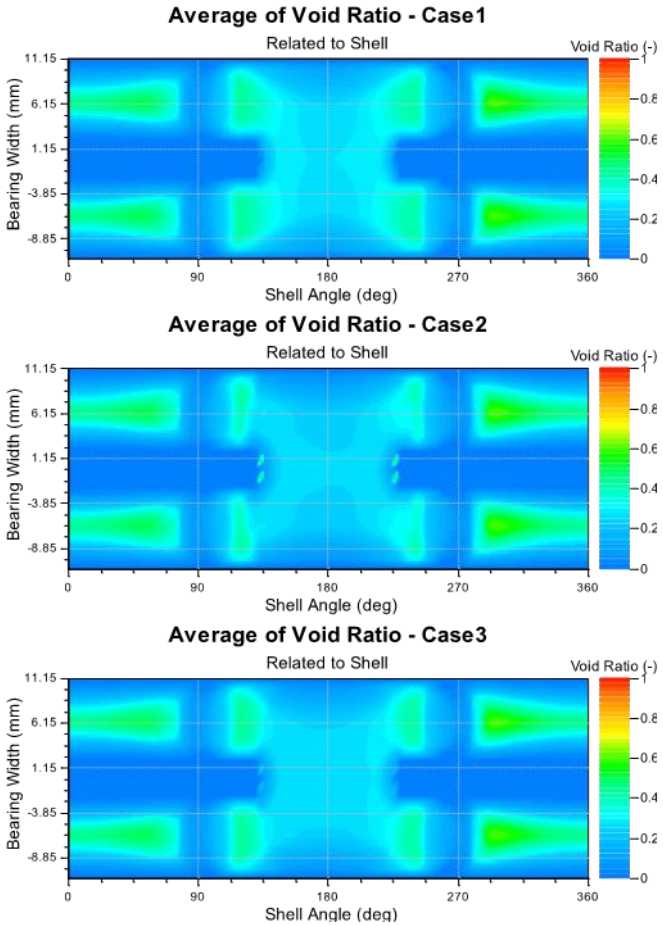

Figure 9.14. Comparison between mean void ratio distributions.

10. Conclusions

In this PhD activity, a methodology based on a linear complementarity formulation of the Reynold equation was developed, capable of predicting the tribological behavior of lubricated contact, handling both the cavitation and asperity contact problems.

A particular focus has been placed on the influence on the results of the choice of the particular asperity contact model, and its calibration. Two different asperity contact models have been implemented, the former based on the standard Greenwood-Tripp theory and the latter based on a complementarity formulation of the asperity contact problem, and the results have been compared. An analysis has been performed of the tribological behavior of the lubricated contact between the piston pin and the conrod small-end of a high performance motorbike engine.

It has been shown that similar results can be obtained from both the approaches, if a calibration of the model input data is performed. However, a remarkable sensitivity has been highlighted of the results obtained using the Greenwood/Tripp model to the adjustment parameters. The realistic (engineering) difficulty in defining and identifying the roughness data and their purely statistical nature, return results that may be afflicted by a dose of uncertainty.

Different set of parameters have been selected for the Greenwood/Tripp model set up, consistent with the same measured roughness data. A non-negligible difference in the MOFT values and pressure distributions has been obtained from the different simulations. As shown by the sensitivity analysis, non-negligible difference in the pressure fields can be obtained from simulations set with input parameters consistent with the same known roughness data.

A validation of the proposed algorithm has been performed comparing results with those obtained adopting the commercial software AVL Excite Power Unit. The influence of the main parameters governing the Excite model on the results has been investigated. Consistent solutions have been obtained from the different simulations thus corroborating both the accuracy of the Excite model and validating the proposed algorithm.

Considering that results of such simulations usually offer guidelines for a correct design of the coupling, an investigation was performed to identify a relationship between available roughness data and model input, starting from direct experimental measurements of real roughness profiles. A suitable procedure has been implemented to calculate the necessary non-standard Greenwood/Tripp parameters.

The calculated elastic factor value has been found higher than the superior limit of the range $0.0003 < K < 0.003$ typically suggested by literature, while the relation between S_q and S_a roughness and the value of the product $\sigma_s \beta \eta$ have been found consistent with the standard values. The resulting roughness parameter was employed to calibrate both the Greenwood/Tripp and LCP asperity contact model.

An additional simulation has been performed, set adopting the usually suggested relations $\sigma_s = S_q = 1.25 * S_a$, $\delta_s = S_a$ and the stiffer value found in literature for the elastic factor $K = 0.003$.

The three simulations show the same critical zones, in terms of averaged asperity contact pressure and void ratio, even if relevant differences have been highlighted between the absolute values of the output governing parameters.

The registered peak of the asperity contact pressure is very high (above 500 MPa). Considering that the contact under investigation is a bushless steel conrod small-end /steel piston-pin coupling, they still behave in the elastic regime. It would be different for example at the interface between piston-pin and piston (the piston is usually manufactured in aluminum). An interesting future development of this work can be the investigation of the effect of the consideration of a worn surface.

The wear's effects can be further investigated even adopting a suitable asperity peak plasticization model.

Figures 15 and 16 show a preliminary comparison of the distribution of asperity contact pressure and void ratio with conrod small-end failures occurred during experimental tests of the engine at an early stage of the design process and under severe testing conditions. A good agreement can be noticed between the simulation results and empirical evidence of wear and cavitation erosion. Further investigations can be performed possibly adopting the cavitation damage index proposed in [79].

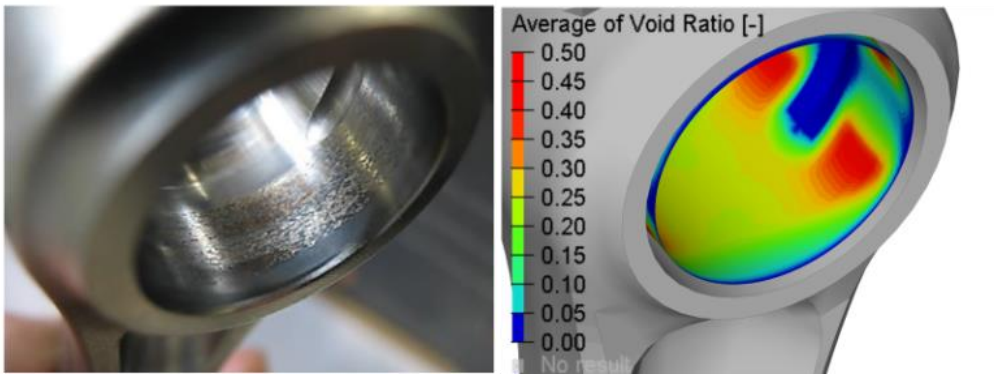

Figure 10.1. Comparison between calculated distribution of void ratio and empirical evidence.

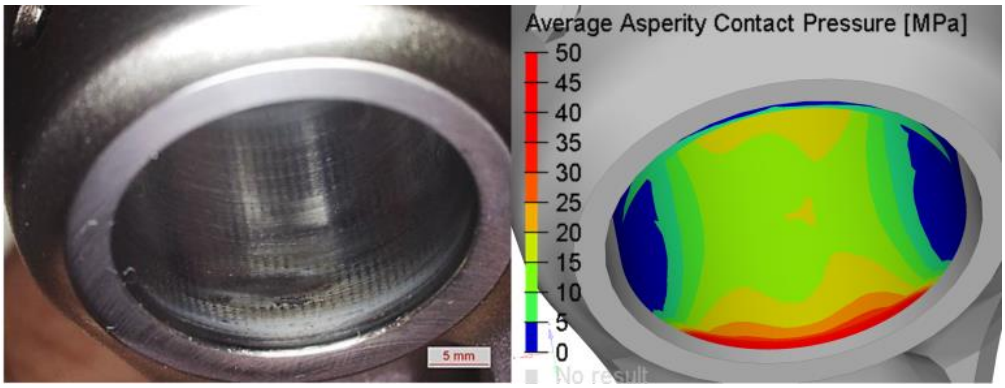

Figure 10.2. Comparison between calculated distribution of asperity contact pressure and empirical evidence.

References

[1] A. Watson, R. Bates and D. Kennedy, Air Pollution, the Automobile, and Public Health, Washington (DC): National Academic Press (US), 1988.

[2] W. V. Wong and S. C. Tung, "Overview of automotive engine friction and reduction trends–Effects of surface, material, and lubricant-additive technologies," *Friction,* vol. 4, no. 1, pp. 1-28, 2016.

[3] D. Richardson, "Review of Power Cylinder Friction for Diesel Engines," *Journal of Engineering for Gas Turbines and Power,* vol. 122, no. 4, pp. 506-519, 2 04 2000.

[4] J.-L. Ligier and B. Noel, "Friction Reduction and Reliability for Engines Bearings," *Lubricants,* vol. 3, pp. 569-596, 23 07 2015.

[5] M. T. Devlin, "Common Properties of Lubricants that Affect Vehicle Fuel Efficiency: A North American Historical Perspective," *Lubricants,* vol. 6, no. 3, p. 68, 2018.

[6] L. Ba, Z.-p. He, Y.-h. Liu e G.-c. Zhang, «Analysis of piston-pin lubrication considering the effects of structure deformation and cavitation,» *Journal of Zhejiang University-SCIENCE A,* vol. 16, n. 6, pp. 443-463, 2015.

[7] C. Zhang, H. Cheng, L. Qiu and K. W. Knipstein, "Scuffing Behaviour of Piston-Pin/Bore Bearing in Mixed Lubrication-Part I: Experimental Studies," *Tribology Transactions,* vol. 42, no. 2, pp. 193-199, 2003.

[8] C. Zhang, H. Cheng, L. Qiu and K. W. Knipstein, "Scuffing Behaviour of Piston-Pin/Bore Bearing in Mixed Lubrication-Part II: Scuffing Mechanism and Failure Criterion," *Tribology Transactions,* vol. 47, no. 1, pp. 149-156, 2004.

[9] L. Bertocchi, M. Giacopini, D. Dini e M. Fowell, «A Mass-Conserving Complementarity Formulation to Study Fluid Film Lubrication in the Presence of Cavitation for Non-Newtonian and Compressible Fluids,» in *ASME 2012 11th Biennial Conference on Engineering Systems Design and Analysis, ESDA*, Nantes, France, 2012.

[10] M. Giacopini, D. Dini, M. Fowell and A. Strozzi, “A Mass-Conserving Complementarity Formulation to Study Lubricant Films in the Presence of Cavitation,” *Journal of Tribology,* vol. 4, no. 132, 2010.

[11] A. Strozzi, “Formation of three lubrication problems in terms of complementarity,” *Wear,* vol. 104, pp. 103-115, 1985.

[12] J. A. Greenwood and J. H. Tripp, “The Contact of Two Nominally Flat Rough Surfaces,” *Proceedings of the Institution of Mechanical Engineers,* vol. 185, no. 48, pp. 625-634, 1970.

[13] B. Bhushan, “Contact mechanics of rough surfaces in tribology: multiple asperity contact,” *Tribology Letters,* vol. 4, no. 1, pp. 1-35, 01 01 1998.

[14] B. Jakobsson and L. Floberg, The finite Journal Bearing, considering vaporization, Göteborg: Gumperts Förlag, 1957.

[15] L. Floberg, Experimental investigation of cavitation regions in journal bearings, Cornell: Transactions of Chalmers University of Technology, 1961.

[16] L. Floberg, «Cavitation Boundary Conditions with Regard to the Number of Streamers and Tensile Strength of the Liquid,» in *Cavitation and Related Phenomena in Lubrication*, England, ImechE, 1974, pp. 31-36.

[17] D. C. Sun and D. E. Brewe, “Two Reference Time Scales for Studying the Dynamic Cavitation of Liquid Films,” *Journal of Tribology,* vol. 114, no. 3, pp. 612-615, 01 07 1992.

[18] M. J. Braun and R. C. Hendricks, “An Experimental Investigation of the Vaporous/Gaseous Cavity Characteristics of an Eccentric Journal Bearing,” *A S L E Transactions,* vol. 27, no. 1, pp. 1-14, 1984.

[19] H. Elrod and M. Adams, “A Computer Program for Cavitation and Starvation Problems,” in *Cavitation and Related Phenomena in Lubrication*, vol. 37, Mechanical Engineering Pub, 1974, pp. 37-42.

[20] H. Elrod, “A Cavitation Algorithm,” *ASME Journal of Lubrication Technology,* vol. 103, pp. 350-354, 1981.

[21] D. Brewe, “Theoretical Modeling of the Vapor Cavitation in Dynamically Loaded

Journal Bearings," *ASME Journal of Tribology,* vol. 108, pp. 628-638, 1986.

[22] C. Woods and D. Brewe, "The Solution of the Elrod Algorithm for a Dynamically Loaded Journal Bearing Using Multigrid Techniques," *ASME Journal of Tribology,* vol. 111, pp. 302-308, 1989.

[23] D. Vijayaraghavan and T. Keith, "Development and Evaluation of a Cavitation Algorithm," *Tribology Transactions,* vol. 32, no. 2, pp. 225-233, 1989.

[24] F. Sahlin, A. Almqvist, R. Larsson and S. Glavatskih, "A cavitation algorithm for arbitrary lubricant compressibility," *Tribology International,* vol. 40, no. 8, pp. 1294-1300, 2007.

[25] K. P. Oh, "The Numerical Solution of Dynamically Loaded Elastohydrodynamic Contact as a Nonlinear Complementarity Problem," *Journal of Tribology,* vol. 106, no. 1, pp. 88-95, 1984.

[26] M. Kostreva, «Elasto-hydrodynamic lubrication: A non-linear complementarity problem,» *Int. J. Numer. Methods Fluids,* vol. 4, n. 4, pp. 377-397, 1984.

[27] K. P. Oh e P. K. Goenka, «The Elastohydrodynamic Solution of Journal Bearings Under Dynamic Loading,» *Journal of Tribology,* vol. 107, n. 3, pp. 389-394, 1985.

[28] D. Dowson and G. Higginson, Elasto-Hydrodynamic Lubrication, Oxford: Pergamon Press, 1966.

[29] J. Ståhl e B. O. Jacobson, «Compressibility of Lubricants at High Pressures,» *Tribology Transactions,* vol. 46, n. 4, pp. 592-599, 2003.

[30] R. Tuomas and O. Isaksson, "Compressibility of oil/refrigerant lubricants in elasto-hydrodynamic contacts," *Journal of Tribology,* vol. 128, no. 1, pp. 2187-228, 2006.

[31] B. Jacobson and P. Vinet, "A model for the influence of pressure on the bulk modulus and influence of temperature on the solidification pressure for liquid lubricants," *Journal of tribology,* vol. 109, no. 4, pp. 709-714, 1987.

[32] C. Venner and J. Bos, "Effects of lubricant compressibility on the film thickness in ehl line and circular contacts.," *Wear,* vol. 173, no. 12, pp. 151-165, 1994.

[33] C. Barus, "Isotherms, isopiestics and isometrics relative to viscosity," *American Journal of Science,* vol. 45, pp. 87-96, 1893.

[34] C. Roelands, Correlational aspects of the viscosity-temperature-pressure relationship of lubricant oils, PhD thesis, TU Delft: Delft University of Technology, 1966.

[35] A. K. Doolittle, "Studies in Newtonian Flow. II. the dependence of the viscosity of liquids on free-space," *Journal of applied Physics,* vol. 22, no. 12, pp. 1471-1475, 1951.

[36] D. Gwynllyw, A. Davies and T. Phillips, "On the effect of a piezoviscous lubricant on the dynamics of a journal bearing," *Journal of Rheology,* vol. 40, no. 6, pp. 1239-1266, 1996.

[37] R. Grieve and H. Spikes, "Temperature and Shear Stress in Thin Film EHD Contacts," in *Thinning Films and Tribological Interfaces Proceeding of the 26th Leeds-Lyon Symposium on Tribology*, Elsevier, 2000.

[38] O. Zienkiewicz and F. Emeritus, The Finite Element Method Fifth edition, Volume 3: Fluid Dynamics, Butterworth-Heinemann, 2000.

[39] H. Grandin, Fundamentals of the finite element method, Waveland Press, 1191.

[40] C. J. Hooke, D. J. Lines and J. P. O'Donoghue, "A theoretical study of the lubrication of reciprocating O-ring seals," in *Proc. 3rd Int. Conf. Fluid Sealing*, 1967.

[41] F. H. Theyse, "The inverse hydrodynamic theory and its application in the design of controlled leakage seals between moving parts," in *Proc. 3rd Int. Conf. Fluid Sealing,* 1967.

[42] A. D. Roberts and P. D. Swales, "The elastohydrodynamic lubrication of a highly elastic cylindrical surface," *Brit. J. Appl. Phys,* vol. 2, no. 1317, 1969.

[43] I. A. Gibson, C. J. Hooke and J. P. O'Donoghue, "Elastohydrodynamic lubrication of O-ring seals," *Proc.Instn mech. Engrs,* vol. 184, no. 197, 1970.

[44] C. J. Hooke and J. P. O'Donoghue, "Elastohydrodynamic lubrication of soft, highly deformed contacts," *J. Mech. Engng Sci.,* vol. 14, no. 34, 1972.

[45] K. P. Baglin and J. F. Archard, "An analytic solution of the elastohydrodynamic lubrication of materials of low elastic modulus," in *Proc. Instn mech. Engrs, Symposium on Elastohydrodynamic Lubrication,* 1972.

[46] P. D. Swales, D. Dowson and J. L. Latham, "Theoretical and experimental observations of the behaviour of soft elastic materials under elastohydrodynamic conditions," in

Proc. Instn mech. Engrs, Symposium on Elastohydrodynamic Lubrication, 1972.

[47] G. J. Field and B. S. Nau, "An experimental study of reciprocating rubber seals," in *Proc. Instn mech. Engrs, Symposium on Elastohydrodynamic Lubrication,* 1972.

[48] G. J. Field and B. S. Nau, "A theoretical study of the elastohydrodynamic lubrication of reciprocating rubber seals," *Trans. Am. SOC. lub. Engrs,* vol. 18, no. 48, 1975.

[49] S. M. Rohde and K. P. Oh, "A unified treatment of thick and thin film elastohydrodynamic problems by using higher order element methods," in *Proc. R. Soc.*, 1975.

[50] K. P. Oh and S. M. Rohde, "Numerical solution of the point contact problem using the finite element method," *Int. J. Num. methods Engng,* vol. 11, no. 1507, 1977.

[51] F. P. Bowden and D. Tabor, The Friction and Lubrication of Solids, Part I, Oxford: Clarendon Press, 1950.

[52] F. Bowden and D. Tabor, The Friction and Lubrication of Solids, Part II, Oxford: Clarendon Press, 1964.

[53] B. Bhushan, Tribology and mechanics of magnetic storage devices, Springer Science & Business Media, 2012.

[54] J. A. Greenwood and J. B. Williamson, "Contact of nominally flat surfaces," *Proceedings of the Royal Society of London. Series A. Mathematical and Physical Sciences,* vol. 295, no. 1442, pp. 300-319, 1966.

[55] D. J. Whitehouse and J. Archard, "The properties of random surfaces of significance in their contact," *Proceedings of the Royal Society of London. A. Mathematical and Physical Sciences,* vol. 316, no. 1524, pp. 97-121, 1970.

[56] R. Onions and J. Archard, " The contact of surfaces having a random structure," *Journal of Physics D: Applied Physics,* vol. 6, no. 3, p. 289, 1973.

[57] P. Nayak, "Random process model of rough surfaces in plastic contact," *Wear,* vol. 26, no. 3, pp. 305-333, 1973.

[58] A. Bush, R. Gibson and T. Thomas, "The elastic contact of a rough surface," *Wear,* vol. 35, no. 1, pp. 87-111, 1975.

[59] R. Gibson, "The surface as a random process," *Rough Surfaces,* pp. 119-143, 1982.

[60] J. McCool, “Predicting microfracture in ceramics via a microcontact model,” *Journal of tribology,* vol. 108, no. 3, pp. 380-385, 1986.

[61] T. R. Thomas, “Rough surfaces,” *Rough Surfaces, 2nd Edition. Edited by THOMAS TOM R. Published by World Scientific Publishing Co. Pte. Ltd.,.,* 1999.

[62] H. Francis, “Application of spherical indentation mechanics to reversible and irreversible contact between rough surfaces,” *Wear,* vol. 45, no. 2, pp. 221-269, 1977.

[63] B. Bhushan, “Analysis of the real area of contact between a polymeric magnetic medium and a rigid surface,” *Journal of Tribology,* vol. 106, no. 1, pp. 26-34, 1984.

[64] J. I. McCool, “Comparison of models for the contact of rough surfaces,” *Wear,* vol. 107, no. 1, pp. 37-60, 1986.

[65] W. Chang, I. Etsion and D. B. Bogy, “An elastic-plastic model for the contact of rough surfaces,” *Journal of tribology,* vol. 109, no. 2, pp. 257-263, 1987.

[66] C. A. Kotwal and B. Bhushan, “Contact analysis of non-Gaussian surfaces for minimum static and kinetic friction and wear,” *Tribology Transactions,* vol. 39, no. 4, pp. 890-898, 1996.

[67] J. Williamson, “The microtopography of surfaces,” in *Proceedings of the Institution of Mechanical Engineers, Conference Proceedings,* London, 1967.

[68] P. Gupta and N. Cook, “Junction deformation models for asperities in sliding interaction,” *Wear,* vol. 20, no. 1, pp. 73-87, 1972.

[69] B. Bhushan and N. Cook, “On the correlation between friction-coefficients and adhesion stresses,” *Journal of Engineering Materials and Technology,* vol. 97, no. 3, pp. 285-287, 1975.

[70] R. Sayles and T. Thomas, “Computer simulation of the contact of rough surfaces,” *Wear,* vol. 49, no. 2, pp. 273-296, 1978.

[71] C. Y. Poon and B. Bhushan, “Comparison of surface roughness measurements by stylus profiler, AFM and non-contact optical profiler,” *Wear,* vol. 190, no. 1, pp. 76-88, 1995.

[72] F. Akyuz and J. Merwin, “Solution of nonlinear problems of elastoplasticity by finite elementmethod.,” *AIAA Journal,* vol. 6, no. 10, pp. 1825-1831, 1968.

[73] K. Komvopoulos and D. Choi, “Elastic finite element analysis of multi-asperity

contacts," *Journal of tribology,* vol. 114, no. 4, pp. 823-831, 1992.

[74] H. Francis, "The accuracy of plane strain models for the elastic contact of three-dimensional rough surfaces," *Wear,* vol. 85, no. 2, pp. 239-256, 1983.

[75] W. Lai and H. Cheng, "Computer simulation of elastic rough contacts," *ASLE transactions,* vol. 28, no. 2, pp. 172-180, 1985.

[76] M. Webster and R. Sayles, "A numerical model for the elastic frictionless contact of real rough surfaces," *Journal of tribology,* vol. 108, no. 3, pp. 314-320, 1986.

[77] X. Tian and B. Bhushan, "A numerical three-dimensional model for the contact of rough surfaces by variational principle," *Journal of tribology,* vol. 118, no. 1, pp. 33-42, 1996.

[78] M. Giacopini, L. Bertocchi, A. Baldini and D. Dini, "A Complementarity Formulation for the EHL Analysis of a Connecting Rod Big End Bearing," in *5th WTC*, Torino, Italy, 2013.

[79] D. Dini, L. N. Mastrandrea, M. Giacopini and E. Bertocchi, "Numerical Investigation of the Cavitation Damage in a High Performance ENGINE Conrod Big End Bearing Via a Mass-Conserving Complementarity Algorithm," in *Society of Tribologists and Lubrication Engineers Annual Meeting and Exhibition*, Lake Buena Vista, United States, 2014.

[80] L. N. Matrandrea, M. Giacopini, D. Dini and E. Bertocchi, "Elastohydrodynamic Analysis of the Conrod Small-End of a High Performance Motorbike Engine Via a Mass Conserving Cavitation Algorithm," in *ASME International Mechanical Engineering Congress and Exposition 15*, Houston,Texas, 2015.

[81] A. A. Cannarozzi, «On the resolution of some unilaterally constrained problems in structural engineering,» *Computer Methods in Applied Mechanics and Engineering - COMPUT METHOD APPL MECH ENG*, vol. 24, pp. 339-357, 1980.

[82] Y. Hu, H. S. Cheng, T. Arai, Y. Kobayashiy e S. Aoyama, «Numerical Simulation of Piston Ring in Mixed Lubrication—A Nonaxisymmetrical Analysis,» *Journal of Tribology,* vol. 116, n. 3, pp. 470-478, 1994.

[83] R. Jedynak e J. Gilewicz, «Approximation of the Integrals of the Gaussian Distribution

of Asperity Heights in the Greenwood-Tripp Contact Model of Two Rough Surfaces Revisited,» *J. Appl. Math.,* 2013.

[84] L. Wei and H. Wei, "An EHD-mixed lubrication analysis of main bearings for diesel engine based on coupling between flexible whole engine block and crankshaft," *Industrial Lubrication and Tribology,* vol. 67, no. 2, pp. 150-158, 2015.

[85] K. Murty, Linear and Nonlinear Programming, Lemgo, Germany: Heldermann-Verlag, 1988.

[86] M. Ferris and T. Munson, "Complementarity Problems in GAMS and the PATH solver," *University of Wisconsin–Madison, Tech. Rep.,* pp. 98-12, 1998.

[87] C. Lemke and J. Howson, "Equilibrium points of bimatrix games," *SIAM Journal on Applied Mathematics,* vol. 12, pp. 413-423, 1964.

[88] F. Jourdan, P. Alart and M. Jean, "A Gauss-Seidel Like Algorithm to Solve Frictional Contact Problems," *Computer Methods in Applied Mechanics and Engineering,* vol. 155, pp. 31-47, 1998.

[89] M. Forg, F. Pfeiffer and H. Ulbrich, "Simulation of unilateral constrained systems with many bodies," *Multibody System Dynamics,* vol. 14, pp. 137-154, 2005.

[90] D. Stewart and J. Trinkle, "An Implicit Time-Stepping Scheme for Rigid Body Dynamics with Coulomb Friction," in *Proceedings of IEEE International Conference on Robotics and Automation,* San Francisco,CA, 2000.

[91] J. Lloyd, "Fast Implementation of Lemke's Algorithm for Rigid Body Contact Simulation Automation," in *IEEE International Conference on Robotics and* , Barcelona, Spain, 2005.

[92] E. Guendelman, R. Bridson and R. Fedkiw, "Nonconvex rigid bodies with stacking," *ACM Transactions on Graphics,* vol. 22, no. 3, pp. 871-878, 2003.

[93] P. Kry and D. Pai, "Interaction capture and synthesis," *ACM Transactions on Graphics,* vol. 25, no. 3, pp. 872-880, 2006.

[94] R. Cottle and G. Dantzig, "Complementary pivot theory of mathematical programming," *Linear Algebra and Its Applications,* vol. 1, no. 1968, pp. 103-125.

[95] V. Acary and F. Perignon, "An Introduction to Siconos," *INRIA, Tech Rep.,* no. 340,

2007.

[96] T. Woloszynski, P. Podsiadlo and G. Stachowiak, “Efficient Solution to the Cavitation Problem in Hydrodynamic Lubrication,” *Tribology Letters,* vol. 58, 2015.

[97] G. Dantzig and R. Cottle, “POSITIVE (SEMI-) DEFINITE MATRICES AND MATHE MATICAL PROGRAMMING,” *J. Abadie (ed.), Nonlinear programming ,* pp. 55-73, 1963.

[98] T. De Luca, F. Facchinei and C. Kanzow, “A semismoothequation approach to the solution of nonlinear complementarity problems,” *Math Program,* vol. 75, pp. 407-439, 1996.

[99] C. Kelley, Solving Nonlinear Equations with Newton's Method, Philadelphia: SIAM, 2003.

[100] L. Marmorini, A. Baldini, E. Bertocchi, M. Giacopini, R. Rosi and A. Strozzi, “On the Loosening Mechanism of a Bush Press-Fitted in the Small End of a Connecting Rod,” *Proceedings of the Institution of Mechanical Engineers Part D: Journal of Automobile Engineering,* vol. 226, no. 3, pp. 312-324, 2012.

[101] T. Suhara, S. Ato, M. Takiguchi and S. Furuhama, “Friction and Lubrication Characteristics of Piston Pin Boss Bearings of an Automotive Engine,” in *SAE Technical Paper 970840*, 1997.

[102] M. Takiguchi, K. Nagasawa and T. Suhara, “Friction and Lubrication Characteristics of Small End Connecting Rod Bearing of a Automotive Engine,” in *18th Annual Fall Technical Conference of the ASME Internal Combustion Engine Division, Part 2*, Fairborn, USA, 1996.

[103] N. Antoni, Q. Nguyen, J.-L. Ligier, P. Saffré and J. Pastor, “On the Cumulative microslip phenomenon,” *European Journal of Mechanics - A/Solids,* vol. 26, pp. 626-646, 2007.

[104] M. Aitken and H. McCallion, “Elastohydrodynamic Lubrication of Big-End Bearings Part 1: Theory,” *Proceedings of The Institution of Mechanical Engineers Part C-journal of Mechanical Engineering Science - PROC INST MECH ENG C-J MECH E,* vol. 205, pp. 99-106, 1991.

[105] B. Fantino, J. Frene and J. Du Parquet, “Elastic Connecting-Rod Bearing With Piezoviscous Lubricant: Analysis of the Steady-State Characteristics.,” *ASME. J. of Lubrication Tech,* vol. 101, no. 2, pp. 190-197, 1979.

[106] D. Wang, O. Mian, D. Merritt and G. Zhu, “Elasto-Hydrodynamic Lubrication Analysis and Wear Prediction of Connecting Rod Small-End Bush and Piston Pin Interface,” in *SAE International 2008-36-0068,* 2008.

[107] J. Ligier and P. Ragot, “Small End Conrod Lubrication,” in *SAE Technical Paper 2006-01-1101,* 2006.

[108] M. Spuria, D. Bonneau, Y. Le Baratoux and P. Molari, “A dynamic Model for an Internal Combustion Engine Full-Fullfloating,” in *XVII Congresso dell’Associazione Italiana di Meccanica Teorica e Applicata*, Firenze, 2015.

[109] D. Bonneau and V. Optasanu, “Finite Element Mass-Conserving Cavitation Algorithm in Pure Squeeze Motion.Validation/Application to a Connecting-Rod Small End Bearing,” *Journal of Tribology,* vol. 122, no. 1, pp. 162-169, 2000.

[110] L. Bertocchi, M. Giacopini and D. Dini, “Analysis of the Lubrication Regimes at the Small End and Big End of a Connecting Rod of A High Performance Motorbike Engine,” in *Proceedings of the ASME/STLE 2012 International Joint Tribology Conference,* Denver,Colorado,USA, 2012.

[111] K. Clark, J. Antonevich, D. Kemppainen and G. Barna, “Piston Pin Dynamics and Temperature in a CI Engine.,” *SAE International Journal of Engines,* vol. 2, no. 1, pp. 91-105, 2009.

[112] J. Ligier and P. Ragot, “Piston Pin: Wear and Rotating Motion,” in *SAE Technical Paper No. 2005-01-1651,* 2005.

[113] M. Giacopini, S. Sissa, R. Rosi and S. Fantoni, “Influence of Different Temperature Distributions on the Fatigue Life of a Motorcycle Piston,” *Proceedings of the Institution of Mechanical Engineers, Part D, Journal of Automobile Engineering,* vol. 229, no. 9, pp. 1279-1288, 2015.

[114] R. Craig and M. Bampton, “Coupling of Substructures for Dynamic Analyses,” *AIAA Journal, American Institute of Aeronautics and Astronautics,* vol. 6, no. 7, pp. 1313-1319, 1968.

[115] K. Olsson, “Cavitation in Dynamically Loaded Bearings,” in *Transactions of Chalmers University of Technology*, Goteborg,Sweden, 1965.

[116] Ricardo Software, *PISDYN - RINGPAK User Manual,* Van Buren Township, MI 48111, U.S.A., 2017.

[117] C. Arcoumanis, P. Ostovar e R. Mortier, «Mixed Lubrication Modelling of Newtonian and Shear Thinning Liquids in a Piston-Ring Configuration,» *SAE Technical Paper 972924,* 1997.

[118] E. Tomanik, H. Chacon e G. Teixeira, «A simple numerical procedure to calculate the input data of Greenwood-Williamson model of asperity contact for actual engineering surfaces,» *Tribology and Interface Engineering Series,* vol. 41, pp. 205-215, 2003.

[119] AVL List GmbH, *Advanced Simulation Technologies -Software Documentation,* 2018.

[120] H. Allmaier, C. Priestner, H. Priebsch, C. Forstner e F. Novotny-Farkas, «redicting friction reliably and accurately in journal bearings—A systematic validation of simulation results with experimental measurements,» *Tribology International - TRIBOL INT,* vol. 44, pp. 1151-1160, 01 09 2011.

[121] D. E. Sander, H. Allmaier, H. Priebsch, M. Witt e A. Skiadas, «Simulation of journal bearing friction in severe mixed lubrication – Validation and effect of surface smoothing due to running-in,» *Tribology International,* vol. 96, 01 12 2015.

[122] A. Ferretti, M. Giacopini, L. N. Mastrandrea e D. Dini, «Investigation of the Influence of Different Asperity Contact Models on the Elastohydrodynamic Analysis of a Conrod Small-End/Piston Pin Coupling,» *SAE Int. J. Engines,* vol. 11, n. 6, pp. 919-934, 2018.